

Higgs Boson Properties and Search for Additional Resonances

by

Can You

A dissertation submitted to The Johns Hopkins University in conformity with the
requirements for the degree of Doctor of Philosophy.

Baltimore, Maryland

July, 2017

CERN-THESIS-2017-128
05/06/2017



© Can You 2017

All rights reserved

Abstract

The Higgs boson was predicted by the Standard Model of particle physics and jointly discovered by the CMS and ATLAS experiments at LHC, in 2012. Following its discovery, the property measurements of the Higgs boson and the search for additional resonances become important research goals. The Standard Model is not the complete theory and leaves many questions unanswered, therefore it is important to search for any evidence of new physics beyond the SM. This thesis will briefly introduce the theoretical motivation for the Higgs boson, the production and decay mechanisms of the Higgs boson, and the methods used for analysis of the Higgs boson properties. The spin-1 and spin-2 Higgs hypotheses are tested in $H \rightarrow ZZ \rightarrow 4\ell$ channel, using the data recorded by CMS in Run1 of LHC. The exotic spin models were excluded and the Higgs boson is shown to agree with the Standard Model prediction of spin-0. The search for high-mass Higgs-like resonance is performed in $H \rightarrow ZZ \rightarrow 4\ell$ and $H \rightarrow ZZ \rightarrow 2\ell 2q$ channels, using data recorded by CMS in Run2 of LHC. No excess at high mass region is observed for spin-0 or spin-2 models, and the limits are set on production cross section of new potential resonances.

Primary Reader: Andrei Gritsan

Secondary Reader: Barry Blumenfeld

Acknowledgments

I would like to thank my advisor, Andrei Gritsan, who has encouraged me to be more confident and pointed out many aspects that I could work on and improve. It is your patient and careful guidance and constant pursue of excellence that lead me to become a better researcher, and gave me more courage in facing challenges. I also wish to thank Meng Xiao, who kindly gave me guidance and encouragements on research, inspired me with her determination, and shared with me many of her brilliant ideas. I would like to thank Andrew, Ian and Chris, who have helped me to start my first research projects, patiently explained to me the basics, and helped me to become a independent researcher. I would like to thank Xiaozhou, Jonathan, Ulascan, Heshy and Carol. It is very fortunate to collaborate with great researchers like you. I learned a lot from each of you. I would like to thank Wenzer and Robert, your motivation and passion for research made it a very enjoyable experience to work with you. I also wish to thank many people outside JHU, in the HZZ group and alignment group, and many researchers and friends I met at CERN.

I would like to thank my undergraduate advisors Hoi Fung Chau, Jason Pun

and John Leung, for guiding me through my years at the University of Hong Kong, teaching me to deal with various problems in my study and student life, and helping me to find my interest in particle physics. I must also thank my high school physics teachers Yunhui Li and Liang Zhang, who cultivated in me the passion for math and science, and taught me to tackle problems outside the textbooks.

I cannot thank my family enough for supporting me to pursue this PhD. I want to thank my parents, who always encouraged me to seek challenges, and always believed in me when I face difficulties. I wish to thank my husband and colleague, Lei Feng, for his love and support in the past eleven years.

For all the friends I met in these years, thank you. You made my PhD life a warm and delightful memory.

Contents

Abstract	ii
Acknowledgments	iv
List of Tables	xiii
List of Figures	xiv
1 Introduction	1
1.1 The Elementary Particles	1
1.2 The SM Higgs Boson	4
1.3 Beyond the SM	5
1.4 Summary	7
2 Higgs Boson Phenomenology at the LHC	8
2.1 Higgs Boson Production	9
2.2 Higgs Boson Decay	11

2.3	Kinematics for Properties Measurement	12
2.3.1	spin-0 interactions	12
2.3.2	spin-1 interactions	13
2.3.3	spin-2 interactions	14
2.3.4	Kinematic discriminants based on Matrix Element Method . .	14
3	Experimental Setup	18
3.1	The Large Hadron Collider	18
3.2	The Compact Muon Solenoid	21
3.2.1	Coordinate Conventions	22
3.2.2	The Magnet	23
3.2.3	Inner Tracker	23
3.2.3.1	Pixel Detector	24
3.2.3.2	Strip Detector	25
3.2.4	Electromagnetic Calorimeter	26
3.2.5	Hadronic Calorimeter	27
3.2.6	Muon System	30
3.2.6.1	Muon Drift Tubes	32
3.2.6.2	Cathode Strip Chambers	33
3.2.6.3	Resistive Plate Chambers	33
3.3	Alignment of CMS tracker	34
3.3.1	The Problem	35

3.3.2	Parameterization	36
3.3.3	Linear Least Squares Model	36
3.3.4	Matrix Partitioning	37
3.3.5	Single Track Fit	40
3.3.6	Build the Matrices	41
3.3.7	The Approximate Solutions - Tracker Alignment Algorithms .	42
3.3.7.1	Local Approach	42
3.3.7.2	Global Approach	48
3.3.8	Alignment Strategies	49
3.3.8.1	Hierarchical Alignment	49
3.3.8.2	Differential Alignment	50
3.3.9	Weak Modes	51
3.3.9.1	Z-Expansion	52
3.3.9.2	charge-symmetric deformations	54
3.3.9.3	charge-asymmetric deformations	55
3.3.9.4	$Z\mu\mu$ validation and constraint	55
3.3.10	Validation Methods	57
3.3.10.1	Track Splitting	57
3.3.10.2	Distribution of the Median of Residuals	59
3.3.10.3	Primary Vertex	59
3.3.11	Conclusion	61

4	Data Analysis Methods	64
4.1	Trigger and Data Acquisition	64
4.1.1	Level-1 Triggers	65
4.1.2	High Level Triggers (HLT)	65
4.2	Software and Computing	65
4.3	Reconstruction of Physical Objects	66
4.3.1	Leptons	67
4.3.1.1	Electrons	67
4.3.1.2	Muons	68
4.3.1.3	Lepton isolation and SIP	70
4.3.1.4	FSR Photons	71
4.3.2	Jets	72
4.4	Event Selection	72
4.4.1	$H \rightarrow ZZ \rightarrow 4\ell$	72
4.4.2	$H \rightarrow ZZ \rightarrow 2\ell 2q$	74
4.5	Monte Carlo Simulation	77
4.6	Statistical Analysis	79
4.6.1	Test of Hypotheses	79
4.6.2	Profile Likelihood Ratio	80
4.6.3	Exclusion Limits and Significance of Excess	81
4.6.4	Test for Alternative Signals	83

5	Exclusion of the Higgs Boson Exotic Spin	85
5.1	Experimental data and Simulated Samples	86
5.2	Event selection and backgrounds	87
5.3	Yields	89
5.4	Kinematic Distributions	91
5.5	Hypothesis Testing	93
5.5.1	Spin-1	93
5.5.2	Spin-2	95
5.6	Systematic Uncertainties	99
5.6.1	Theoretical uncertainties	99
5.6.2	Experimental uncertainties	99
5.7	Results	101
5.7.1	Testing of mixed spin-1 hypotheses	101
5.7.2	Testing of spin-2 hypotheses	106
5.7.3	Constrains on mixed non-interfering states	112
5.8	Summary of the exotic spin studies	121
6	Search for High Mass $X \rightarrow VV$ Resonances	122
6.1	Experimental data and Simulated Samples	123
6.2	Event Selection and Categorization	124
6.2.1	$X \rightarrow ZZ \rightarrow 4\ell$	124
6.2.2	$X \rightarrow ZZ \rightarrow 2\ell 2q$	125

6.3	Kinematic discriminants	129
6.3.1	$X \rightarrow ZZ \rightarrow 4\ell$	129
6.3.2	$X \rightarrow ZZ \rightarrow 2\ell 2q$	129
6.4	Signal and background parameterization	135
6.5	Signal Model	136
6.5.1	Lineshape prior to detector effects	137
6.5.2	Efficiency	137
6.5.3	Resolution	139
6.5.3.1	Final parameterization	140
6.6	Background Estimation	144
6.6.1	$X \rightarrow ZZ \rightarrow 4\ell$	144
6.6.2	$X \rightarrow ZZ \rightarrow 2\ell 2q$	144
6.6.2.1	Estimation of Z+jets background	144
6.6.2.2	Estimation of $t\bar{t}$ background	146
6.7	Systematic Uncertainties	147
6.7.1	$X \rightarrow ZZ \rightarrow 4\ell$	148
6.7.2	$X \rightarrow ZZ \rightarrow 2\ell 2q$	149
6.8	Results	150
7	Conclusion	154
	Bibliography	156

List of Tables

3.1	LHC performance-related operational parameter and their nominal values.	20
3.2	Parameters of the CMS superconducting solenoid.	23
5.1	Spin 0 samples at 8 TeV and 7 TeV.	86
5.2	Spin 1 samples at 8 TeV and 7 TeV.	86
5.3	Spin 2 samples at 8 TeV and 7 TeV.	87
5.4	The number of estimated background and signal events, and number of observed candidates, after final inclusive selection.	90
5.5	List of kinematic discriminants used in this analyses.	91
5.6	Summary of the uncertainties.	100
5.7	A summary of models used in the analysis of spin-one hypotheses. Events are generated with SM expectation for the signal cross section ($\mu=1$).	103
5.8	List of models used in the analysis of the spin-two hypotheses corresponding to the pure states of the type noted.	107

List of Figures

1.1	The Standard Model of particle physics.	3
2.1	Feynman diagrams for common Higgs production mechanisms (a)gluon fusion, (b)vector boson fusion, (c)associated production with a gauge boson, (d)associated production with top quarks.	10
2.2	Illustration of an X (Higgs or Higgs-like) boson production and decay $gg \rightarrow X \rightarrow ZZ \rightarrow (\ell^+\ell^-)(f\bar{f})$ (left) and VBF $qq' \rightarrow qq'X$ (right). Angles and invariant masses fully characterize the orientation of the production and decay chain.	15
3.1	CMS detector	22
3.2	A quarter of the CMS inner tracker, in r-z view. The single-sided strip modules are in solid magenta lines, and the double-sided strip modules are in open blue lines. Pixel modules are in solid blue lines.	24
3.3	ECAL supermodule energy resolution. The upper series of points correspond to events taken with a 20×20 mm ² trigger, while the lower series of points correspond to events taken with a 4×4 mm ² trigger.	28
3.4	The muon momentum resolution versus the momentum, in the barrel region (left) and in endcaps (right).	31
3.5	Layout of one quarter of the muon system.	32
3.6	The convergence plot for 2016 CRUZET alignment, using HipPy package.	46
3.7	The convergence plot for module level alignment, using HipPy package.	47
3.8	The shift plot for 2016 CRUZET alignment, using HipPy package.	47
3.9	The fitted parameters with error in 2016 CRUZET alignment, using HipPy package.	48
3.10	Possible weak modes in CMS tracker alignment.	53
3.11	The impact of weak modes on track reconstruction. The dashed lines are the true track trajectories, and the solid lines are the reconstructed tracks.	55

3.12	Possible weak modes in CMS tracker alignment.	56
3.13	The track splitting validation in impact parameters d_{xy} and d_z for 2016 CRUZET alignment. The observed precision using the aligned geometry (green circles), produced with the Millepede-II and HipPy algorithms using cosmic ray data at 0T, is a major improvement over the 2015 EOY (End-of-Year) geometry (blue empty squares). The precision comes close to that of the ideal Monte Carlo (red).	58
3.14	The DMR validations for the local x- and y-directions in the barrel pixel detector. The alignment shown in magenta was produced with the Millepede-II and HipPy algorithms using 3.8 T cosmic ray and collision data collected in 2016. The blue line shows the starting geometry obtained at the end of 2015.	60
3.15	The primary vertex validation, with d_{xy} and d_z plotted in bins of track azimuth ϕ . The performance of a dedicated alignment (magenta) achieved with the Millepede-II and HipPy algorithms using cosmic ray and collision data at 3.8T is compared to the one of the alignments used to reprocess the collision data collected by CMS during 2015 (blue).	62
5.1	Observed distributions of the discriminants in data and MC expectations for the background and for a signal resonance at $m_H = 125.6$ GeV, either the SM Higgs boson or an alternative spin-1 hypothesis indicated. Top row from left to right: $\mathcal{D}_{\text{bkg}}(J^P = 1^-)$, $\mathcal{D}_{\text{bkg}}(J^P = 1^+)$, \mathcal{D}_{1^-} , \mathcal{D}_{1^+} ; bottom row from left to right: $\mathcal{D}_{\text{bkg}}^{\text{dec}}(J^P = 1^-)$, $\mathcal{D}_{\text{bkg}}^{\text{dec}}(J^P = 1^+)$, $\mathcal{D}_{1^-}^{\text{dec}}$, $\mathcal{D}_{1^+}^{\text{dec}}$. All distributions, except \mathcal{D}_{bkg} and $\mathcal{D}_{\text{bkg}}^{\text{dec}}$, are shown with the requirement $\mathcal{D}_{\text{bkg}} > 0.5$ ($\mathcal{D}_{\text{bkg}}^{\text{dec}} > 0.5$) to enhance signal purity.	92
5.2	Distribution of $\mathcal{D}_{\text{bkg}}^{\text{dec}}$ vs. $\mathcal{D}_{1^-}^{\text{dec}}$ for the qqZZ background (a) and for a signal resonance consistent with the SM Higgs boson with $m_{0^+} = 125.6$ GeV. (b)	94
5.3	Distribution of D_{bkg}^{dec} vs. D_{JP}^{dec} for the $gg \rightarrow ZZ$ background (left) and for the signal resonance consistent with the SM Higgs boson $m_H = 125.6$ GeV model.	96
5.4	Distribution of D_{bkg} in data and MC expectations for the background and for a signal resonance consistent with SM Higgs boson at $m_H = 125.6$ GeV (left). The D_{bkg}^{dec} distribution for the production independent scenario (right).	97
5.5	Distributions of D_{JP} with a requirement $D_{bkg} > 0.5$. Distributions for background and signal are shown.	98

5.6	Distribution of the test-statistic $q = -2\ln(\mathcal{L}_{JP}/\mathcal{L}_{0+})$ of the spin-1 hypothesis tested against the SM Higgs boson hypothesis, for the production independent scenario. J^P = pure 1^- (top left), mixture with $f_{b2}=0.2$ (top middle), $f_{b2}=0.4$ (top right), $f_{b2}=0.6$ (bottom left), $f_{b2}=0.8$ (bottom middle), and pure 1^+ (bottom right). Distributions for the SM Higgs boson are represented by the yellow histogram and for the alternative J^P hypotheses by the blue histogram.	102
5.7	Distribution of the test-statistic $q = -2\ln(\mathcal{L}_{JP}/\mathcal{L}_{0+})$ of the spin-1 hypothesis tested against the SM Higgs boson hypothesis, for the $q\bar{q}$ production scenario. J^P = pure 1^- (top left), mixture with $f_{b2}=0.2$ (top middle), $f_{b2}=0.4$ (top right), $f_{b2}=0.6$ (bottom left), $f_{b2}=0.8$ (bottom middle), and pure 1^+ (bottom right). Distributions for the SM Higgs boson are represented by the yellow histogram and for the alternative J^P hypotheses by the blue histogram.	104
5.8	Distribution of median test statistic q , as a function of f_{b2} . The green (red) and blue (black) bands represent the 1σ and 2σ around the median expected value for the SM (spin-1) Higgs boson hypothesis. . .	105
5.9	Distribution of test-statistics $q = -2\ln(\mathcal{L}_{JP}/\mathcal{L}_{0+})$ for two signal types (0^+ represented by the yellow histogram and alternative hypothesis by the blue histogram) for $m_H = 125.6$ GeV shown with a large number of generated experiments. Red arrow represents the observed value of the test-statistics.	108
5.10	Distribution of $q = -2\ln(\mathcal{L}_{JP}/\mathcal{L}_{0+})$ for two signal types (0^+ represented by the yellow histogram and alternative hypothesis by the blue histogram) for $m_H = 125.6$ GeV shown with a large number of generated experiments. Ten alternative hypotheses are tested in gg , $q\bar{q}$ and production model independent way.	109
5.11	Distribution of $q = -2\ln(\mathcal{L}_{JP}/\mathcal{L}_{0+})$ for two signal types (0^+ represented by the yellow histogram and alternative hypothesis by the blue histogram) for $m_H = 125.6$ GeV shown with a large number of generated experiments. Ten alternative hypotheses are tested in gg , $q\bar{q}$ and production model independent way.	110
5.12	Summary of the expected and observed values for the test-statistic q distributions for the twelve alternative hypotheses tested with respect to the SM Higgs boson. The orange (blue) bands represent the 1σ , 2σ , and 3σ around the median expected value for the SM Higgs boson hypothesis (alternative hypothesis). The black point represents the observed value.	111

5.13	Expected and observed distributions of $-2\Delta \ln \mathcal{L}$ as a function of $f(J^P)$, in the production independent (any $\rightarrow J^P$) case. $J^P =$ pure 1^- (top left), mixture with $f_{b2}=0.2$ (top middle), $f_{b2}=0.4$ (top right), $f_{b2}=0.6$ (bottom left), $f_{b2}=0.8$ (bottom middle), and pure 1^+ (bottom right). The horizontal lines at $-2\Delta \ln \mathcal{L} = 1$ and 3.84 represent the 68% and 95% C.L., respectively.	114
5.14	Expected and observed distributions of $-2\Delta \ln \mathcal{L}$ as a function of $f(J^P)$, in the $q\bar{q}$ production case. $J^P =$ pure 1^- (top left), mixture with $f_{b2}=0.2$ (top middle), $f_{b2}=0.4$ (top right), $f_{b2}=0.6$ (bottom left), $f_{b2}=0.8$ (bottom middle), and pure 1^+ (bottom right). The horizontal lines at $-2\Delta \ln \mathcal{L} = 1$ and 3.84 represent the 68% and 95% C.L., respectively.	115
5.15	Summary of expected and observed constraints on the non-interfering fraction measurements for spin-1.	116
5.16	Non-interfering fraction expectations for various spin-2 models. The above results are production-independent.	117
5.17	Non-interfering fraction expectations for various spin-2 models ($gg \rightarrow J^P$).	118
5.18	Non-interfering fraction expectations for various spin-2 models ($q\bar{q} \rightarrow J^P$).	119
5.19	Summary of expected and observed constraints on the non-interfering fraction measurements for spin-2.	120
6.1	Distribution of the invariant mass of the four-leptons in un-tagged (upper left), VBF-tagged (upper right) and RSE (bottom left) category and $\mathcal{D}_{\text{bkg}}^{\text{kin}}$ (bottom right) of all the selected events. Signal expectation including the interference effect for several mass and width hypotheses are shown in the plot. The cross-section of the signal correspondes to the expected exclusion value (times a scaling to make them more visible) on the plots, and are normalizaed to a total of 400 events on the right plot.	126
6.2	Invariant mass distribution m_{ZZ} in the signal region for the merged (left) and resolved (right) case in the different categories. The points are the observed data, the stacked histograms are the standard model simulated background, and the open histograms are simulated signal samples. The blue hatched bands refer to the sum of MC- and data-derived background estimations. Lower panels show data/estimation ratios.	128
6.3	Distribution of \mathcal{D}_{Zjj} with events with two resolved jets (top) and with a merged jet (bottom). Spin-0 on the left, spin-2 on the right.	130

6.4	Distribution of \mathcal{D}_{Zjj} vs $m_{2\ell 2q}$ with conditional normalisation for spin-0 signal (top left), DY + jets (top right), $t\bar{t}$ + WW (bottom left), ZW, ZZ diboson backgrounds (bottom right), for the merged selection. When conditionally normalised, each slice of \mathcal{D}_{Zjj} is normalised to unit area for a given value of $m_{2\ell 2q}$	131
6.5	Distribution of \mathcal{D}_{Zjj} vs $m_{2\ell 2q}$ with conditional normalisation for spin-0 signal (top left), DY + jets (top right), $t\bar{t}$ + WW (bottom left), ZW, ZZ diboson backgrounds (bottom right), for the resolved selection. When conditionally normalised, each slice of \mathcal{D}_{Zjj} is normalised to unit area for a given value of $m_{2\ell 2q}$	132
6.6	Distribution of \mathcal{D}_{Zjj} vs $m_{2\ell 2q}$ with conditional normalisation for spin-2 signal (top left), DY + jets (top right), $t\bar{t}$ + WW (bottom left), ZW, ZZ diboson backgrounds (bottom right), for the merged selection. When conditionally normalised, each slice of \mathcal{D}_{Zjj} is normalised to unit area for a given value of $m_{2\ell 2q}$	133
6.7	Distribution of \mathcal{D}_{Zjj} vs $m_{2\ell 2q}$ with conditional normalisation for spin-2 signal (top left), DY + jets (top right), $t\bar{t}$ + WW (bottom left), ZW, ZZ diboson backgrounds (bottom right), for the resolved selection. When conditionally normalised, each slice of \mathcal{D}_{Zjj} is normalised to unit area for a given value of $m_{2\ell 2q}$	134
6.8	The efficiency of the signal events to pass the $X \rightarrow ZZ \rightarrow 4\ell$ (top) and $X \rightarrow ZZ \rightarrow \mu\mu qq$ (bottom) selection as a function of the generated ZZ invariant mass, from ggH (left) and VBF (right) production modes.	138
6.9	Representative $m_{4\ell}$ distributions of a resolution function $\mathcal{R}(m_{4\ell} m_{4\ell}^{\text{ideal}})$ in $2e2\mu$ (left), $4e$ (middle), and 4μ (right) channels. Several examples are shown from top to bottom: $m_{4\ell} = 200, 740, 1000$ GeV.	141
6.10	Representative $m_{2\ell 2q}$ distributions of a resolution function $\mathcal{R}(m_{2\ell 2q} m_{2\ell 2q}^{\text{ideal}})$ two-jet (left) and merged-jet (right) categories. Several examples are shown from top to bottom: $m_{2\ell 2q} = 750, 1000, 2000$ GeV.	142
6.11	Dependence of six parameters of the resolution function in the $2e2\mu$ (left), $4e$ (middle), and 4μ (right) channels. Point show results of individual fits, smooth curves show parameterization from a simultaneous fit of all distributions.	143
6.12	Dependence of six parameters of the resolution function in the two-jet (left) and merged-jet (right) categories. Point show results of individual fits, smooth curves show parameterization from a simultaneous fit of all distributions.	143
6.13	Expected and observed upper limits on the $pp \rightarrow X \rightarrow ZZ$ cross section as a function of m_X at $\Gamma_X = 0, 10, \text{ and } 100$ GeV, for 4ℓ final state, using 35.9 fb^{-1} of CMS data at 13 TeV. Left: f_{VBF} profiled. Right: $f_{\text{VBF}} = 1$, pure VBF model.	151

6.14	Expected and observed upper limits on the $pp \rightarrow X \rightarrow ZZ$ cross section as a function of m_X at $\Gamma_X = 0, 10$, and 100 GeV, for $2\ell 2q$ final state, using 35.9 fb^{-1} of CMS data at 13 TeV . Left: f_{VBF} profiled. Right: $f_{\text{VBF}} = 1$, pure VBF model.	152
6.15	Expected and observed upper limits on the $pp \rightarrow X \rightarrow ZZ$ cross section as a function of m_X at $\Gamma_X = 0, 10$, and 100 GeV, with 4ℓ and $2\ell 2q$ channels combined, using 35.9 fb^{-1} of CMS data at 13 TeV . Left: f_{VBF} profiled. Right: $f_{\text{VBF}} = 1$, pure VBF model.	152
6.16	Expected and observed upper limits on the $pp \rightarrow X \rightarrow ZZ$ cross section under narrow width resonance assumption for 12.9 fb^{-1} of CMS data at 13 TeV with a spin-2 graviton assumption.	153

Chapter 1

Introduction

1.1 The Elementary Particles

The elementary particles are categorized into fermions (with half-integer spin) and bosons (with integer spin). Fermions are the (anti-)matter particles, while vector (spin-1) bosons are the force carriers (mediators). The only known scalar boson, Higgs boson, is the quantum excitation of the Higgs field, a field responsible for the mass of particles. Fermions and bosons obey different statistics, i.e. the Fermi-Dirac statistics and the Bose-Einstein statistics. For example, electrons are fermions which obey electrodynamics, and the electromagnetic force is mediated by the exchange of photons.

There are four known fundamental forces in nature: the strong force, the electromagnetic force, the weak force, and the gravitational force. Gravity is much weaker

than the other forces at subatomic level, and is not included in the Standard Model of particle physics.

In the standard model, the elementary fermions are grouped into leptons, quarks and their antiparticles.

Setting the unit charge to be the magnitude of electron charge ($e=1$), there are three leptons with electromagnetic charge of -1 : the electron, the muon and the tau. There are also three uncharged leptons, called neutrinos: electron neutrino, muon neutrino and tau neutrino. These form three generations each with two particles. There are also 6 leptonic antiparticles, which correspond to the 6 leptons stated above. The particles and their corresponding antiparticles have the same mass but opposite quantum properties.

There are 6 quarks divided into 3 generations, and 6 corresponding antiquarks. Quarks have fractional electric charge of either $2/3$ or $-1/3$, as shown in figure 1.1. They also carry colors, which are the “charges” for strong interaction. There are three types of colors: red, green and blue. The gluons only couple to color-charged particles, in the same way that photons only couple to charged particles. Gluons themselves also carry color. The antiquarks carry fractional charge of $-2/3$ or $1/3$, and anticolors. Hardrons are composite particles formed by quarks. They are called mesons if they are made of one quark and one antiquark, and baryons if they are made of three quarks/antiquarks. The complete family of elementary particles described by standard model is summarized in figure 1.1

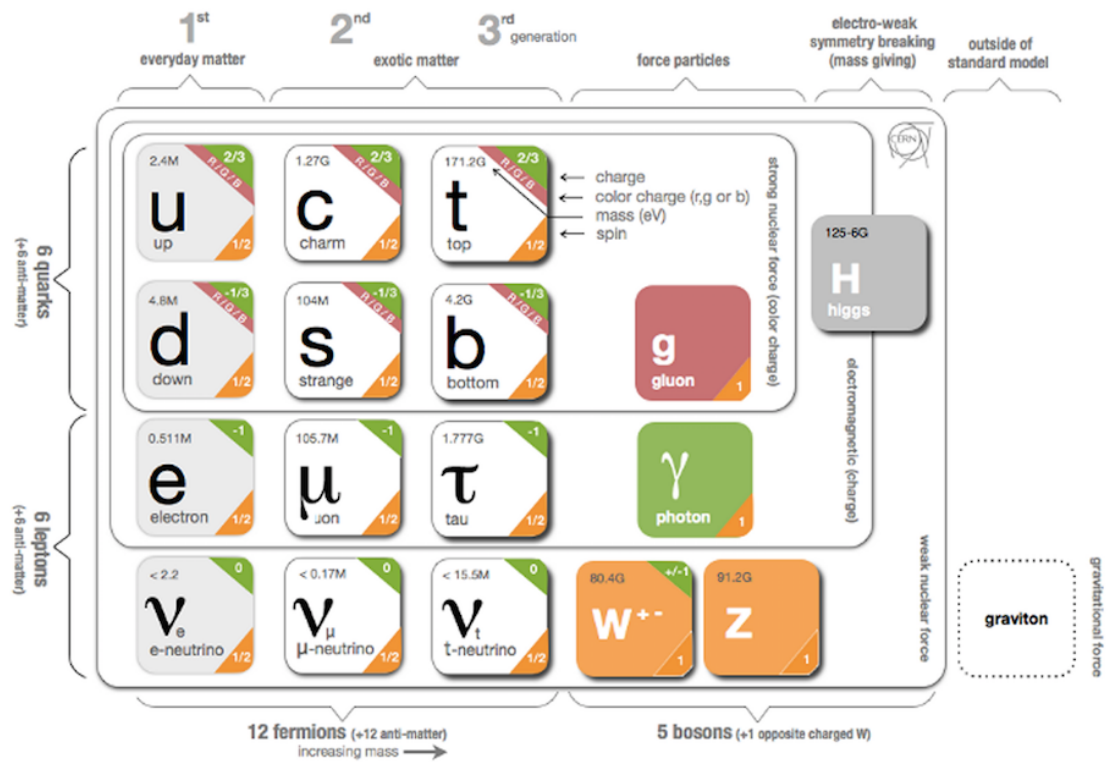


Figure 1.1: The Standard Model of particle physics.

1.2 The SM Higgs Boson

In relativistic quantum field theory, particles are not localized entity but quantized excitation of fields. The particles and their interactions are described by Lagrangians. A scalar field (spin-0 particle) is described by the Klein-Gordon Lagrangian. A spinor field (spin-1/2 particle) is described by the Dirac Lagrangian, and a vector field (spin-1 particle) is described by the Proca Lagrangian.

Local gauge invariance means that the Lagrangian is invariant under 'local' phase transformation, or adding a space-dependent phase factor. Local gauge invariance requires the gauge bosons to be massless. While the photons and gluons, mediators for eletromagnetic and strong interactions, are massless, the W and Z gauge bosons for weak interaction are massive.

In Standard Model, spontaneous symmetry breaking and the Higgs Mechanism are responsible for the mass of weak gauge bosons (W and Z). In the early universe, the Higgs potential is symmetrically centered around the stable lowest energy state, but as the universe cooled down, the symmetry was broken and Higgs potential changed to a "Mexican-hat" shape. The SU(2) symmetry of weak interaction can be spontaneously broken, by choosing a non-zero ground state in two-component scalar field, and thus introduce a mass term for the weak gauge bosons. In this mechanism, the massive gauge field is introduced as well as a massive scalar particle - the Higgs Boson, the excitation of the Higgs field. The Higgs field also accounts for the masses of the fermions. The Higgs field permeates all the space, and the quarks and leptons gained

mass by coupling to the Higgs field in the early universe.

The introduction of Higgs boson completes the standard model, but for a long time it remained the last missing piece with no experimental evidence. Since the proposal of the Higgs Mechanism in 1960's, the search for Higgs boson has been the main goal for many major high energy experiments. The theory leaves the mass of the Higgs Boson a free parameter, thus a large mass region need to be searched. The Large Electron-Positron (LEP) collider, and the Tevatron experiments set several constraints on the Higgs mass, but no evidence of the Higgs particle was found at 95% confidence level. After about 50 years, on 4 July 2012, the CMS and ATLAS experiments at LHC jointly announced the discovery of the Higgs particle. On 8 October 2013, the Nobel prize in physics was awarded to Francois Englert and Peter Higgs for their work on explaining origin of mass by Brout-Englert-Higgs mechanism.

1.3 Beyond the SM

The observed universe is made of matter. The Big Bang should have created the matter and antimatter in equal amounts. When a particle encounters its antiparticle, they annihilate, but in the end the main leftover is matter. The matter-antimatter asymmetry remains unexplained by the standard model. In 1967, Sakharov proposed that the matter-antimatter imbalance could be caused by processes that satisfy a set of three conditions: baryon number violation, C-symmetry and CP-symmetry viola-

tion, and interactions out of thermal equilibrium. CP-violation has been observed in neutral Kaons experiments by Cronin and Fitch. However, the known CP violation in the weak interactions of quarks is not enough to account for the degree of matter-antimatter asymmetry observed. There must be some explanations beyond standard model.

The matter we know about, described in standard model, only accounts for about 5% of the total matter-energy content of the universe. The other part of universe is made of Dark Matter (about 20%) and Dark Energy (about 75%). Dark matter is indicated by its gravitational effects in astronomical measurements, and dark energy is responsible for the accelerating expansion of universe. However, we have no idea what they are made of.

There's also a so called hierarchy problem. Why is Higgs boson mass much smaller than the Plank scale (10^{19} GeV)? Quantum corrections to Higgs boson mass is much larger than the physical Higgs mass. This requires the fine-tuning cancellation between the correction and the bare Higgs mass.

Gravity is not included in standard model. In order to include gravity, a quantum version of general relativity needs to be formulated. This has not yet been successfully solved. Practically it doesn't affect the models of particle physics since it's much weaker than other three forces.

These unsolved questions indicates that there must be physics beyond the standard model. Supersymmetry (SUSY) is one of the interesting models. SUSY proposed a

new symmetry between bosons and fermions. In SUSY, each fermion has a bosonic partner and each boson has a fermionic partner. The Planck-scale quantum corrections cancel between the partners leads to a solution of the hierarchy problem. SUSY provides possible dark matter candidates. SUSY provides models with extended Higgs sector, such as two-Higgs-doublet models (2HDM), and allows for additional CP violation in extended Higgs sector. The other models include extra dimensional models and string theories.

1.4 Summary

The Higgs boson was predicted in standard model and discovered by CMS and ATLAS in 2012. There are strong motivations for models beyond the standard model. Therefore, precise measurement of the Higgs boson's quantum numbers and search for multiple Higgs bosons could give us hints of new physics.

Chapter 2 will discuss the phenomenology of Higgs boson at LHC. Chapter 3 will introduce the LHC and the CMS detector. Chapter 4 will discuss the computing framework and statistical data analysis methods used in CMS analyses. Chapter 5 will present the measurement of the exotic spin of the Higgs boson and chapter 6 will present the search for a new high mass Higgs-like resonance. Chapter 7 will summarize the thesis and discuss the future outlooks.

Chapter 2

Higgs Boson Phenomenology at the LHC

The Standard Model Higgs boson is a CP-even particle of spin 0. Its mass is a free parameter in SM. The interaction of Higgs boson with other fundamental particles depends on their masses. The couplings to fermions are linearly proportional to the fermion mass, while the coupling to bosons are proportional to the square of the boson masses. Therefore, the dominant Higgs production and decay involves coupling to heavy particles such as W, Z and third generation quarks and leptons.

2.1 Higgs Boson Production

The main Higgs production mechanisms at the LHC are gluon fusion, vector boson fusion, associated production with a weak gauge boson, and associated production with a pair of top/anti-top quarks.

The gluon fusion production mechanism, shown in figure 2.1(a), is the dominant production mechanism at the LHC. Gluon-gluon has the highest probability for producing a resonance. However, gluons cannot couple to the Higgs boson directly because they are massless. The gluon fusion process is mediated by an exchange of virtual top quark. The coupling to lighter quarks is suppressed by a factor of m_q .

The vector boson fusion production mechanism, shown in figure 2.1(b), has the second-largest cross section at the LHC. The VBF process is a scattering of a pair of (anti-)quarks mediated by exchange a W or Z boson, which radiates a Higgs boson. The scattered (anti-)quarks give rise to two energetic jets at high pseudorapidity, in the forward and backward regions of the detector, which is the signature of VBF process. Gluon fusion can also produce 2 jets due to NLO and NNLO effects, but the kinematics of the jets are different from those in VBF, which is used for their discrimination.

The associated production with W/Z bosons, or top quarks, as shown in figure 2.1(c)(d), accounts for about 5% of the total Higgs production cross section.³⁰

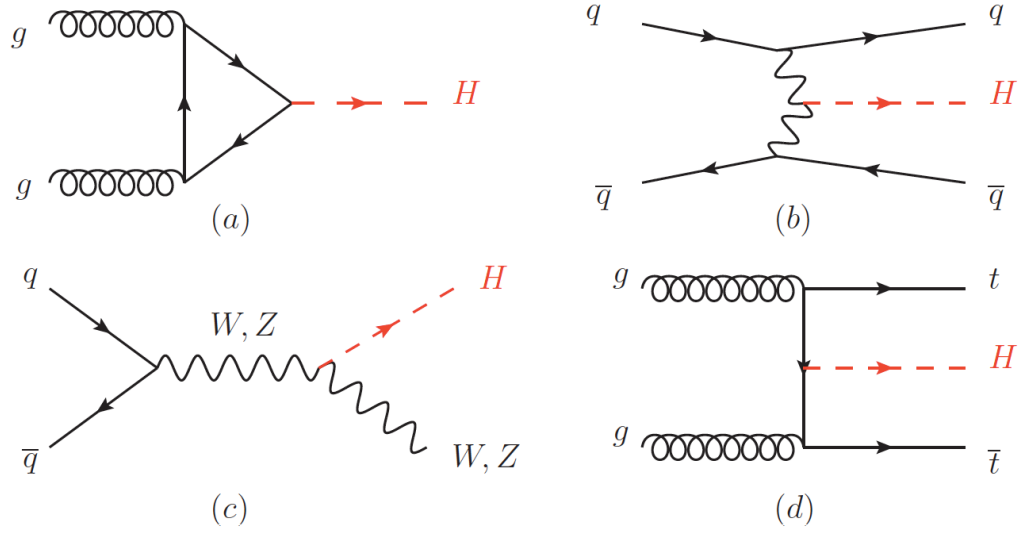


Figure 2.1: Feynman diagrams for common Higgs production mechanisms (a)gluon fusion, (b)vector boson fusion, (c)associated production with a gauge boson, (d)associated production with top quarks.

2.2 Higgs Boson Decay

The Higgs boson couples to its decay products according to their masses. At the Higgs mass of 125 GeV or lower, $H \rightarrow b\bar{b}$ is the dominant decay mode, because b-quarks are the heaviest on-shell decay particles. At high mass, $H \rightarrow WW$ and $H \rightarrow ZZ$ dominates. $H \rightarrow \gamma\gamma$ and $H \rightarrow Z\gamma$ have much smaller branching ratios, since massless photon cannot couple to Higgs directly, the process requires a loop with massive particles.

The sensitivity of a channel depends on the decay branching ratio, reconstructed mass resolution and level of background. $H \rightarrow b\bar{b}$ has large QCD backgrounds and poor mass resolution. $H \rightarrow WW$ has missing energy due to neutrinos in final decay products. The expected cross section of $H \rightarrow ZZ$ is relatively small compared with $H \rightarrow b\bar{b}$ or $H \rightarrow WW$, but $H \rightarrow ZZ \rightarrow 4l$ process has small background and fully decay kinematics with high resolution. Therefore, it's an ideal channel for discovery and property measurement of the Higgs boson. This thesis will focus on the $H \rightarrow ZZ$ channels.

2.3 Kinematics for Properties Measurement

The standard model Higgs boson is a CP-even, spin-0 particle. However, at the time of discovery, we need to measure if the new particle is indeed spin-0, or it is spin-1 or spin-2, which would indicate physics beyond standard model.

The interaction of the resonance X and a pair of spin-1 bosons V_1 and V_2 can be described by scattering amplitudes.

2.3.1 spin-0 interactions

For a spin-0 particle X, the XVV interaction can be parameterized as:

$$\begin{aligned}
 A(X_{J=0} \rightarrow V_1 V_2) = & v^{-1} \left(\left[a_1 - e^{i\phi_{\Lambda_1}} \frac{q_{Z_1}^2 + q_{Z_2}^2}{(\Lambda_1)^2} \right] m_Z^2 \epsilon_{Z_1}^* \epsilon_{Z_2}^* \right. \\
 & + a_2 f_{\mu\nu}^{*(Z)} f^{*(Z),\mu\nu} + a_3 f_{\mu\nu}^{*(Z)} \tilde{f}^{*(Z),\mu\nu} \\
 & \left. \right)
 \end{aligned}
 \tag{2.1}$$

V_1 and V_2 stand for two electroweak bosons (Z bosons in this thesis). v stands for the vacuum expectation value of the X field. $f^{(i)\mu\nu} = \epsilon_i^\mu q_i^\nu - \epsilon_i^\nu q_i^\mu$ is the field strength tensor of a gauge boson V_i with momentum q_i and polarization vector ϵ_i . $\tilde{f}_{\mu\nu}^{(i)}$ is the dual field strength tensor. The superscript * designates the complex conjugate.

The SM HZZ couplings at tree level corresponds to the a_1 term, with $a_1 =$

2. Parity-conserving interaction of a pseudo-scalar (CP-odd) corresponds to the a_3 terms. The a_3 (CP-odd) term appears in the SM only at a three-loop level and is extremely small. The a_1 and a_2 terms describe the parity-conserving interaction of a scalar (CP-even). Λ_1 stand for the scale of new physics.

2.3.2 spin-1 interactions

For a spin-1 particle X , the XVV interaction can be parameterized as:

$$A(X_{J=1} \rightarrow VV) = b_1 [(\epsilon_1^* q) (\epsilon_2^* \epsilon_X) + (\epsilon_2^* q) (\epsilon_1^* \epsilon_X)] + b_2 \epsilon_{\alpha\mu\nu\beta} \epsilon_X^\alpha \epsilon_1^{*\mu} \epsilon_2^{*\nu} \tilde{q}^\beta \quad (2.2)$$

ϵ_X is the polarization vector of the particle X . $b_1 \neq 0$ coupling corresponds to a vector particle, while $b_2 \neq 0$ coupling corresponds to a pseudovector particle.

In order to test the SM Higgs against some mixed states of spin-one, we can define the effective fraction of pseudovector as:

$$f_{b_2} = \frac{|b_2|^2 \sigma_2}{|b_1|^2 \sigma_1 + |b_2|^2 \sigma_2} \quad (2.3)$$

where σ_i is the effective cross-section of the process corresponding to $b_i = 1, b_{j \neq i} = 0$ in the $H \rightarrow ZZ^{(*)} \rightarrow 2e2\mu$ final state.

2.3.3 spin-2 interactions

For a spin-2 particle X, the XVV interaction can be parameterized as:

$$\begin{aligned}
A(X_{J=2} \rightarrow V_1 V_2) = & \Lambda^{-1} \left[2c_1 t_{\mu\nu} f^{*1,\mu\alpha} f^{*2,\nu\alpha} + 2c_2 t_{\mu\nu} \frac{q_\alpha q_\beta}{\Lambda^2} f^{*1,\mu\alpha} f^{*2,\nu,\beta} \right. \\
& + c_3 \frac{\tilde{q}^\beta \tilde{q}^\alpha}{\Lambda^2} t_{\beta\nu} (f^{*1,\mu\nu} f_{\mu\alpha}^{*2} + f^{*2,\mu\nu} f_{\mu\alpha}^{*1}) + c_4 \frac{\tilde{q}^\nu \tilde{q}^\mu}{\Lambda^2} t_{\mu\nu} f^{*1,\alpha\beta} f_{\alpha\beta}^{*(2)} \\
& + m_V^2 \left(2c_5 t_{\mu\nu} \epsilon_1^{*\mu} \epsilon_2^{*\nu} + 2c_6 \frac{\tilde{q}^\mu q_\alpha}{\Lambda^2} t_{\mu\nu} (\epsilon_1^{*\nu} \epsilon_2^{*\alpha} - \epsilon_1^{*\alpha} \epsilon_2^{*\nu}) + c_7 \frac{\tilde{q}^\mu \tilde{q}^\nu}{\Lambda^2} t_{\mu\nu} \epsilon_1^* \epsilon_2^* \right) \\
& + c_8 \frac{\tilde{q}^\mu \tilde{q}^\nu}{\Lambda^2} t_{\mu\nu} f^{*1,\alpha\beta} \tilde{f}_{\alpha\beta}^{*(2)} + c_9 t^{\mu\alpha} \tilde{q}_\alpha \epsilon_{\mu\nu\rho\sigma} \epsilon_1^{*\nu} \epsilon_2^{*\rho} q^\sigma \\
& \left. + \frac{c_{10} t^{\mu\alpha} \tilde{q}_\alpha}{\Lambda^2} \epsilon_{\mu\nu\rho\sigma} q^\rho \tilde{q}^\sigma (\epsilon_1^{*\nu} (q\epsilon_2^*) + \epsilon_2^{*\nu} (q\epsilon_1^*)) \right], \tag{2.4}
\end{aligned}$$

$t_{\mu\nu}$ describes the polarization of a tensor particle. m_V is the mass of the considered gauge boson. c_1 and c_5 couplings correspond to parity-conserving interaction of a spin-two tensor with the minimal couplings.

2.3.4 Kinematic discriminants based on Matrix Element Method

The spin of the Higgs boson restricts the possible polarization vectors of the decay Z bosons, and these polarization vectors will change helicity amplitudes which determines the angular distributions. Therefore, information about the quantum numbers of the Higgs boson and its couplings to SM fields can be extracted from the angular distributions of the Higgs decay to 4ℓ or $2\ell 2q$ final states.

The four-momenta of $H \rightarrow ZZ \rightarrow 4\ell/2\ell 2q$ decay products carry eight independent

degrees of freedom which fully fix the four-vectors of all involved particles in the system's center-of-mass frame, up to an arbitrary rotation around the beam axis.

There are five angles $\vec{\Omega} \equiv (\theta^*, \Phi_1, \theta_1, \theta_2, \Phi)$ defined in Fig. 2.2, and three invariant masses, the masses of the lepton/quark pairs, m_{Z_1} and m_{Z_2} , and the invariant masses of the 4ℓ or $2\ell 2q$ system.

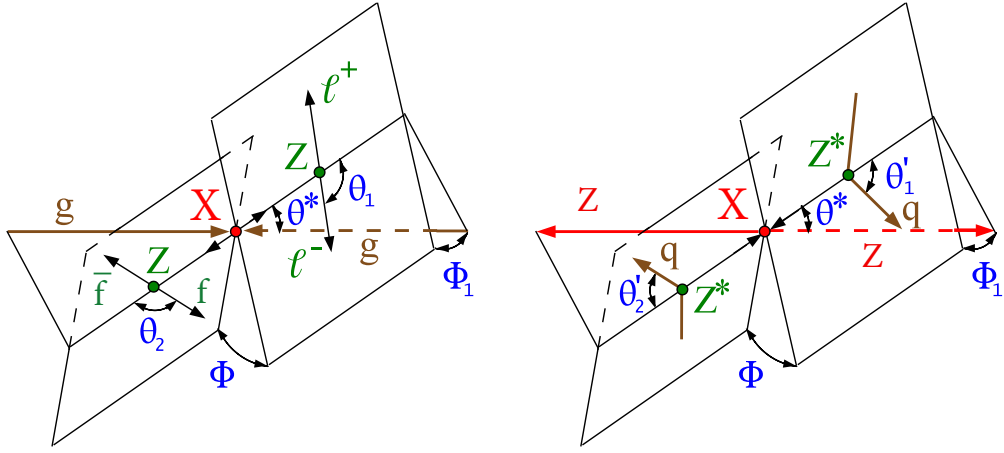


Figure 2.2: Illustration of an X (Higgs or Higgs-like) boson production and decay $gg \rightarrow X \rightarrow ZZ \rightarrow (\ell^+ \ell^-)(f \bar{f})$ (left) and VBF $qq' \rightarrow qq'X$ (right). Angles and invariant masses fully characterize the orientation of the production and decay chain.

Since the final states can be precisely measured, the full decay kinematics can be calculated. The 8 observables can be used to construct a single kinematic discriminant which can effectively discriminate signal from background, categorize the production mechanism, or test alternative signal hypothesis. The probabilities can either be calculated from analytic matrix elements or matrix elements used in generator.

Kinematic discriminants in this thesis are computed using **JHUGen**^{5,10} matrix elements for signal and **MCFM** matrix elements for background processes, both implemented with the **MELA** package.^{5,10}

In the $X \rightarrow ZZ \rightarrow 4\ell$ analysis, the dominant background originates from the $\bar{q}\bar{q} \rightarrow ZZ / Z\gamma^* / \gamma^*\gamma^* \rightarrow 4\ell$ process. Therefore, the discriminant sensitive to the $X \rightarrow ZZ \rightarrow 4\ell$ kinematics and optimal for suppression of the dominant background is defined as

$$\mathcal{D}_{\text{bkg}}^{\text{kin}} = \left[1 + \frac{\mathcal{P}_{\bar{q}\bar{q} \rightarrow 4\ell}(\vec{\Omega}^{X \rightarrow 4\ell} | m_{ZZ})}{\mathcal{P}_{X \rightarrow 4\ell}(\vec{\Omega}^{X \rightarrow 4\ell} | m_{ZZ})} \right]^{-1}. \quad (2.5)$$

In the $X \rightarrow ZZ \rightarrow 2\ell 2q$ analysis, the dominant background originates from the $Z+2\text{jets}$ process. Therefore, the discriminant sensitive to the $X \rightarrow ZZ \rightarrow 2\ell 2q$ kinematics is calculated as

$$\mathcal{D}_{\text{Zjj}} = \left[1 + \frac{\mathcal{P}_{\text{Zjj}}(\vec{\Omega}^{X \rightarrow 2\ell 2q} | m_{ZZ})}{\mathcal{P}_{X \rightarrow 2\ell 2q}(\vec{\Omega}^{X \rightarrow 2\ell 2q} | m_{ZZ})} \right]^{-1}. \quad (2.6)$$

In both Eqs. (2.5) and (2.6), the denominator contains the probability for the signal and the numerator includes the probability for the dominant background process, different in each channel.

The discriminant sensitive to the VBF signal topology with two associated jets is calculated as:

$$\mathcal{D}_{2\text{jet}} = \left[1 + \frac{\mathcal{P}_{\text{XJJ}}(\vec{\Omega}^{X+\text{JJ}} | m_{ZZ})}{\mathcal{P}_{\text{VBF}}(\vec{\Omega}^{X+\text{JJ}} | m_{ZZ})} \right]^{-1}, \quad (2.7)$$

where \mathcal{P}_{VBF} and \mathcal{P}_{XJJ} are probabilities obtained from the **JHUGen** matrix elements for the VBF process and gluon fusion (a combination of gg , $\bar{q}q$, and $\bar{q}q'$ parton colli-

sions) in association with two jets ($X + 2\text{jets}$). This discriminant is equally efficient in separating VBF from either $gg \rightarrow X + 2\text{jets}$ signal or gg or $\bar{q}\bar{q} \rightarrow 2\ell 2\bar{q} + 2\text{jets}$ background because jet correlations in these processes are distinct from the VBF process.

To separate SM signal from an alternative pure J^P state, the $\mathcal{D}_{J^P}^{\text{kin}}$ discriminant is calculated as:

$$\mathcal{D}_{J^P}^{\text{kin}} = \left[1 + \frac{\mathcal{P}_{J^P}(\vec{\Omega}^{X \rightarrow 4\ell} | m_{ZZ})}{\mathcal{P}_{SM}(\vec{\Omega}^{X \rightarrow 4\ell} | m_{ZZ})} \right]^{-1}. \quad (2.8)$$

\mathcal{D}_{bkg}^{dec} and $\mathcal{D}_{J^P}^{\text{kin}}$ can be calculated for alternative spin-1 and spin-2 hypotheses. The discriminants can also be calculated in a way that is independent of the production model. This can be done by integrating over the two production angles $\cos \theta^*$ and ϕ_1 . The production-independent discriminants are denoted by \mathcal{D}_{bkg}^{dec} and $\mathcal{D}_{J^P}^{dec}$.

Chapter 3

Experimental Setup

3.1 The Large Hadron Collider

The Large Hadron Collider (LHC) is the world's largest and highest-energy particle accelerator at present. The LHC consists of a 27km ring of superconducting magnets, and lies in a tunnel 50-175m underground, on the France-Switzerland border. In the accelerator, two high-energy particle beams travel in opposite direction in separate beam pipes, and interact at four points. The beam pipes are kept at ultrahigh vacuum to avoid interaction with gas molecules. About 10 thousand superconducting magnets are installed in LHC. A series of 1232 dipole magnets, each 15m long, are used to guide the beam along the accelerator ring, and 392 quadrupole magnets, each 5-7m long, are used to focus the beam. There are additional stronger quadrupole magnets closer to interaction points and higher multipole order magnets

to correct field geometry. 16 radiofrequency (RF) cavities are used to increase the energy of beam particles by 0.5 MeV/turn. 96 tonnes of liquid helium is used to keep the superconducting magnets at their operating temperature of 1.9K (-271.3C).

The LHC primarily collides proton beams, but it can also perform lead-lead collisions. Each proton is accelerated to the energy of 6.5 TeV (design energy is 7 TeV), giving a total collision energy of 13 TeV. Proton bunches are first formed in the 26 GeV Proton Synchrotron (PS), then accelerated to 450 GeV in the Super Proton Synchrotron (SPS) and ejected into the main LHC ring for acceleration to the target energy.

Besides the colliding energy, the number of particle interactions is also important, especially for rare events with small cross section. In high energy physics, the cross section (σ) is used to measure the probability of a certain process to occur in a given interaction, and luminosity (\mathcal{L}) is the proportionality factor between the the number of events per second ($\frac{dN}{dt}$) and the cross section (σ).

$$\frac{dN}{dt} = \mathcal{L} \cdot \sigma \quad (3.1)$$

In LHC, each beam (30 cm long) are made of 2808 proton bunches, and each bunch contains 1.15×10^{11} protons. The bunches are designed to collide every 25 nanoseconds. The luminosity of LHC can be calculated as below:

$$\mathcal{L} = \frac{N_p^2 k_b f \gamma}{4\pi \epsilon_n \beta^*} F \quad (3.2)$$

where N_p is the number of particles per bunch, k_b is the number of bunches per

Parameter	Symbol	Design Value
Beam Energy	E	7 TeV
β -value at IP	β^*	0.55 m
Bunch Spacing		2.5 ns
Number of Bunches	k_b	2808
Normalized transverse emittance	ϵ_n	3.75 μm
Peak Luminosity	\mathcal{L}	$10^{34} \text{ cm}^{-2}\text{s}^{-1}$
Average Bunch Intensity	N_p	1.15×10^{11}
Number of collisions per bunch crossing		19

Table 3.1: LHC performance-related operational parameter and their nominal values.

beam, f is the revolution frequency, γ is the Lorentz factor, ϵ_n is the normalized transverse emittance, and β is the betatron function at the interaction point, F is the geometrical reduction factor due to the beam crossing angle. The design values of LHC performance related parameters are listed in Table 3.1.⁸ The design luminosity is $10^{34} \text{ cm}^{-2}\text{s}^{-1}$, leading to around 1 billion proton-proton interactions per second.

The proton beams are made to collide at the sites of four detectors: CMS, ATLAS, ALICE and LHCb, among which CMS and ATLAS are two general purpose detectors, LHCb focus on the physics of b quark and ALICE is optimized to study quark-gluon plasma using heavy-ion collisions.

3.2 The Compact Muon Solenoid

The Compact Muon Solenoid (CMS) is one of the two general purpose experiments at the LHC, which involves various physics analysis, such as study of the Standard Model (including Higgs Boson), search for supersymmetric particles, search for new massive vector bosons and extra dimensions. As the name indicates, the CMS detector is a compact detector built around a superconducting solenoid, with a high performance system to measure muons. The detector is compactly designed with layers of materials to measure the energy and momentum of different particles. It has a length of 21.6 m, a diameter of 14.6 m and a total weight of 12500 tons. The solenoid in the heart of CMS is 13 m long, 5.9 m in inner diameter, and generates a magnetic field of 4T, which is needed to provide good resolution for high momentum particles. There is a muon detector to provide precise measurement for muons, an electromagnetic calorimeter to precisely measure electrons and photons, an inner tracking system to provide high momentum resolution and reconstruction efficiency for all charged particles, and a "hermetic" hadron calorimeter to measure jet mass and missing transverse energy. The overall layout of CMS is shown in Figure 3.1. The overview of all subsystems in CMS will be illustrated in this section.

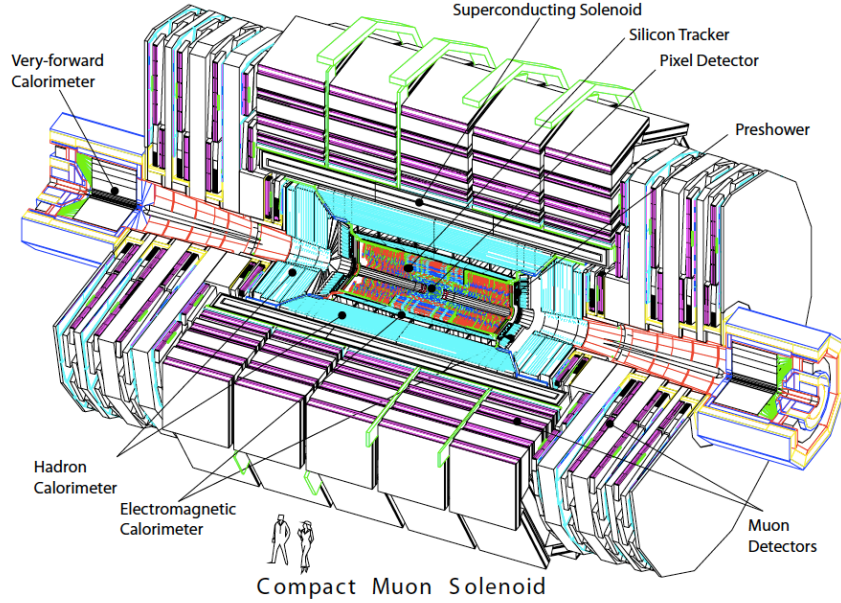


Figure 3.1: CMS detector

3.2.1 Coordinate Conventions

The origin of the coordinate system is centered at the nominal collision point, with the y-axis pointing vertically upward, the x-axis pointing radially inward toward the center of LHC, and the z-axis pointing along the beam direction. The azimuthal angle ϕ is measured from x-axis in the x-y plane and the polar angle θ is measured from the z-axis in y-z plane. Pseudorapidity is defined as $\eta = -\ln \tan(\theta/2)$. The transverse momentum (p_T) and transverse energy (E_T) are measured as the component transverse to the beam direction. The missing transverse momentum or energy is measured from the imbalance of momentum or energy in the transverse plane.

Field	4T
Inner Bore	5.7 m
Length	12.9 m
Number of Turns	2168
Current	19.5 kA
Stored Energy	2.7 GJ
Hoop Stress	64 atm

Table 3.2: Parameters of the CMS superconducting solenoid.

3.2.2 The Magnet

Since the momentum and sign of charged particle is determined by the curvature and direction of the particle in a magnetic field, strong magnet is needed for high resolution in momentum measurement. CMS uses a large superconducting solenoid to provide a large bending power, with the parameters given in Table 3.2.

Inner tracker and the calorimeter detectors fits inside the magnet coil, while muons chambers and iron return yoke surround the magnet coils, contain and guide the field.

3.2.3 Inner Tracker

The inner tracker of CMS is made entirely of silicon, and placed closest to the beam line with largest particle flux. It is used to precisely measure particle momentum and

to reconstruct interaction vertices. It is subdivided into two silicon pixel subdetectors, the Tracker Pixel Barrel (TPB), the Tracker Pixel Endcap (TPE), and four silicon strip subdetectors, the Tracker Outer Barrel (TOB), the Tracker Inner Barrel (TIB), the Tracker Inner Disks (TID), and the Tracker Endcap (TEC). All active components are contained in a cylindrical volume with a length of 5.4 m and a diameter of 2.4 m. To prevent thermal runaway caused by radiation damage, dry nitrogen is used to keep the tracker at a temperature of about $-10\text{ }^{\circ}\text{C}$. The r-z view of CMS Tracker is shown in Figure 3.2

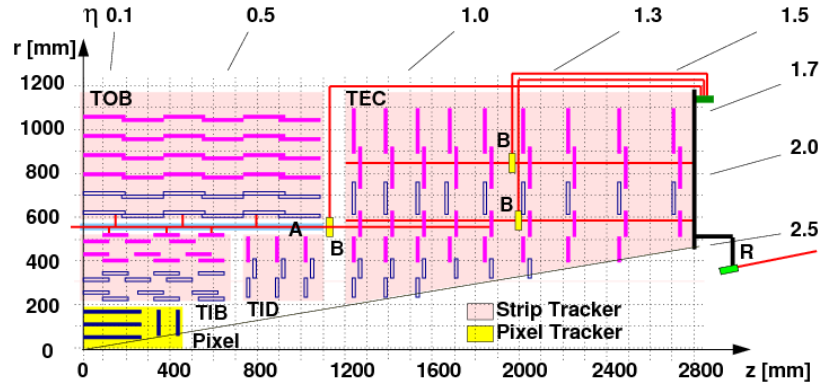


Figure 3.2: A quarter of the CMS inner tracker, in r-z view. The single-sided strip modules are in solid magenta lines, and the double-sided strip modules are in open blue lines. Pixel modules are in solid blue lines.

3.2.3.1 Pixel Detector

Silicon pixel detector is placed closest to the interaction point. It consists of 66 millions pixels of size $100 \times 150\mu\text{m}^2$ in 1440 modules.

In the barrel region, there are three layers of pixel detectors at the radii of 4.4 ,7.3 and 10.2 cm. The 768 modules in barrel region are arranged into half-ladders with 4 modules each. The high Lorentz angle (23°) increases the electron cloud width in the silicon bulk and generates charge sharing between adjacent pixels which is used to improve $r\phi$ resolution.

In the forward region there are two endcap disks at $|z| = 34.5$ and 46.5 cm. The 672 modules in forward region are arranged into blades with 7 modules each. The blades are rotated by 20° to benefit from Lorentz effect.

The spatial resolution for pixel detector is about $10\mu\text{m}$ in $r\phi$ direction, and $20\mu\text{m}$ in z direction.

3.2.3.2 Strip Detector

The strip detector consists of 9.6 million microstrips in 15128 modules. The thickness of strip sensor ranges from $320\mu\text{m}$ to $500\mu\text{m}$ and the strip pitch (distance between strips) ranges from $80\mu\text{m}$ to $205\mu\text{m}$.

The barrel region is divided into two parts, the Tracker Inner Barrel (TIB) with 4 layers, and the Tracker Outer Barrel (TOB) with 6 layers. The endcap region is divided into Tracker Inner Disk (TID) with 3 disks, and Tracker End Cap (TEC) with 9 disks. The innermost two layers in TIB and TOB, the innermost two rings in TID, and the innermost two rings and the fifth ring in TEC have "stereo" modules. In the stereo module, two single-sides strip modules are mounted back-to-back with a stereo

angle of 100 mrad, providing measurements in both $r\phi$ and rz coordinates. Therefore, each track from the collision can have at least four two-dimensional measurements.

3.2.4 Electromagnetic Calorimeter

The Electromagnetic Calorimeter (ECAL) is used to measure the energy of electrons and photons. The ECAL is made up of a barrel section (EB) and two endcaps (EE). The barrel section has a inner radius of 129cm, and covers the pseudorapidity range of $0 < |\eta| < 1.48$. It is organized into 36 “supermodules”, with a total of 61,200 lead tungstate (PbWO_4) crystals. The endcaps are at a distance of 314 cm from the vertex and cover the pseudorapidity range of $1.48 < |\eta| < 3$. There are 7,324 crystals in each of the two endcaps. The ECAL also contains Preshower detectors which is positioned in front of endcaps. It covers a pseudorapidity range from $|\eta| = 1.65$ to 2.61. It’s main task is to provide $\pi^0 - \gamma$ separation.

Lead tungstate “scintillates” when particles pass through it, and produce photon bursts proportional to the particle’s energy. The crystal has a square cross-section of side length 22 – 25 mm, matching the Moliere radius of 21.9 mm. The length of the crystal is 220-230 mm. The small Moliere radius reduce the pileup effect by reducing the area over which the energy is summed. In addition, PbWO_4 has short radiation length(0.89 cm), fast response (average decay time of 10 ns) and is radiation hard (10 Mrad).

Photodetectors are attached to the back of each crystal, and convert the scin-

tillation light to amplified electrical signals. Due to the low light yield of PbWO_4 , unity gain devices cannot provide the noise performance needed. Silicon avalanche photodiodes (APDs), which operates at gains of 50-100, are used in barrel. In addition, the high radiation environment in the forward regions excludes the possibility of solid-state and hybrid devices in endcaps. Vacuum phototriodes (VPTs), operates at gains of 10, are used in the endcaps. The energy deposited in the crystals is converted into digital form and stored every 25ns, then the digital values in each trigger tower is used by the level 1 calorimeter trigger.

The energy resolution of ECAL supermodules can be measured using test beams. By fitting a Gaussian function to the reconstructed energy distributions, the energy resolution can be parameterized as :

$$\left(\frac{\sigma}{E}\right)^2 = \left(\frac{S}{\sqrt{E}}\right)^2 + \left(\frac{N}{E}\right)^2 + C^2 \quad (3.3)$$

where S is a stochastic term, N is the noise, and C is a constant term. The values of fitted parameters are listed in Figure 3.3

3.2.5 Hadronic Calorimeter

The Hadronic Calorimeter (HCAL) measures the energy of “hadrons” (particles made of quarks and gluons). It also provides good containment and hermeticity for measurement of missing transverse energy E_T^{miss} , which indicates the presence of non-interacting, uncharged particles such as neutrinos. To capture the energy of all

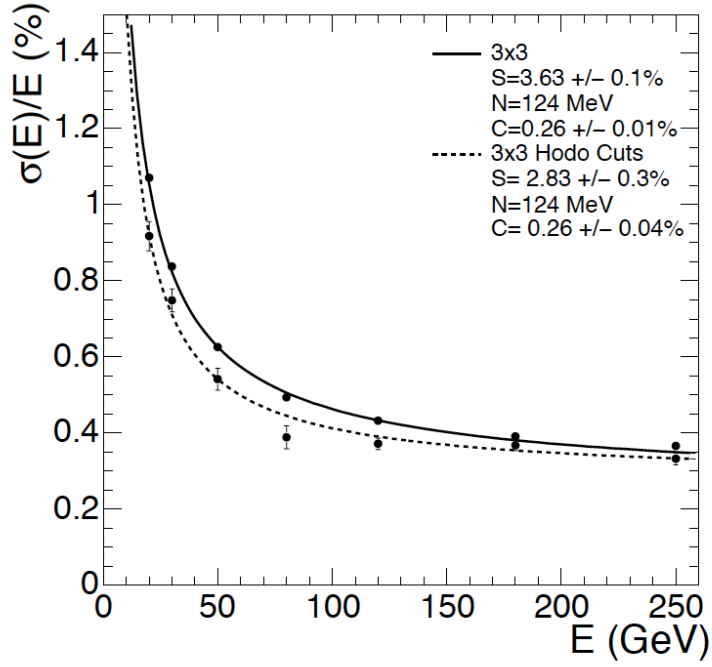


Figure 3.3: ECAL supermodule energy resolution. The upper series of points correspond to events taken with a $20 \times 20 \text{ mm}^2$ trigger, while the lower series of points correspond to events taken with a $4 \times 4 \text{ mm}^2$ trigger.

particles emerging from collision, HCAL is built in a staggered fashion to ensure that there are no gaps in direct lines from the origin.

The HCAL is a sampling calorimeter, with alternating layers of absorber material and scintillator material. Brass was chosen as absorber material because it is non-magnetic and has short interaction length. Plastic scintillator tiles produce a light pulse when particles pass through, and wave-length shifting fibres carry the light to readout system. The photodetection readout is based on multi-channel hybrid photodiodes. The amount of light is summed over many layers of tiles to measure a particle's energy. HCAL is organized into four sections of hadron barrel (HB), hadron outer barrel (HO), hadron endcap (HE), and hadron forward (HF).

The hadron barrel (HB) part of HCAL consists of 32 towers in two half barrels. There are 15 brass plates of 5 cm thickness. The first scintillator plate has a thickness of 9 mm, while the others have a thickness of 3.7 mm. This optimizes the first scintillator plate to collect 1.5 times higher amount of light than the other plates.

The hadron outer barrel (HO) is physically located outside the solenoid magnet and inside the barrel muon system. The scintillator plates have a thickness of 10 mm. It is used to collect the energy of hadronic showers that leaked through the hadron barrel region. This increase the resolution in measuring missing transverse energy E_T^{miss} .

The hadron endcap (HE) consists of 14 towers and covers the pseudorapidity range of $1.3 < |\eta| < 3$.

The hadron forward calorimeters (HF) covers the pseudorapidity range of $3 < |\eta| < 5$. HF in the very forward region receives the most particle energy in collision, so the material must be very resistant to radiation. Steel absorbers and quartz fibers are used. The quartz fibers measure Cherenkov radiation and channel the signal to photomultipliers. The absorbing structure is made from steel plates.

3.2.6 Muon System

Detecting Muon is one of the most important tasks in CMS. Since muons are 200 times heavier than electrons, they can penetrate the ECAL and HCAL and several meters of iron. Therefore, the muon chambers are placed at the edge of CMS, outside of the solenoid magnet, where muons are the only particles likely to register a signal.

The muon systems is made up of four muon stations interleaved with iron return yoke. Momentum of muon is measured by fitting for track curvature from hits in multiple layers of muon station. When muon p_T is smaller than 200 GeV. The resolution of "muon system only" measurement is dominated by the multiple scattering in the material before the muons exit the coil and enter the first muon station. When muon p_T is higher than 200 GeV, the muon chamber spatial resolution dominates. For low momentum muons, the inner tracker provides the best resolution. The measurements from muon detector and inner tracker can be combined to achieve the best muon momentum resolution. Figure 3.4 shows the muon momentum resolution using muon system only, inner tracker only, or both.

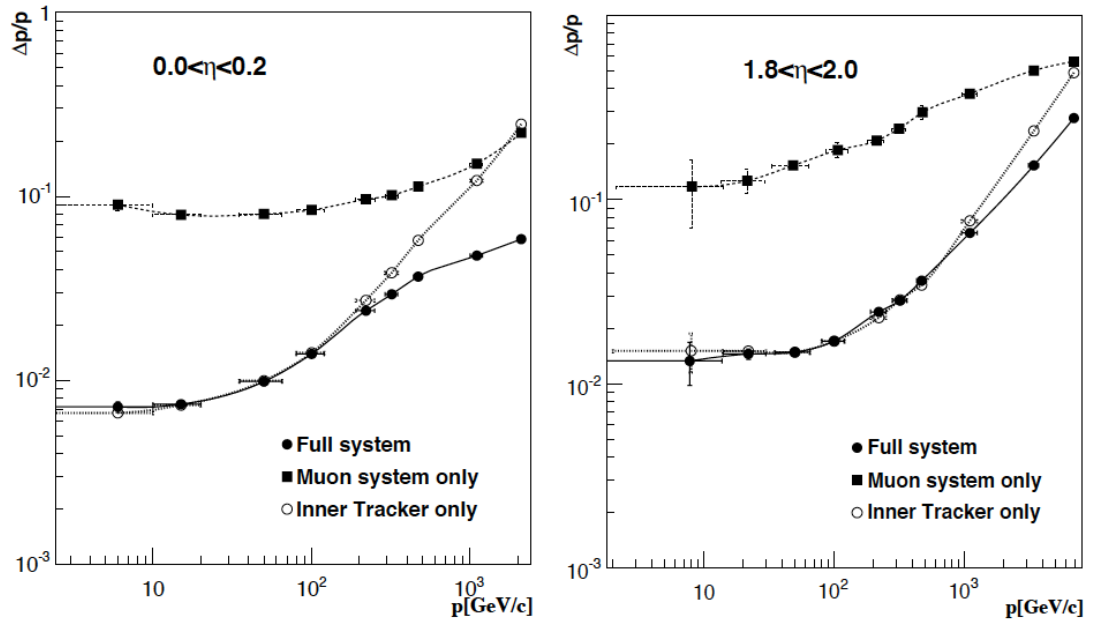


Figure 3.4: The muon momentum resolution versus the momentum, in the barrel region (left) and in endcaps (right).

There are three types of gaseous detectors used in the muon system. Drift tubes (DT) are used in the barrel region, where the muon rate and neutron induced background rate are low, and the magnetic field is also low. Cathode strip chambers (CSC) are used in the endcaps, where we have high muon rate, high neutron induced background rate and high magnetic field. Resistive plate chambers (RPC) are used both in barrel region and endcaps. The detector layout is shown in Figure 3.5.

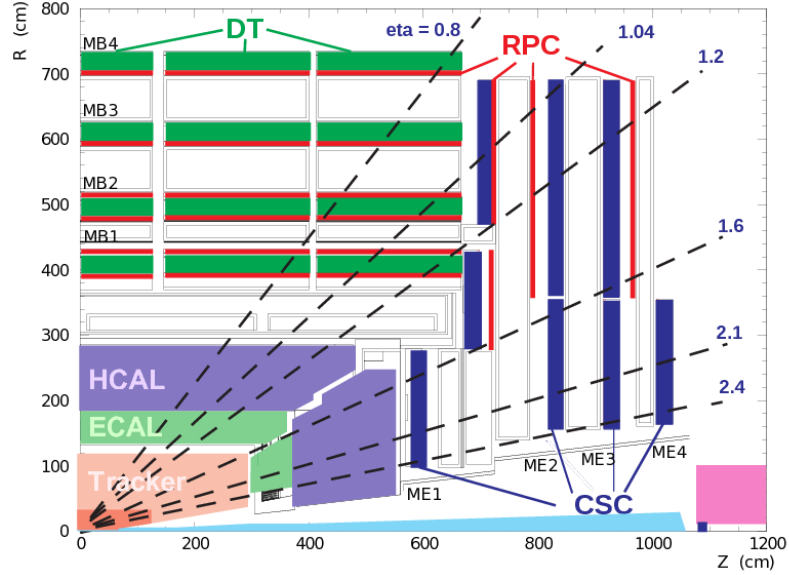


Figure 3.5: Layout of one quarter of the muon system.

3.2.6.1 Muon Drift Tubes

The barrel section consists of drift tube chambers (DT) and resistive plate chambers (RPC), organized in 4 stations (layers). One DT is coupled with one or two RPCs. Muon stations are placed in the iron return yoke, which is divided into 5

wheels and 12 sectors per wheel. Each drift tube chamber has one or two resistive plate chambers coupled to it, so a high p_T muon can cross up to 6 RPCs and 4 DT chambers, with up to 44 hits. The drift tube contains a wire in a gas volume. When charged particles pass through the gas volume, electrons are knocked off the gas atom and move to the anode wires, creating a signal.

3.2.6.2 Cathode Strip Chambers

The endcaps consists of 468 cathode strip chambers (CSC) in the η region $0.9 < |\eta| < 2.4$, and RPCs in the η region $0.9 < |\eta| < 1.6$. Each endcap is divided into 4 disks with 36 azimuthal sectors in each disk. CSCs consists of arrays of anode wires and cathode strips with gas volume, perpendicular to each other. When charged particles pass through, electrons are knocked off the gas atom and travel to the anode wires creating an electron avalanche. Positive ions move toward the cathode strips, creating a charge pulse in the strips. The closely spaced anode wire and cathode strip give two perpendicular coordinates for position measurement. Each CSC module contains 6 layers for precise measurement of muon tracks.

3.2.6.3 Resistive Plate Chambers

CMS uses double-gap resistive chambers. Two parallel high resistivity Bakelite electrodes are separated by a 2 mm gas gap, and the gap is placed on top of another, with a copper readout strips placed in between. They operate at avalanche mode to

have good time resolution at high rates. To identify muon candidates, the pattern of fired RPC strips in subsequent layer is compared with pattern generated by Monte Carlo. The information is used by a trigger to decide if the data is worth keeping.

3.3 Alignment of CMS tracker

The task of CMS tracker is to measure the trajectories of charged particle with high resolution in track position, angle and momentum. Excellent tracking performance is essential for analysis of physics processes. For example, searches for high mass resonances in leptonic final states require good momentum resolution for transverse momenta above 1 TeV. In addition, excellent impact parameter resolution of reconstructed tracks is important for reconstruction of beam spot, primary vertices and b-jet tagging.

Tracker geometry is described by a complete set of parameters describing the geometrical properties (both location and angles) of the modules composing the tracker, and it is an important input for track reconstruction. The uncertainty of tracker geometry should remain below the intrinsic silicon hit resolution of around $10\text{ }\mu\text{m}$ for pixels and $30\text{ }\mu\text{m}$ for strips.

There are many challenges to determine to tracker geometry, such as the limited accessibility of the tracker, the large number of modules to align, the high precision required, and the constant changing in geometry due to changes in environment con-

ditions. Track-based internal alignment is effective in solving these problems, and it is responsible for determining the changes in the positions and angles of the tracker modules relative to each other. Survey measurements of TOB is used to determine its global position relative to the beam axis and the other sub-components are aligned relative to TOB by track-based alignment algorithms.

3.3.1 The Problem

Track-based alignment determines the module positions using the tracks reconstructed from the tracker geometry in situ, because residuals are sensitive to the tracker geometry used in track reconstruction relative to the true positions and angles of tracker modules. It can be treated as a least square minimization problem, where sum of the squares of track-hit residuals from a collection of tracks is minimized.

The objective function to minimize is:¹⁶

$$\chi^2(\mathbf{p}, \mathbf{q}) = \sum_j^{\text{tracks}} \sum_i^{\text{measurements}} \left(\frac{m_{ij} - f_{ij}(\mathbf{p}, \mathbf{q}_j)}{\sigma_{ij}} \right)^2, \quad (3.4)$$

where the measurement m_{ij} is the reconstructed hit positions on the modules, σ_{ij} is uncertainty of the measurement, and f_{ij} is the trajectory prediction of the track model at the position of the measurement, depending on the geometry parameters \mathbf{p} and track parameters \mathbf{q}_j (slope and curvature of the track).

3.3.2 Parameterization

3.3.3 Linear Least Squares Model

Since an initial geometry is used to determine the approximate track parameters, and we assume the corrections from the initial geometry to be small, and the fitted trajectories can be approximated with a straight line in the vicinity of the detector plane.

f_{ij} can be linearized around its initial values:

$$f_{ij}(\mathbf{p} + \Delta\mathbf{p}, \mathbf{q}_j + \Delta\mathbf{q}_j) \simeq f_{ij}(\mathbf{p}, \mathbf{q}_j) + \left(\frac{\partial f_{ij}}{\partial \mathbf{p}}\right)^T \Delta\mathbf{p} + \left(\frac{\partial f_{ij}}{\partial \mathbf{q}_j}\right)^T \Delta\mathbf{q}_j \quad (3.5)$$

We can combine geometry and track parameters as a vector \mathbf{r} and write residual in vector form:

$$\boldsymbol{\varepsilon}(\mathbf{r} + \Delta\mathbf{r}) \simeq \boldsymbol{\varepsilon}(\mathbf{r}) + \mathbf{A}^T \Delta\mathbf{r} \quad (3.6)$$

where $\boldsymbol{\varepsilon}(\mathbf{r})$ is the initial residual and $\boldsymbol{\varepsilon}(\mathbf{r} + \Delta\mathbf{r})$ is the residual with corrected parameters. \mathbf{A} is the Jacobian matrix $\mathbf{A} = \nabla_{\mathbf{r}} \boldsymbol{\varepsilon}(\mathbf{r})$. For simplicity, $\boldsymbol{\varepsilon}(\mathbf{r})$ will be denoted $\boldsymbol{\varepsilon}$ below.

The objective function Eq.3.4 becomes:⁹

$$\chi^2(\mathbf{r} + \Delta\mathbf{r}) \simeq (\boldsymbol{\varepsilon} + \mathbf{A}^T \Delta\mathbf{r})^T \mathbf{V}^{-1} (\boldsymbol{\varepsilon} + \mathbf{A}^T \Delta\mathbf{r}) \quad (3.7)$$

where \mathbf{V} is the covariance matrix of the measurements.

To derive the optimal correction vector $\Delta\mathbf{r}$ for minimization, we can simply differentiate the objective function w.r.t. $\Delta\mathbf{r}$ and equating to zero. This leads to the

normal equations to the linear least square solutions:

$$\mathbf{A}\mathbf{V}^{-1}\boldsymbol{\varepsilon} + (\mathbf{A}\mathbf{V}^{-1}\mathbf{A}^T)\Delta\mathbf{r} = 0 \quad (3.8)$$

or

$$\mathbf{C}\Delta\mathbf{r} = \mathbf{d} \quad (3.9)$$

where the symmetric matrix $\mathbf{C} = \mathbf{A}\mathbf{V}^{-1}\mathbf{A}^T$ and the vector $\mathbf{d} = -\mathbf{A}\mathbf{V}^{-1}\boldsymbol{\varepsilon}$.

To solve for the optimal correction $\Delta\mathbf{r}$, the straightforward way is to invert the matrix \mathbf{C} . However, there are 16588×6 geometry parameters and millions of track parameters, leading to a huge n-by-n matrix \mathbf{C} with $n > 10^5$. The computing time is $O(n^3)$ for matrix inversion, so the solution in this form is not practical in terms of computing time and storage space.

It's also important to note that sometimes the residuals depend non-linearly on the track parameters. In this case a few iterations are needed.

3.3.4 Matrix Partitioning

The huge n-by-n matrix \mathbf{C} in Eq.3.9 can be partitioned into four submatrices:

$$\mathbf{C} = \left(\begin{array}{c|c} \mathbf{B} & \mathbf{G} \\ \hline \mathbf{G}^T & \mathbf{\Gamma} \end{array} \right) \quad (3.10)$$

Where the submatrix \mathbf{B} is the symmetric p-by-p Hessian matrix for geometry parameters (p is the number of geometry parameters), the submatrix $\mathbf{\Gamma}$ is the symmetric q-by-q Hessian matrix for track parameters (q is the number of track parameters),

and the submatrix \mathbf{G} is a q-by-p matrix relating the geometry parameters to track parameters. Since the tracks are independent of each other, $\mathbf{\Gamma}$ is mostly diagonal, i.e. only the hits on the same track are correlated.

The matrix equation Eq.3.9 can be written in the form

$$\left(\begin{array}{c|c} \mathbf{B} & \mathbf{G} \\ \hline \mathbf{G}^T & \mathbf{\Gamma} \end{array} \right) \left(\begin{array}{c} \Delta \mathbf{p} \\ \hline \Delta \mathbf{q} \end{array} \right) = \left(\begin{array}{c} \mathbf{b} \\ \hline \boldsymbol{\beta} \end{array} \right) \quad (3.11)$$

Inverting the entire matrix \mathbf{C} can be simplified by performing the block Gaussian elimination shown below.

The product of \mathbf{C} with the lower triangular matrix \mathbf{L} (defined below) can be written as the product of an upper triangular matrix \mathbf{U} and a diagonal matrix \mathbf{D} :

$$\begin{aligned} \mathbf{CL} &= \left(\begin{array}{c|c} \mathbf{B} & \mathbf{G} \\ \hline \mathbf{G}^T & \mathbf{\Gamma} \end{array} \right) \left(\begin{array}{c|c} \mathbf{I}_p & \mathbf{0} \\ \hline -\mathbf{\Gamma}^{-1}\mathbf{G}^T & \mathbf{I}_q \end{array} \right) \\ &= \left(\begin{array}{c|c} \mathbf{B} - \mathbf{G}\mathbf{\Gamma}^{-1}\mathbf{G}^T & \mathbf{G} \\ \hline \mathbf{0} & \mathbf{\Gamma} \end{array} \right) \\ &= \left(\begin{array}{c|c} \mathbf{I}_p & \mathbf{G}\mathbf{\Gamma}^{-1} \\ \hline \mathbf{0} & \mathbf{I}_q \end{array} \right) \left(\begin{array}{c|c} \mathbf{B} - \mathbf{G}\mathbf{\Gamma}^{-1}\mathbf{G}^T & \mathbf{0} \\ \hline \mathbf{0} & \mathbf{\Gamma} \end{array} \right) = \mathbf{UD} \end{aligned} \quad (3.12)$$

In this way we find a LDU decomposition for the block matrix \mathbf{C} :

$$\mathbf{C} = \mathbf{UDL}^{-1} = \left(\begin{array}{c|c} \mathbf{I}_p & \mathbf{G}\mathbf{\Gamma}^{-1} \\ \hline \mathbf{0} & \mathbf{I}_q \end{array} \right) \left(\begin{array}{c|c} \mathbf{B} - \mathbf{G}\mathbf{\Gamma}^{-1}\mathbf{G}^T & \mathbf{0} \\ \hline \mathbf{0} & \mathbf{\Gamma} \end{array} \right) \left(\begin{array}{c|c} \mathbf{I}_p & \mathbf{0} \\ \hline \mathbf{\Gamma}^{-1}\mathbf{G}^T & \mathbf{I}_q \end{array} \right) \quad (3.13)$$

and the inverse of \mathbf{C} can be expressed as:

$$\mathbf{C}^{-1} = \mathbf{L}\mathbf{D}^{-1}\mathbf{U}^{-1} = \left(\begin{array}{c|c} \mathbf{I}_p & \mathbf{0} \\ \hline -\mathbf{\Gamma}^{-1}\mathbf{G}^T & \mathbf{I}_q \end{array} \right) \left(\begin{array}{c|c} (\mathbf{B} - \mathbf{G}\mathbf{\Gamma}^{-1}\mathbf{G}^T)^{-1} & \mathbf{0} \\ \hline \mathbf{0} & \mathbf{\Gamma}^{-1} \end{array} \right) \left(\begin{array}{c|c} \mathbf{I}_p & -\mathbf{G}\mathbf{\Gamma}^{-1} \\ \hline \mathbf{0} & \mathbf{I}_q \end{array} \right) \quad (3.14)$$

The inverse of \mathbf{C} is now expressed in terms of two inverses of smaller matrices $(\mathbf{B} - \mathbf{G}\mathbf{\Gamma}^{-1}\mathbf{G}^T)$ and $\mathbf{\Gamma}$. $(\mathbf{B} - \mathbf{G}\mathbf{\Gamma}^{-1}\mathbf{G}^T)$ is the Schur complement \mathbf{C}/\mathbf{B} of block \mathbf{B} in matrix \mathbf{C} , and it will be denoted as \mathbf{S} matrix below.

Expand Eq.3.14 to get the inverse of \mathbf{C} , and solve for the optimal correction in Eq.3.11 :

$$\begin{pmatrix} \Delta \mathbf{p} \\ \Delta \mathbf{q} \end{pmatrix} = \begin{pmatrix} \mathbf{S}^{-1} & -\mathbf{S}^{-1}\mathbf{G}\mathbf{\Gamma}^{-1} \\ \hline -\mathbf{\Gamma}^{-1}\mathbf{G}^T\mathbf{S}^{-1} & \mathbf{\Gamma}^{-1} - \mathbf{\Gamma}^{-1}\mathbf{G}^T\mathbf{S}^{-1}\mathbf{G}\mathbf{\Gamma}^{-1} \end{pmatrix} \begin{pmatrix} \mathbf{b} \\ \beta \end{pmatrix} \quad (3.15)$$

This gives two set of equations, one for correction in geometry parameters (tracker alignment) and the other for correction for track parameters (track fitting):

$$\Delta \mathbf{p} = \mathbf{S}^{-1}(\mathbf{b} - \mathbf{G}\mathbf{\Gamma}^{-1}\beta) \quad (3.16)$$

$$\Delta \mathbf{q} = (-\mathbf{\Gamma}^{-1}\mathbf{G}^T\mathbf{S}^{-1})\mathbf{b} + (\mathbf{\Gamma}^{-1} - \mathbf{\Gamma}^{-1}\mathbf{G}^T\mathbf{S}^{-1}\mathbf{G}\mathbf{\Gamma}^{-1})\beta \quad (3.17)$$

It will be ideal to solve simultaneously for both geometry and track parameters, but it's not possible given the large the size of matrices. For tracker alignment, we are most interested in the geometry parameters $\Delta \mathbf{p}$, i.e. to solve Eq.3.16. In order to do this, the first step is to build all the matrices and vectors from the measurements. An initial track fitting is required, which means we need to get an approximate solution for Eq.3.17.

3.3.5 Single Track Fit

Starting from Eq.3.17, we make the assumption that the residuals are independent of geometry parameters. This approximation assumption not always valid. If the starting tracker geometry has large deviation from the true tracker geometry, the track parameters calculated under this assumption will be too biased, and can lead to more biased geometry parameters calculated in Section 3.3.7. Furthermore, the entire linear least square model will fail with a poor starting geometry.

This assumption leads to a much simplified equation, with matrices \mathbf{B} , \mathbf{G} and the vector \mathbf{b} being set to zero. Eq.3.17 becomes:

$$\Delta \mathbf{q} = \mathbf{\Gamma}^{-1} \boldsymbol{\beta} \quad (3.18)$$

It has been mentioned that the track parameters of different tracks are independent of each other, and the matrix $\mathbf{\Gamma}$ is a diagonal block matrix made of block $\mathbf{\Gamma}_j$ for each track. Therefore, we can fit an individual track, independent of other tracks. Instead of solving for $\Delta \mathbf{q}$, the track parameters $\Delta \mathbf{q}_j$ for track j will be solved.

$$\Delta \mathbf{q}_j = \mathbf{\Gamma}_j^{-1} \boldsymbol{\beta}_j$$

$$\mathbf{\Gamma}_j = \sum_i^{\text{hits}} \left(\frac{\partial f_{ij}}{\partial \mathbf{q}_j} \right)^T \left(\frac{\partial f_{ij}}{\partial \mathbf{q}_j} \right) \frac{1}{\sigma_{ij}^2} \quad \text{and} \quad \boldsymbol{\beta}_j = \sum_i^{\text{hits}} \left(\frac{\partial f_{ij}}{\partial \mathbf{q}_j} \right)^T \frac{\varepsilon_{ij}}{\sigma_{ij}^2} \quad (3.19)$$

The track parameter is updated to $\mathbf{q}_j + \Delta \mathbf{q}_j$, then $\mathbf{\Gamma}_j$ and $\boldsymbol{\beta}_j$ are also updated. The fitting process is repeated until convergence is reached ($\boldsymbol{\beta}_j$ becomes negligible).

3.3.6 Build the Matrices

After the fitting of all tracks, we can use them to construct all the matrices and vectors in Eq.3.16 to solve for geometry parameters.

Using the converged covariance matrix $\mathbf{\Gamma}_j$ from each track, the full $\mathbf{\Gamma}$ matrix is formed by:

$$\mathbf{\Gamma} = \left(\begin{array}{c|c|c} \mathbf{\Gamma}_1 & \mathbf{0} & \mathbf{0} \\ \hline \mathbf{0} & \ddots & \mathbf{0} \\ \hline \mathbf{0} & \mathbf{0} & \mathbf{\Gamma}_j \end{array} \right) \quad (3.20)$$

The q-vector $\boldsymbol{\beta}$ is given by:

$$\boldsymbol{\beta} = \begin{pmatrix} \beta_1 \\ \vdots \\ \beta_j \end{pmatrix} \quad (3.21)$$

The $p \times p$ matrix \mathbf{B} and the p-vector \mathbf{b} of the geometry parameters in Eq.3.11 can be formed by summing up contributions from all measurements of all tracks:

$$\mathbf{B} = \sum_j^{\text{tracks}} \sum_i^{\text{hits}} \left(\frac{\partial f_{ij}}{\partial \mathbf{p}} \right)^T \left(\frac{\partial f_{ij}}{\partial \mathbf{p}} \right) \frac{1}{\sigma_{ij}^2} \quad (3.22)$$

$$\mathbf{b} = \sum_j^{\text{tracks}} \sum_i^{\text{measurements}} \left(\frac{\partial f_{ij}}{\partial \mathbf{p}} \right)^T \frac{\varepsilon_{ij}}{\sigma_{ij}^2} \quad (3.23)$$

For each track j , a rectangular $p \times q_j$ matrix \mathbf{G}_j , which correlate the track parameters with the geometry parameters can be formed by summing over all measurements of that track:

$$\mathbf{G}_j = \sum_i^{\text{hits}} \left(\frac{\partial f_{ij}}{\partial \mathbf{p}} \right)^T \left(\frac{\partial f_{ij}}{\partial \mathbf{q}_j} \right) \frac{1}{\sigma_{ij}^2} \quad (3.24)$$

The full correlation matrix \mathbf{G} of dimension $p \times q$ is formed by joining them horizontally:

$$\mathbf{G} = (\mathbf{G}_1 \cdots \mathbf{G}_q) \quad (3.25)$$

3.3.7 The Approximate Solutions - Tracker Alignment Algorithms

Two approaches to determine the alignment (geometry) parameters are in use at CMS. One is the local approach, implemented in HipPy package, and the other one is the global approach, implemented in the MillePede-II package.

3.3.7.1 Local Approach

The local approach solves the alignment problem iteratively.²⁵ The correlation between geometry parameters and track parameters is ignored within one iteration, but it is taken into account when the single track fitting procedure in Section 3.3.6 is repeated and the alignment parameters are re-calculated for many iterations. Generally the correction step gets smaller and smaller, and the final geometry converges after 10 to 20 iterations.

There are cases when the convergence to true geometry cannot be reached within reasonable number of iterations, especially when the starting geometry is far away and the track number is small. This sometimes happens when the detector starts a new run, and the small collection of tracks available was reconstructed with a

very different old geometry. Many methods can be used to improve the performance and avoid deviating from true geometry, such as hierarchical alignment, differential alignment, adding constraints and properly mixing track collections, which will be discussed in the following sections. There is also a requirement of minimum number of hits on each detector module for its geometry to be updated, and a threshold on the final alignment uncertainly.

The matrix \mathbf{G} accounts for the correlation between track parameters and geometry parameters, and it is approximated to be zero in the local approach. The normal equations for geometry parameter correction Eq.3.16 is simplified to:

$$\Delta \mathbf{p} = \mathbf{B}^{-1} \mathbf{b} \quad (3.26)$$

We can further simplify the problem by solving the correction for each detector module independently, and take care of the correlation between detectors by multiple iterations.

For a single detector module, the geometry parameter is of dimension 6, as mentioned in Section 3.2.3:

$$\Delta \mathbf{p} = (\Delta u, \Delta v, \Delta w, \Delta \alpha, \Delta \beta, \Delta \gamma) \quad (3.27)$$

where the u-axis is along the precise coordinate of the sensor plane, the v-axis along the course coordinate, and the w-axis normal to the sensor. The angles α , β and γ are rotations around the axes u,v and w.

In stereo strip detectors and pixel detectors, each hit has two measurements, u_m

and v_m , and in the non-stereo strip detectors there is only one measurement u_m .

Without loss of generality, we consider the first case.

The residual is a 2-vector for a hit on a specific detector module:

$$\boldsymbol{\varepsilon} = \begin{pmatrix} \varepsilon_u \\ \varepsilon_v \end{pmatrix} = \begin{pmatrix} u_m - u_f \\ v_m - v_f \end{pmatrix} \quad (3.28)$$

It can be shown that the 6×2 Jacobian matrix for f_{ij} , the measurement i from track j , has the form below:

$$\nabla_{\mathbf{p}} f = \begin{pmatrix} \frac{\partial f_u}{\partial u} & \frac{\partial f_v}{\partial u} \\ \frac{\partial f_u}{\partial v} & \frac{\partial f_v}{\partial v} \\ \frac{\partial f_u}{\partial w} & \frac{\partial f_v}{\partial w} \\ \frac{\partial f_u}{\partial \alpha} & \frac{\partial f_v}{\partial \alpha} \\ \frac{\partial f_u}{\partial \beta} & \frac{\partial f_v}{\partial \beta} \\ \frac{\partial f_u}{\partial \gamma} & \frac{\partial f_v}{\partial \gamma} \end{pmatrix} = \begin{pmatrix} -1 & 0 \\ 0 & -1 \\ \tan \psi & \tan \theta \\ v_x \tan \psi & v_x \tan \theta \\ u_x \tan \psi & u_x \tan \theta \\ v_x & -u_x \end{pmatrix} \quad (3.29)$$

where ψ is the angle between the track and the vw -plane, and θ is the angle between the track and the uw -plane.

So the matrix \mathbf{B} (6×6 for a single track module) and vector \mathbf{b} (2-vector) can easily be calculated following Eq.3.22.

The iterative correction $\Delta \mathbf{p}$ can be solved by Equation 3.26, by simply inverting a 6×6 matrix.

HipPy alignment algorithm is one of two major tracker alignment algorithms in

CMS. The performance can be demonstrated by the 0 T cosmic ray (CRUZET) alignment in 2016. About 0.2 million cosmic tracks with 3.6 million hits with no magnetic field are used. The alignment is done at high level, aligning 6 detector units, which means there are only 6×6 geometry parameters, and the coordinates are the same as global tracker coordinate. For this alignment campaign, 20 iterations are used.

The iterative correction in all parameters in each iterations is shown in Figure 3.6. It shows that the most significant movement is in z direction of BPIX, and the correction converge to small values in the end, which means the final geometry is stable. This kind of plot is referred to as “convergence plot” for HipPy.

The convergence plot for a module level alignment is shown in Figure 3.7. Alignment corrections pixel barrel detector (BPIX) is plotted, with each line correspond to one of the BPIX modules. Since v is along the course direction, the convergence is worse than that of u direction, but it reaches the desired accuracy of $10\mu\text{m}$. The β direction is not aligned in this specific alignment.

The total correction relative to the initial geometry is shown in Figure 3.8. This is also referred to as “shift plot” for HipPy. It gives the similar information as “convergence plot”, but provide a clearer view of the total movement. Here we see that the BPIX moved by about $130\mu\text{m}$ in z direction.

The alignment uncertainty is obtained for each iteration, and the percentage error for each detector module is calculated and used to determine if the geometry of that

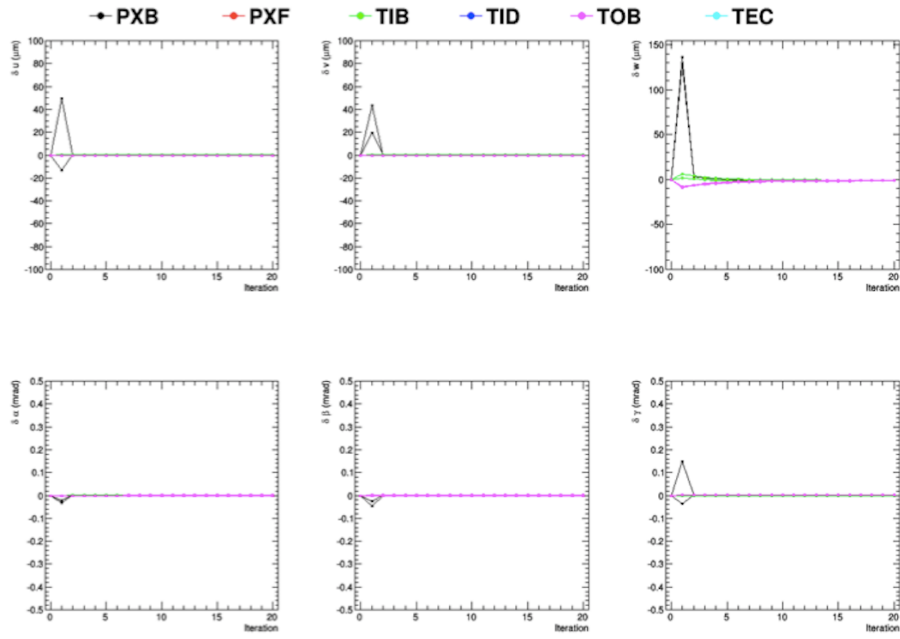


Figure 3.6: The convergence plot for 2016 CRUZET alignment, using HipPy package.

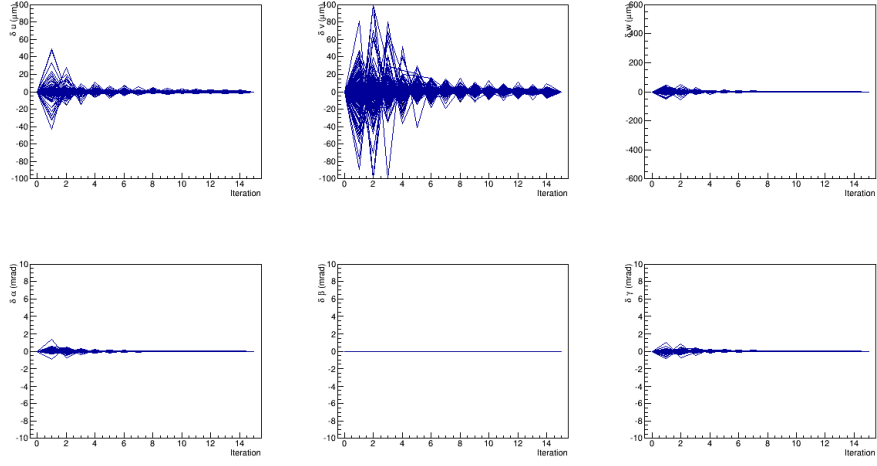


Figure 3.7: The convergence plot for module level alignment, using HipPy package.

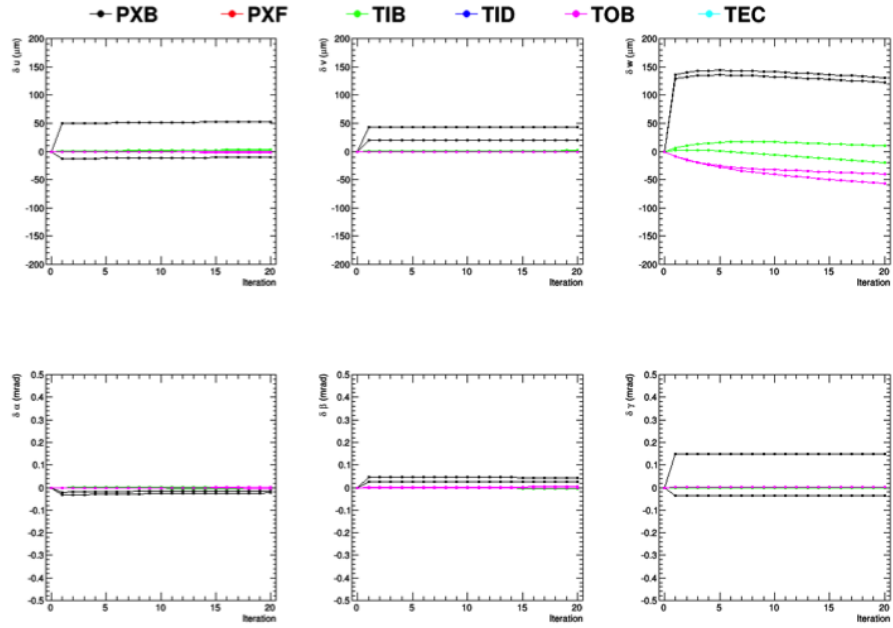


Figure 3.8: The shift plot for 2016 CRUZET alignment, using HipPy package.

module will be updated in that iteration. The alignment parameters with error bars is plotted for the final iteration as shown in Figure 3.9 for high level alignment.

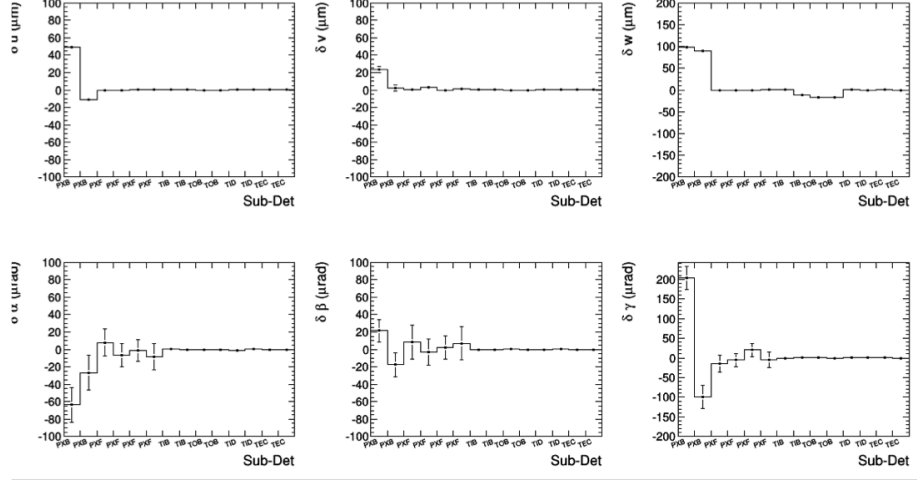


Figure 3.9: The fitted parameters with error in 2016 CRUZET alignment, using HipPy package.

3.3.7.2 Global Approach

The global approach solves the alignment problem in a single step (or a few iterations when needed). It takes into account the correlation between track parameters and geometry parameters (matrix \mathbf{G}), as well as the correlation between geometry parameters (full matrix \mathbf{B}). It is close to but not an exact solution to the normal equations Equation 3.16, because it follows the same procedure of first fitting the single tracks based on the initial geometry, rather than fitting the track parameters together with the geometry parameters, so possible bias could be introduced in constructing

matrices \mathbf{B} and \mathbf{G} .

The full $\mathbf{\Gamma}$ matrix needs to be inverted in order to construct the Schur complement \mathbf{S} to matrix \mathbf{B} , and the inverse of the Schur complement \mathbf{S} itself needs to be calculated in the end to determine the corrections. Both $\mathbf{\Gamma}$ and \mathbf{S} are large sparse matrices given that millions of tracks are used.

3.3.8 Alignment Strategies

There are certain patterns of CMS tracker geometry that can be used to reduce the computing time and improve the alignment accuracy. Instead of solving the problem directly, two main strategies are used in routine alignments.

3.3.8.1 Hierarchical Alignment

The alignment purpose is to determine the positions of all modules of the tracker, but the alignment procedure can be performed at any hierarchy levels. i.e. different substructures of the detector. For example, the barrel pixel is made of two half barrels, which are made of three layer with each layer made of several ladders, and on each ladder, 8 modules are mounted on top. Alignment can be done at any of these “levels”. To treat the translation and rotation of the substructure as a whole, the geometry parameters of each level of substructure can be defined, and the correlation between track measurements and these parameters can be obtained. This leads to a modified version of Equation 3.29:

$$\nabla_{\mathbf{p}_h} f = \frac{\partial \mathbf{p}}{\partial \mathbf{p}_h} \cdot \nabla_{\mathbf{p}} f \quad (3.30)$$

where $\frac{\partial \mathbf{p}}{\partial \mathbf{p}_h}$ is the 6×6 Jacobian matrix relating the translation and rotation of high level structures to the movement of each module in local module coordinates.

The alignment of high level structure is very useful when the number of tracks is insufficient for determining the position of each module, or when there's a significant “weak mode” in module level alignment. “Weak modes” will be described in more detail in Section 3.3.9.

In the iterative local approach, higher-level alignment is usually done before the full module-level alignment, for faster and better convergence. In the global approach, the higher-level alignment can be done simultaneous with the module-level alignment, and linear equality constraints are used to eliminate redundant degrees of freedom, by means of Lagrangian multipliers. The substructure selected for higher-level alignment depends on the number of tracks available, and the specific alignment goals.

3.3.8.2 Differential Alignment

The “differential alignment” or “multi-IOV alignment” means some of the alignment parameters are treated as time-dependent, while the majority of the alignment parameters are treated as time-independent. In reality, the positions of high-level structures are more sensitive to the changing environment, and the relative position of modules mounted on top remain more stable with time.

An interval of validity (IOV) is a period during which the detector environment remains stable, and we don't expect much change in the high-level structure. It is sometimes determined by running preliminary alignments with tracks from each run, and compare their alignment parameters and validation results. All the tracks from a specific IOV are combined to determine the geometry of high-level structure for that IOV.

In the local approach, the multi-IOV alignment is done in two steps. In the first step, the high-level structure is aligned for each IOV, using only tracks from the corresponding IOV. The final aligned geometries for all IOVs are combined into a multi-IOV geometry, and is used as the starting geometry for the second step. In the second step, tracks from all IOVs are used together to determine the position of each module w.r.t. the high-level structure. Each track pick the starting geometry according to its own IOV, but the relative correction is calculated using all tracks.

This method allows to use the full statistics of the whole dataset while still taking into account the time dependence of higher structures.

3.3.9 Weak Modes

The main challenges of the alignment are the combinations of changes in geometry parameters that leave the objective function χ^2 invariant. This will be reflected in singularity of the matrix \mathbf{S} in Equation 3.16. These combinations, or geometry transformations, are called “weak modes”, because their contribution to the final

geometry can not be easily determined.

Weak mode arises when coherent change in the geometry parameters \mathbf{p} can be compensated by change of the track parameters. This is especially the case when the starting geometry is far from the true geometry, because the track parameters are determined prior to the alignment. Simple examples include that, the overall shift of the tracker can be compensated by the change of impact parameter of tracks, and the “layer rotation” of the tracker can be compensated by the change of curvature of the tracks. The weak modes will further lead to the bias in track parameters when the aligned geometry is used for track reconstruction, and this contribute significantly to the uncertainty in kinematic properties of the tracks.

Various forms of weak modes are shown in Figure 3.10.

The weak modes depend on a few factors, such as the geometry and segmentation of the detector, the geometrical distribution of tracks, and the alignment parameters to solve. A few typical weak modes and their solutions are discussed below.

3.3.9.1 Z-Expansion

Z-expansion ($\Delta z \propto z$) is the most common weak mode, and it happens when the alignment is done with collision tracks parallel to the beam line, and the z-movement of tracker modules will have small effect on the track-hit residuals. The most effective way to constrain this weak mode is to include cosmic tracks, with track parameters more sensitive to the z-movement of the detector. When there are limited number of

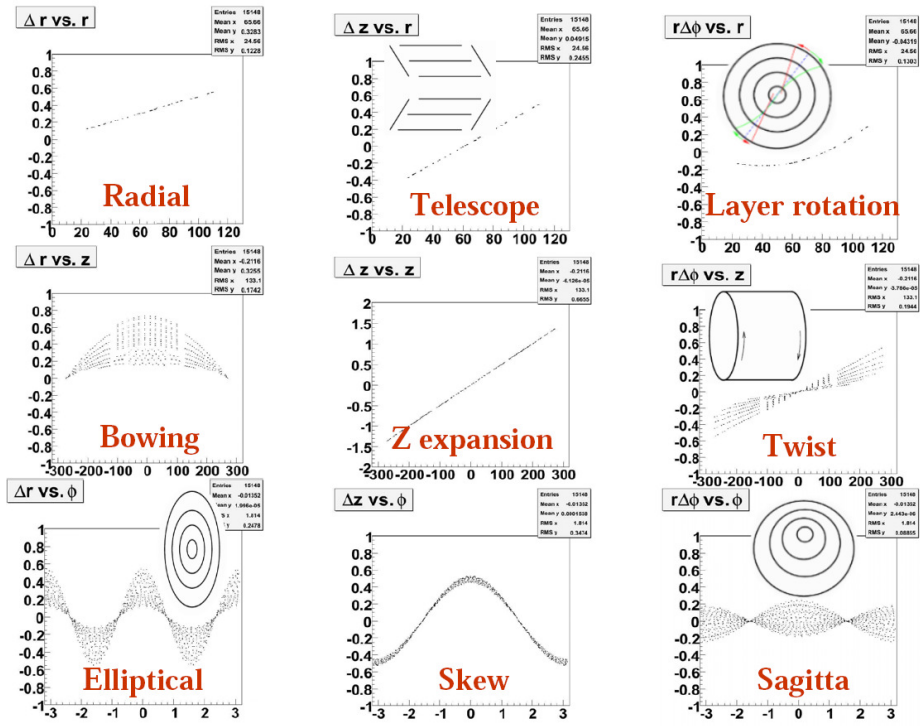


Figure 3.10: Possible weak modes in CMS tracker alignment.

the cosmic tracks, more weight need to be assigned to the cosmic tracks compared with the collision tracks for a better constraint.

Z-expansion does not change the transverse momenta of the reconstructed tracks. There are a few other weak modes that systematically affect the track transverse momenta. They can be categorized as charge-symmetric and charge-asymmetric deformations, depending on if the change to the transverse momenta is the same or the opposite for the oppositely charged tracks.

3.3.9.2 charge-symmetric deformations

The systematic changes in radial direction will change the momentum of positive and negative charged tracks in the same way, so we call them charge-symmetric deformations. The examples are:

Simple radial expansion/contraction ($\Delta r \propto r$): constant Δp_T , no spatial dependence. Elliptical ($\Delta r \propto \cos(2\phi + \phi_0)$): Δp_T has the same ϕ dependence. Sagitta ($\Delta r \propto \cos(\phi + \phi_0)$): Δp_T has the same ϕ dependence. Bowing ($\Delta r \propto z$): Δp_T has the same z dependence

Figure 3.11(a) shows the changes in reconstructed track curvature caused by sagitta deformation.

3.3.9.3 charge-asymmetric deformations

The systematic changes in ϕ direction will change the momentum of positive and negative charged tracks in opposite ways, so we call them charge-asymmetric deformations. The examples are:

Simple layer rotation ($\Delta\phi \propto r$) : constant Δp_T , no spatial dependence. Layer rotation with ϕ dependence ($\Delta\phi \propto r f(\phi)$) : Δp_T has the same phi dependence Twist ($\Delta\phi \propto z$): Δp_T has the same z dependence

Figures 3.11(b) and (c) show the changes on reconstructed track curvature caused by layer rotation and twist deformation.

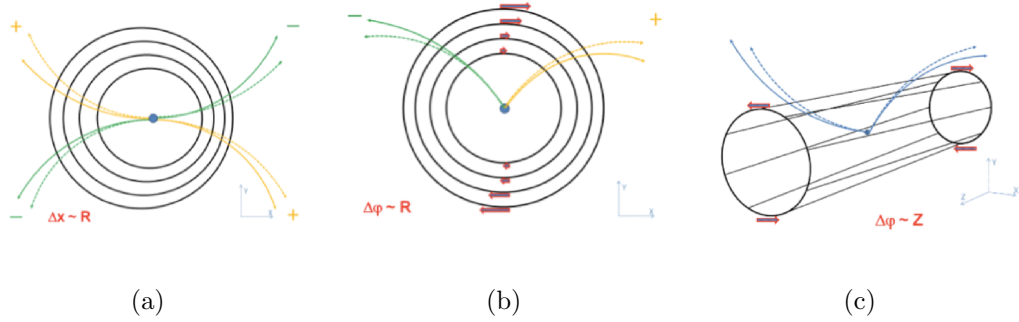


Figure 3.11: The impact of weak modes on track reconstruction. The dashed lines are the true track trajectories, and the solid lines are the reconstructed tracks.

3.3.9.4 $Z\mu\mu$ validation and constraint

The information of a known resonance decaying into two charged particles can be used to detect as well as constrain certain weak modes. A common process used is

the decay of Z boson into two muons, because high p_T muons are measured with high precision and efficiency by CMS.

In $Z\mu\mu$ validation, the reconstructed Z mass is compared with the theoretical Z mass, and plotted against the track ϕ and η for both μ^+ and μ^- . Since the two muons have opposite charge, it can detect both charge-symmetric and charge-asymmetric weak modes. The ϕ and η dependence of the bias in reconstructed Z mass can also point to the types of existing weak modes.

A detailed dependence is mentioned in sections 3.3.9.2 and 3.3.9.3 and plotted in the simulation study in Figure 3.12

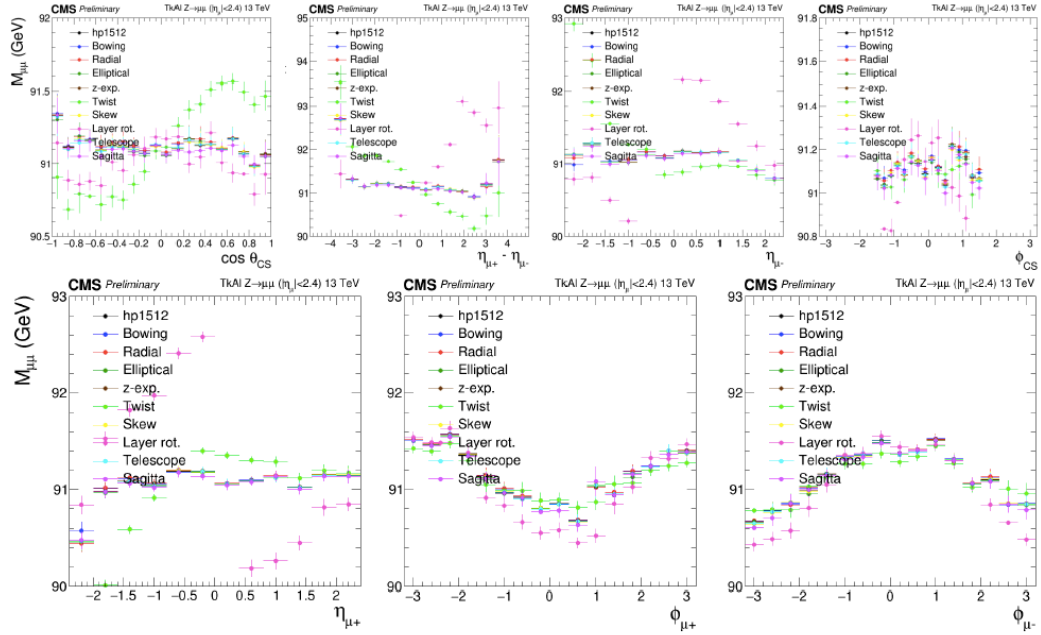


Figure 3.12: Possible weak modes in CMS tracker alignment.

The $Z\mu\mu$ constraint uses the Z mass and decay vertex as a constraint in alignment

fit. It is an effective method to constrain the weak modes that can be detected by $Z\mu\mu$ validation.

3.3.10 Validation Methods

To estimate the statistical accuracy of the alignment results and to detect possible biases, many validation methods are used. In addition to $Z\mu\mu$ validation mentioned in 3.3.9.4, the track splitting, distribution of median of residuals, primary vertex are commonly used.

3.3.10.1 Track Splitting

In track splitting validation, cosmic tracks are split in half at the point of closest approach to beam line, then both halves are reconstructed independently and their parameters are compared at the splitting point. The normalized differences between track parameters of the two halves are histogrammed. If the relative position of the detector sub-structures used to reconstruct the two half-tracks are not determined correctly, the difference in the track parameters will have systematic deviation from zero. The width of the distribution measures the achieved alignment precision.

Figure. 3.13 shows an example of track splitting validation results.

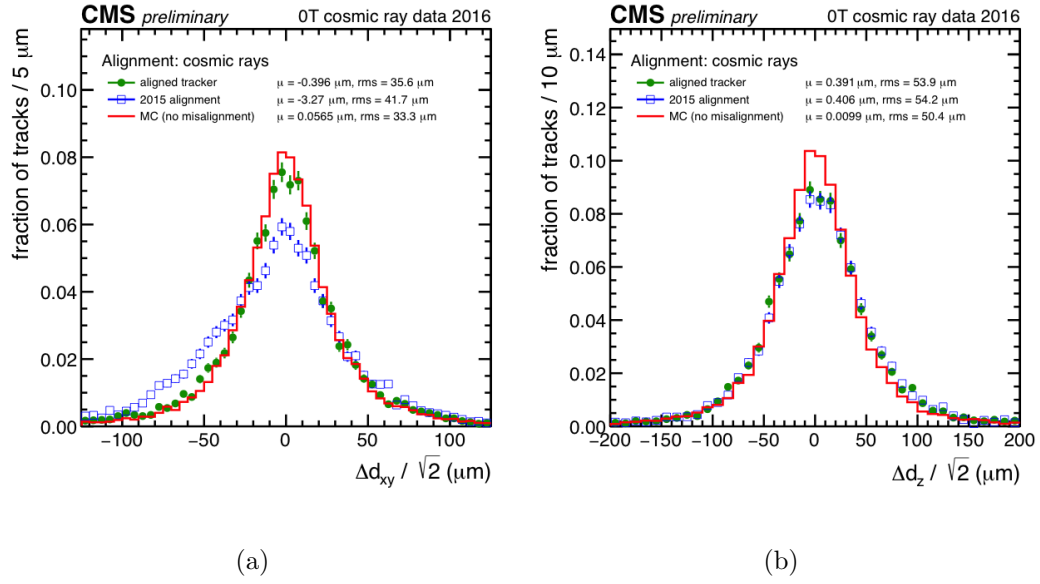


Figure 3.13: The track splitting validation in impact parameters d_{xy} and d_z for 2016 CRUZET alignment. The observed precision using the aligned geometry (green circles), produced with the Millepede-II and HipPy algorithms using cosmic ray data at 0T, is a major improvement over the 2015 EOY (End-of-Year) geometry (blue empty squares). The precision comes close to that of the ideal Monte Carlo (red).

3.3.10.2 Distribution of the Median of Residuals

Each track is refitted using the alignment constants under consideration, and the hit prediction for each module is obtained from all of the other track hits. The median of the distribution of unbiased hit residuals (DMR) is then taken for each module and is histogrammed.

The width of this distribution of the medians of residuals is a measure of the statistical precision of alignment results; deviations from zero indicate possible biases. The width also has an intrinsic component due to the limited number of tracks, meaning that distributions can only be compared if they are produced with the same number of tracks, as is the case within each set of plots here.

Figure. 3.14 shows an example the DMR validation results.

3.3.10.3 Primary Vertex

The resolution of the reconstructed vertex position is driven by the pixel detector since it is the closest detector to the interaction point and has the best hit resolution. The primary vertex residual method is based on the study the distance between the track and the vertex, the latter reconstructed without the track under scrutiny (unbiased track-vertex residual).

Events used in this analysis are selected online with minimum bias triggers. The fit of the vertex must have at least 4 degrees of freedom. For each of the vertices, the impact parameters are measured for tracks with more than 6 hits in the tracker,

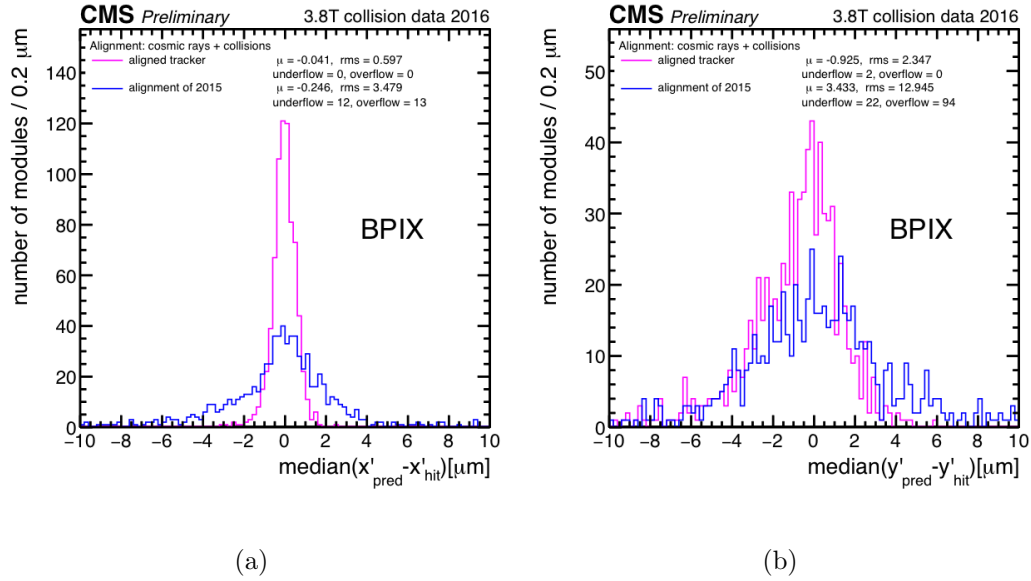


Figure 3.14: The DMR validations for the local x- and y-directions in the barrel pixel detector. The alignment shown in magenta was produced with the Millepede-II and HipPy algorithms using 3.8 T cosmic ray and collision data collected in 2016. The blue line shows the starting geometry obtained at the end of 2015.

of which at least two are in the pixel detector, and at least one hit in the first layer of the Barrel Pixel or the first disk of the Forward Pixel, with χ^2/ndof of the track fit < 5 . The vertex position is recalculated excluding the track under scrutiny. A deterministic annealing clustering algorithm is used in order to make the method robust against pileup, as in the default reconstruction sequence.

The distributions of the unbiased track-vertex residuals in the transverse plane, and in the longitudinal direction, are studied in bins of track azimuth ϕ and pseudo-rapidity η . Random misalignments of the modules affect only the resolution of the unbiased track-vertex residual, increasing the width of the distributions, but without biasing their mean. Systematic movements of the modules will bias the distributions in a way that depends on the nature and size of the misalignment and the selected tracks.

Figure. 3.13 shows an example the primary vertex validation results in 2016.

3.3.11 Conclusion

The track-based alignment is an effective method to align CMS tracker to a high precision close to the intrinsic silicon sensor resolution. The major computational challenge is the inversion of large matrices, due to large number of tracker geometry parameters and track parameters. In order to reduce the size of this problem, the matrix is partitioned and the alignment parameters are solved after track fitting. There are two approaches adopted by CMS alignment group. The local approach

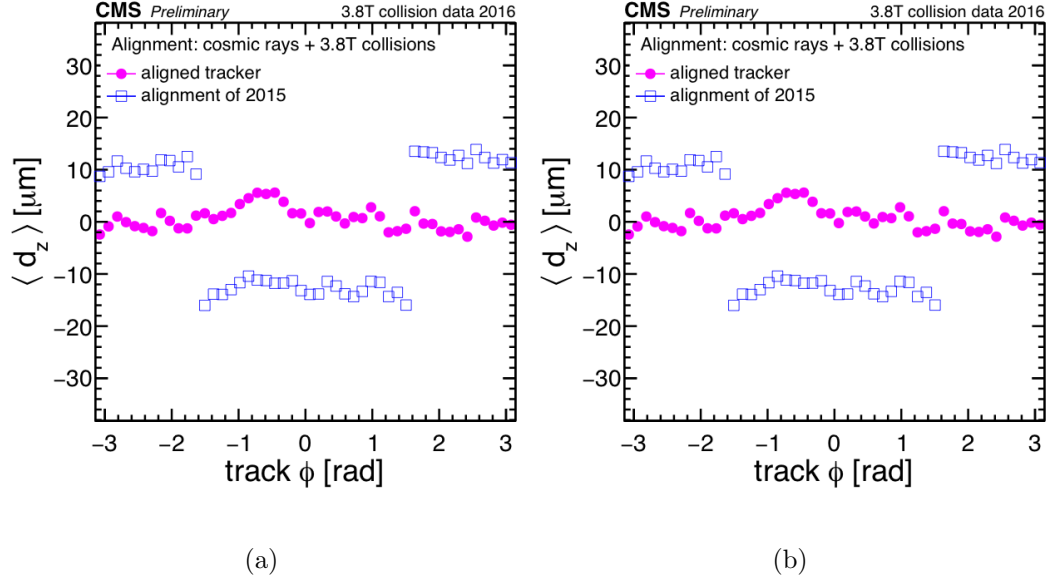


Figure 3.15: The primary vertex validation, with d_{xy} and d_z plotted in bins of track azimuth ϕ . The performance of a dedicated alignment (magenta) achieved with the Millepede-II and HipPy algorithms using cosmic ray and collision data at 3.8T is compared to the one of the alignments used to reprocess the collision data collected by CMS during 2015 (blue).

solves for each detector unit independently and reduce the matrix size to 6×6 . The correlation between geometry parameters are taken into account by running multiple iterations. The global approach solves the large sparse matrix in one go, and includes the correlation terms in calculation. The two approaches had shown similar performance, and the best aligned geometry is usually obtained by combining the two sequentially. Minimizing the objective χ^2 function cannot guarantee the aligned geometry to be correct, due to possible weak modes. Different forms of weak modes have been discussed as well as the ways to detect and constrain them. Various validation methods are used to test the final alignment results, and to estimate the alignment precision. The sample validation plots from alignments are shown.

Chapter 4

Data Analysis Methods

4.1 Trigger and Data Acquisition

At design luminosity, the bunch crossing rate is 40 MHz, leading to 10^9 pp interactions per second. Data recorded from each pp interaction (event) has a size of about 1.5 MB. Data from only 100 crossings can be stored per second. Therefore, a trigger system is needed to keep only the most interesting events, with an acceptance rate of $1/10^6$. The CMS data acquisition and trigger systems consist of four parts: the detector electronics, the Level-1 trigger, the readout network, and the online high-level trigger.

4.1.1 Level-1 Triggers

Level-1 triggers are made of hardware processors, and the trigger calculation time is less than $1\ \mu\text{s}$. Level-1 triggers use the information from calorimeters and muon systems, and the correlation between them. The decision of Level-1 trigger is based on “trigger primitive” objects which pass certain E_T or p_T thresholds. The design output rate of Level-1 trigger is 100 kHz. All high resolution data is held in pipelined memories for subsequent decisions.

4.1.2 High Level Triggers (HLT)

The data passing Level-1 Trigger is then transferred from the pipeline to front-end readout buffers. The HLT processors in a processor farm run the HLT software code to reduce the event rate from 100 kHz to 100 Hz for mass storage. The decision of HLT is based on “partially” reconstructed objects, so that events can be discarded as soon as possible. For examples, the information from calorimeters and muon systems are used first, then followed by the information from inner tracker pixel system, and eventually the full information of the event.

4.2 Software and Computing

There are about 50 Petabytes of data generated by LHC in 2016. The storage and processing power needed to analyze LHC data is far beyond the capability of

CERN’s central computing system. Therefore, a highly distributed global computing infrastructure, Worldwide LHC Computing Grid (WLCG), is used to store, distribute and analyze the data from LHC. WLCG is supported by 170 computing centers in 42 countries, making it the world’s largest computing grid. WLCG is made up of four layers, or “tiers”. CERN holds a Tier-0 computing center, which is primarily responsible for storing raw data and distributing the data to Tier-1. Tier-1 consists of thirteen large computing centers at national labs and universities worldwide. They are responsible to keep a fraction of raw data and reconstructed data, large-scale reprocessing, and distribute the data to Tier-2. Tier-2 consists of 160 universities and other scientific institutes. They provide additional computing power for specific analysis and simulation. Tier-3 consists of local clusters or even individual PC, with no formal engagement to WLCG.

4.3 Reconstruction of Physical Objects

There are three steps for event reconstruction in CMS. Local reconstruction is the reconstruction of hits on individual detector modules, providing the information of position and energy deposition of the particles traveling through the detector modules. Global reconstruction combines the local reconstruction information from all individual modules in the same subdetector, and reconstruct objects based on all measurements from that subdetector. Eventually a combined reconstruction is per-

formed to combine the input objects from different subdetectors, and to reconstruct objects based on measurements from complete CMS detector.

A complete description of the particles emerging from each collision is obtained via the CMS particle flow (PF) algorithm,^{1,14} which reconstructs and identifies each individual particle with an optimized combination of information from the various elements of the CMS detector. PF particle candidates are classified as charged hadrons, neutral hadrons, photons, muons, or electrons, and they are then used to build higher-level objects.

4.3.1 Leptons

4.3.1.1 Electrons

Electron and photon showers deposit their energy in ECAL crystals. The energy deposit has a spread in ϕ due to strong magnetic field. “superclusters” are built by adding up clusters in the corresponding ϕ window. Electrons are reconstructed by matching ECAL superclusters with tracks in the inner tracker, within the geometrical acceptance defined by $|\eta^e| < 2.5$ and for transverse momentum $p_T^e > 7$ GeV. Electron candidates are seeded either from clusters of energy deposits in the ECAL (e/ γ superclusters), matched to hits in the inner tracker (“outside-in”), or from hits in the inner tracker, matched to ECAL clusters (“inside-out”).

Electrons are identified using a multivariate discriminant which exploits observ-

ables sensitive to the presence of bremsstrahlung along the electron trajectory, the geometrical and momentum-energy matching between the electron trajectory and the associated energy cluster in the ECAL, the shape of the electromagnetic shower in the ECAL, and variables that discriminate against electrons originating from photon conversions. The training and optimization of the multivariate discriminant used for electron identification are performed using simulation and are divided into six regions formed from two transverse momentum ranges (7–10 GeV and >10 GeV) and three pseudorapidity regions: central barrel ($|\eta^e| < 0.8$), outer barrel ($0.8 < |\eta^e| < 1.479$), and endcaps ($1.479 < |\eta^e| < 2.5$).

4.3.1.2 Muons

The matching between the inner and outer tracks proceeds either outside-in, starting from a track in the muon system, or inside-out, starting from a track in the silicon tracker. Tracker tracks that match track segments in only one or two stations of the muon system are also considered to collect very low- p_T muons that may not have sufficient energy to penetrate the entire muon system. The muons are selected among the reconstructed muon track candidates by applying minimal requirements on the track in both the muon system and inner tracker system, and taking into account compatibility with small energy deposits in the calorimeters.

Muons within the geometrical acceptance $|\eta^\mu| < 2.4$ and $p_T^\mu > 5\text{GeV}$ are reconstructed in the inner tracker and in the outer muon system. Muon reconstruction

then combines the information from these two subsystems in one of two ways:

- *Global Muons* are formed by finding tracks reconstructed in the muon system (called *Standalone Muons*) and propagating them inward to the tracker. If a matching tracker track is found, a Global Muon is built merging the two track sections into one trajectory that combines the information from hits in the tracker and hits in the muon detectors.
- *Tracker Muons* are built by propagating tracker tracks outward to the muon system and looking for reconstructed segments compatible with the extrapolated tracks, to collect very low- p_T muons that may not have sufficient energy to penetrate the entire muon system.

An additional “ghost-cleaning” step is performed to deal with situations when a single muon can be incorrectly reconstructed as two or more muons:

- Tracker Muons that are not Global Muons are required to be arbitrated.
- If two muons are sharing 50% or more of their segments then the muon with lower quality is removed.

Muon efficiencies are measured with the Tag and Probe method performed on $Z \rightarrow \mu\mu$ and $J/\Psi \rightarrow \mu\mu$ events in bins of p_T and η . Data-to-MC scale factors are derived by comparing the efficiencies measured in data and MC and used to correct MC events.

4.3.1.3 Lepton isolation and SIP

In order to suppress muons originating from in-flight decays of hadrons and electrons from photon conversions, we require each lepton track to have a 3D impact parameter significance (SIP) with respect to the primary vertex to be less than 4. The primary vertex is defined as the one with the highest sum of p_T^2 of clusters of associated tracks.

To discriminate prompt leptons from Z boson decay from those arising from electroweak decays of hadrons within jets, an isolation requirement for leptons is imposed. The isolation is computed by summing over the transverse momenta and energies of the charged and neutral particles within a cone of opening angle $\Delta R = \sqrt{(\eta^l - \eta^i)^2 + (\phi^l - \phi^i)^2}$ around the electron's direction at the interaction vertex.

Since isolation is sensitive to energy deposits from pileup interactions, it has to be corrected to make it pileup-independent.

For electrons, the mean pile-up contribution to the isolation cone is obtained as:

$$PU = \rho \times A_{\text{eff}} \quad (4.1)$$

where ρ is the mean energy density in the event and the effective area A_{eff} is defined as the ratio between the slope of the average isolation and that of ρ as a function of the number of vertices.

The relative isolation for an electron is defined as:

$$\text{RelPFiso} = \left(\sum_{\text{charged}} p_T + \max\left(\sum_{\text{neutral}} p_T - \rho \times A_{\text{eff}}, 0 \text{ GeV} \right) \right) / p_T^{\text{lepton}} \quad (4.2)$$

For the muons, $\Delta\beta$ correction is applied, whereby $\Delta\beta$ gives an estimate of the energy deposit of neutral particles (hadrons and photons) from pile-up vertices. The relative isolation for muons is then defined as:

$$\text{RelPFiso} = (\sum_{\text{charged}} p_T + \max(\sum_{\text{neutral}} p_T + \sum_{\text{photon}} p_T - \Delta\beta, 0 \text{ GeV}))/p_T^{\text{lepton}} \quad (4.3)$$

The isolation working point for Run1 analysis was $\text{RelPFiso}(\Delta R = 0.4) < 0.4$, and for Run2 is $\text{RelPFiso}(\Delta R = 0.3) < 0.35$.

4.3.1.4 FSR Photons

When an ECAL “supercluster” has no matching track in the inner tracker, the object candidate is flagged as photon. The selection of photon uses isolation cuts based on shower shape. In the 4ℓ final state, an algorithm is used to recover the final-state radiation (FSR) from leptons. Photons reconstructed by the PF algorithm within $|\eta_\gamma| < 2.4$ are considered as FSR candidates if they pass $p_T^\gamma > 2\text{GeV}$ and $\mathcal{I}^\ell < 1.8$. Associating every such photon to the closest selected lepton in the event, we discard photons that do not satisfy $\Delta R(\gamma, \ell)/(p_T^\gamma)^2 < 0.012$ and $\Delta R(\gamma, \ell) < 0.5$. We finally retain the lowest- $\Delta R(\gamma, \ell)/(p_T^\gamma)^2$ photon candidate of every lepton, if any. The photons identified as FSR are excluded from any isolation computation.

4.3.2 Jets

Jets are reconstructed using a clustering technique in HCAL. A seed calorimetric towers is selected based on its high E_T . Objects close in (η, ϕ) to the seed tower is combined to form a proto-jet. The process continues until no seeding tower remains and the proto-jet parameters are stabilized. The anti- k_T clustering algorithm, with a distance parameter $R = 0.4$ (AK4 jets) and $R = 0.8$ (AK8 jets), after rejecting the charged hadrons that are associated to a pileup primary vertex. Jet Energy Corrections are used to correct the jet energy measurement, for the dependency of jet response on jet η and p_T . In addition, the jets are cleaned from any of the tight leptons (passing the SIP and isolation cut computed after FSR correction) and FSR photons by a separation criterion: $\Delta R(\text{jet}, \text{lepton}/\text{photon}) > 0.4(0.8)$.

4.4 Event Selection

4.4.1 $H \rightarrow ZZ \rightarrow 4\ell$

The event selection is designed to extract signal candidates from events containing at least four well-identified and isolated leptons, each originating from the primary vertex and possibly accompanied by an FSR photon candidate, as described in Section 4.3. In what follows, unless otherwise stated, FSR photons are included in invariant mass computations.

First, Z candidates are formed with pairs of leptons of the same flavor and opposite-charge (e^+e^- , $\mu^+\mu^-$) and required to pass $12 < m_{\ell^+\ell^-} < 120$ GeV. They are then combined into ZZ candidates, wherein we denote as Z_1 the Z candidate with an invariant mass closest to the nominal Z boson mass, and as Z_2 the other one. The flavors of involved leptons define three mutually exclusive subchannels: $4e$, 4μ and $2e2\mu$.

To be considered for the analysis, ZZ candidates have to pass a set of kinematic requirements that improve the sensitivity to Higgs boson decays. The Z_1 invariant mass must be larger than 40 GeV. All leptons must be separated in angular space by at least $\Delta R(\ell_i, \ell_j) > 0.02$. At least two leptons are required to have $p_T > 10$ GeV and at least one is required to have $p_T > 20$ GeV. In the 4μ and $4e$ subchannels, where an alternative $Z_a Z_b$ candidate can be built out of the same four leptons, we discard candidates with $m_{Z_b} < 12$ GeV if Z_a is closer to the nominal Z boson mass than Z_1 is. This protects against events that contain an on-shell Z and a low-mass dilepton resonance. To further suppress events with leptons originating from hadron decays in jet fragmentation or from the decay of low-mass hadronic resonances, all four opposite-charge lepton pairs that can be built with the four leptons (irrespective of flavor) are required to satisfy $m_{\ell^+\ell'^-} > 4$ GeV, where selected. FSR photons are disregarded in the invariant mass computation. Finally, the four-lepton invariant mass $m_{4\ell}$ must be larger than 70 GeV, which defines the mass range of interest for the subsequent steps of the analysis.

In events where more than one ZZ candidate passes the above selection, the candidate with the highest value of $\mathcal{D}_{\text{bkg}}^{\text{kin}}$ (defined in Section 2.3.4) is retained, except if two candidates consist of the same four leptons in which case the candidate with the Z_1 mass closest to the nominal Z boson mass is retained.

4.4.2 $H \rightarrow ZZ \rightarrow 2\ell 2q$

In the $X \rightarrow ZZ \rightarrow 2\ell 2q$ analysis, events are selected with a combination of leptonic and hadronic Z candidates.

The lepton pair selection is similar to the four-lepton analysis: pairs of opposite sign and same flavour electrons and muons with invariant mass between 60 and 120 GeV. The leading and subleading leptons must have minimal p_T of 40 and 24 GeV, and a minimum dilepton p_T of 100 GeV is also required to reject low-HT Drell-Yan. The two leptons must have a minimum separation of $\Delta R > 0.02$ to remove ghost tracks.

The hadronic Z boson candidates have two types: the resolved and the merged. In the resolved case, the two quarks from Z decay forms two distinguishable AK4 jets. In the merged case, Z is highly boosted and a single AK8 jet is taken as a hadronic Z boson candidate. The reconstructed hadronic Z boson is required to have an invariant mass between 40 and 180 GeV, and p_T larger than 100(170) GeV in the resolved (merged) case. Jets must not overlap with leptons, so a cut $\Delta R(\ell, jet) > 0.4$ is applied to each of them.

In order to minimise contamination from standard model DY + jets production, we further require that the hadronic Z boson candidate from a merged selection has substructure consistent with hadronic Z decay. We exploit the techniques that are already standard in searches with merged jets coming from boosted bosons.¹¹ The N-subjettiness, τ_N is defined as

$$\tau_N = \frac{1}{d_0} \sum_k p_{T,k} \min(\Delta R_{1,k}, \Delta R_{2,k}, \dots, \Delta R_{N,k}) \quad (4.4)$$

where the index k runs over the jet constituents and the distances $\Delta R_{N,k}$ are calculated with respect to the axis of the n^{th} subjet. The normalisation factor d_0 is calculated as $d_0 = \sum_k p_{T,k} R_0$, setting R_0 to the jet radius of the original jet. Jets with smaller τ_N are more compatible with the N -subjets configuration. We use the ratio of 2-subjettiness over 1-subjettiness, $\tau_{21} = \tau_2/\tau_1$, as the discriminating variable for the jet substructure, and impose a $\tau_{21} < 0.6$ requirement on merged hadronic Z candidates.

Many events have candidates passing both selections above or they have multiple candidates in one category. An arbitration procedure is used to rank multiple hadronic Z boson candidates reconstructed in a single event:

- If two or more candidates are found in the resolved (merged) jet category, we take the one with the largest $p_T(jj)$ ($p_T(J)$);
- If there is one in merged and one in resolved jet category, we define a “good

merging region” by the selections $p_T(\ell\ell) > 200 \text{ GeV}$, $p_T(J) > 300 \text{ GeV}$ and $\tau_{21}(J) < 0.6$. If we have a merged jet + accompanying dilepton candidate with these requirements, the merged jet is preferred *regardless* of its pruned mass being in signal or sideband region. Otherwise resolved jets are chosen.

In order to improve the ZZ invariant mass resolution in the resolved-jet case, a kinematic fit is performed using a mass constraint on the intermediate $Z \rightarrow q\bar{q}$. The kinematics of final state particles (here the p_T of the two jets forming the Z boson) is re-evaluated with a constraint on the reconstructed Z mass to follow the Z boson’s true lineshape. For each event, the likelihood is maximised and p_T information of the refitted jets are updated. After this refitting, the mass of the Z candidate and m_{ZZ} are recalculated.

The hadronic and leptonic Z boson candidates are combined to form a resonance candidate. The reconstructed ZZ candidate mass, m_{ZZ} denotes the dilepton + dijet mass $M_{\ell\ell jj}$ after kinematic fitting in the resolved case, and to the dilepton + merged jet invariant mass $M_{\ell\ell J}$ in the merged case. A requirement of $m_{ZZ} > 300 \text{ GeV}$ is imposed.

Events that pass the above selection and additionally have hadronic Z mass in the range $[70, 105] \text{ GeV}$ form the *signal region* that is expected to be enriched in new physics process events. On the other hand, events in the range $[40, 70] \text{ GeV} \cup [135, 180] \text{ GeV}$ are retained for background estimation and form the *sideband region*.

4.5 Monte Carlo Simulation

Monte Carlo (MC) simulation samples for the signals and the relevant background processes are used to estimate backgrounds, optimize the event selection, and evaluate the acceptance and systematic uncertainties.

Two type of generators are used on CMS. The general-purpose generators, such as PYTHIA⁸³¹ and HERWIG, provide a description of what happens end-to-end in a hadron collision. They contain theory models for a number of physics aspects, such as hard and soft interactions, parton distributions, initial and final state parton showers, multiple interactions, fragmentation and decay. The Matrix Element (ME) calculators, such as POWHEG 2.0,^{6,19,29} MADGRAPH5-AMCATNLO, and JHUGEN 7.0.2^{5,10,20} deliver an event at the parton level, and one or another multi-purpose generator can further be used to develop a fully hadronized event.

The SM Higgs and Higgs-like signal events are generated at NLO in QCD with the POWHEG 2.0 in gluon fusion and vector-boson fusion, and the decays are modeled with JHUGEN 7.0.2, including additional corrections for the ZZ branching fraction.

Signals with spin-1 and spin-2 hypotheses are generated using the JHUGEN 7.0.2 generator at LO. JHUGEN is able to model correctly the kinematic distributions of outgoing particles, given a set of effective coefficients describing production and decay.

The gluon-fusion production of $gg \rightarrow ZZ/Z\gamma^* \rightarrow 4f$ background, including the off-shell tail of the $H(125)$ boson, is modeled at LO in QCD with MCFM 7.0.¹² The

corresponding electroweak production of $\bar{q}q'ZZ/Z\gamma^* \rightarrow 4f\bar{q}q'$ background is modeled at LO in QCD with PHANTOM.

The $q\bar{q} \rightarrow ZZ/Z\gamma^* \rightarrow 4f$ background is evaluated from POWHEG and MADGRAPH5-AMCATNLO MC simulation. The Z+jets ($Z \rightarrow \ell^+\ell^-$) simulation is a composite sample comprising a set of exclusive LO samples with different associated parton multiplicities, and a dedicated LO production with associated b-quark production, all produced with MADGRAPH and corrected to NLO QCD accuracy with a K-factor depending on the p_T of the dilepton pair, derived from a merged MADGRAPH5-AMCATNLO simulation. The $t\bar{t}$ simulation is performed with POWHEG at NLO QCD.

All signal and background generators are interfaced with PYTHIA8 to simulate the multi-parton interaction and hadronization effects. The generated events are processed through a detailed simulation of the CMS detector based on GEANT4^{3,4} and are reconstructed with the same algorithms that are used for data. The simulated events include overlapping pp interactions (pileup) and have been reweighted so that the distribution of the number of interactions per LHC bunch crossing in simulation matches that observed in data.

4.6 Statistical Analysis

4.6.1 Test of Hypotheses

The search for a new particle can be formulated as a hypothesis testing, where the null hypothesis H_0 is the background-only model, and the alternative hypothesis H_1 is the signal-plus-background model. The target is to use a measurement to reject (discovery) or accept (exclusion) H_0 .

In addition to particle search, sometimes we also need to test if the data are consistent with one theoretical model or the other. For example, in chapter 5, we test standard model Higgs boson against exotic spin resonance models.

In hypothesis testing, the space of observables x is separated into critical region w , where H_0 is rejected, and region of acceptance w^c , where H_0 is accepted. The significance level α is the probability of x falling into critical region when H_0 is true (rate of type I error). The power of the test, $1-\beta$, is the probability of x falling into the critical region when H_1 is true, where β is the probability of x falling into acceptance region when H_1 is true (rate of type II error).

According to Neyman-Pearson Lemma, the likelihood-ratio test has the maximum power $1-\beta$, for a given significance level α :

$$\alpha = \int_w \mathcal{L}(x|\theta_0) dx \tag{4.5}$$

$$1 - \beta = \int_w \mathcal{L}(x|\theta_1)dx = \int_w \frac{\mathcal{L}(x|\theta_1)}{\mathcal{L}(x|\theta_0)} f(x|\theta_0)dx = E_w\left(\frac{\mathcal{L}(x|\theta_1)}{\mathcal{L}(x|\theta_0)} \middle| \theta = \theta_0\right) \quad (4.6)$$

To maximize $1 - \beta$, the acceptance region is chosen to contain largest values of $\mathcal{L}(x|\theta_1)/\mathcal{L}(x|\theta_0)$. Therefore a test-statistic $q(x)$ is chosen to be the ratio of the likelihoods of the two hypotheses, and the critical region is $q > q_c$ for some threshold q_c .

The actual quantity used in high energy physics is the negative logarithm of the likelihood ratio, or more precisely:

$$q = -2 \ln \frac{\mathcal{L}(x|\theta_1)}{\mathcal{L}(x|\theta_0)} \quad (4.7)$$

4.6.2 Profile Likelihood Ratio

For signal search, the profile likelihood ratio is used.^{15,17} The parameter of interest is the signal strength $\mu = \sigma/\sigma_{SM}$, where σ is the signal production cross section and σ_{SM} is its SM prediction. $\mu = 0$ corresponds to no signal (H_0), and $\mu = 1$ corresponds to nominal (Standard Model) signal (H_1).

By classical frequentist approach, the test statistic follows from 4.7:

$$q = -2 \ln \frac{\mathcal{L}(x|\mu = 1)}{\mathcal{L}(x|\mu = 0)} \quad (4.8)$$

where the likelihood function is a production of Poisson probabilities given signal and background rates.

This is only valid when uncertainties are not taken into account. Usually the model includes nuisance parameters θ which accounts for uncertainties in the signal or background due to detector effects, theoretical approximations etc. Then the above test statistic is sensitive to the values of nuisance parameters.

To prevent the inference of signal from downward fluctuation in background, the profile likelihood ratio is used:¹⁷

$$q = -2 \ln \frac{\mathcal{L}(x|\mu, \hat{\theta}_\mu)}{\mathcal{L}(x|\hat{\mu}, \hat{\theta})} \quad (4.9)$$

where $\hat{\theta}_\mu$ is the maximum likelihood estimation of θ with μ fixed. $\hat{\mu}$ and $\hat{\theta}$ are the best fit with both μ and θ left floating.

When there are enough events, the test statistic in Eq.4.9 is independent of the nuisance parameters θ . Also, according to Wilks' theorem, the distribution of q in Eq.4.9 converges to χ^2 distribution with one degree of freedom, under certain conditions. Therefore, $q(\mu)$, the test statistic as a function of μ , can be used to determine the uncertainties on the fitted value of μ . For example, the 68% confidence interval for μ is given by $q(\mu) \leq 1$ and the 95% confidence interval is given by $q(\mu) \leq 3.84$.

4.6.3 Exclusion Limits and Significance of Excess

The p-value for a given observation is the probability of equal or more extreme values of q than observed under null hypothesis, this corresponds to the significance

level α when setting $q_c = q_{obs}$.

Discovery is based on the compatibility of data with the background-only hypothesis. In high energy physics, a discovery is made when a $5\text{-}\sigma$ significance is achieved, with $p_b = 2.87 \times 10^{-7}$, so there's very small probability that the background-only model is rejected by chance. When nuisance parameters are considered, the p-value is required to be small for all values of nuisance parameters. This is done by choosing the nuisance parameters that fit best to the background-only model ($\mu = 0$) when calculating p (to make p larger).

Exclusion is based on the compatibility of data with the signal-plus-background hypothesis. At 95% confidence level, the exclusion upper limit (one-sided confidence interval) is calculated by a p-value of 5%. In order to avoid claiming sensitivity to an arbitrarily small signal rate, the modified frequentist method CL_s is usually used. To calculate CL_s upper limit, the new p-value is defined as the ratio of p-values p_s/p_b .

In order to quantify the sensitivity of analysis, the exceptions are calculated before unblinding data. Asimov dataset is used to estimate the median test statistics for this purpose. The expected significance is calculated by assuming the standard model signal rate ($\mu = 1$), while the expected exclusion upper limit is calculated by assuming the background hypothesis ($\mu = 0$).

4.6.4 Test for Alternative Signals

In the analysis introduced in chapter 5, hypothesis testing is used to distinguish an alternative signal hypothesis from the SM Higgs boson. The likelihoods \mathcal{L} is evaluated based on 2D or 3D probability density functions of kinematic discriminants distributions. The test statistic q for each point of parameter space is constructed as:

$$q = -2 \ln \frac{\mathcal{L}_X}{\mathcal{L}_{0^+}} = -2 \ln \prod_i \frac{pdf(D_i | X + \text{bkg})}{pdf(D_i | 0^+ + \text{bkg})}, \quad (4.10)$$

where i runs over all the events in an pseudo-experiment or real data.

The pdf of test statistics for H_0 and H_1 are then constructed by generating toy pseudo-experiments according to the discriminant distributions.

The expected separation power is calculated as the probability of the test statistic distribution for hypothesis X to be higher than the median of test statistic distribution of hypothesis 0^+ , $P(q \geq q_{\text{median}}^{(X)} | 0^+)$. This is equivalent to the power $1 - \beta$ defined above, when setting the threshold q_c to be median test statistic for hypothesis 0^+ .

The consistency of the observed test statistic q_{obs} with respect to the SM Higgs boson hypothesis 0^+ is measured by the probability $P(q \leq q_{\text{obs}} | 0^+)$. This is equivalent to the significance level α when setting $q_c = q_{\text{obs}}$. Similarly, the consistency of the observed test statistic with respect to the alternative hypothesis is measured by the probability $P(q \geq q_{\text{obs}} | X)$. This is equivalent to the power $1 - \beta$ when setting $q_c = q_{\text{obs}}$.

In our analysis, the modified frequentist CL_s is used for calculating exclusion

limits. The CL_s is calculated as the ratio $(1 - \beta)/(1 - \alpha)$:

$$CL_s = \frac{P(q \geq q_{obs}|X)}{P(q \geq q_{obs}|0^+)} \quad (4.11)$$

If $CL_s < \alpha'$ for a small α' , we conclude that the alternative signal model hypothesis is excluded with the confidence level $(1 - \alpha')$.

Chapter 5

Exclusion of the Higgs Boson

Exotic Spin

The observation of a new boson consistent with the standard model (SM) Higgs boson^{18,21–24,26} was reported by ATLAS and CMS Collaborations in 2012.^{2,13} It was followed by a comprehensive set of measurements of the properties of the new boson, with focus on answering if the new boson is the SM Higgs boson and if there are any indications for the physics beyond SM.

Four-lepton final state provides a particularly sensitive channel for the measurement of the coupling structures which determine the spin and CP properties of the boson. Hypothesis testing can be used to evaluate if the data are compatible with the SM Higgs boson (spin-0) or some exotic spin states (spin-1 and spin-2). In this chapter, the tests of mixed spin-one resonances and spin-two resonances will be pre-

sented.

5.1 Experimental data and Simulated Samples

The datasets used were recorded by the CMS experiment corresponding to $\mathcal{L} = 5.1 \text{ fb}^{-1}$ collected in 2011 at 7 TeV and $\mathcal{L} = 19.7 \text{ fb}^{-1}$ collected in 2012 at 8 TeV. Details of Monte Carlo simulation are introduced in Section 4.5. The MC samples are presented in Tables 5.1, 5.2, and 5.3.

Table 5.1: Spin 0 samples at 8 TeV and 7 TeV.

Sample	scenario
Higgs0PMTToZZTo4L_M-125p6_7/8TeV-powheg15-JHUGenV3	0_m^+ SM

Table 5.2: Spin 1 samples at 8 TeV and 7 TeV.

Sample	scenario
Vector1PTToZZTo4L_M-125p6_7/8TeV-JHUGenV3	1^+
Vector1MTToZZTo4L_M-125p6_7/8TeV-JHUGenV3	1^-
Vector1Mf05ph01Pf05ph0ToZZTo4L_M-125p6_7/8TeV-JHUGenV3	$f_{b_1} = 0.5, \text{ phase}=0$
Vector1Mf05ph01Pf05ph90ToZZTo4L_M-125p6_7/8TeV-JHUGenV3	$f_{b_1} = 0.5, \text{ phase}=\pi/2$

Table 5.3: Spin 2 samples at 8 TeV and 7 TeV.

Sample	scenario
gg	
Graviton2BPToZZTo4L_M-125p6.7/8TeV-JHUgenV3	2_b^+
Graviton2HPToZZTo4L_M-125p6.7/8TeV-JHUgenV3	2_h^+
Graviton2MPToZZTo4L_M-125p6.7/8TeV-JHUgenV3	2_h^-
Graviton2PH2ToZZTo4L_M-125p6.7/8TeV-JHUgenV3	$2_{h_2}^+$
Graviton2PH3ToZZTo4L_M-125p6.7/8TeV-JHUgenV3	$2_{h_3}^+$
Graviton2PH6ToZZTo4L_M-125p6.7/8TeV-JHUgenV3	$2_{h_6}^+$
Graviton2PH7ToZZTo4L_M-125p6.7/8TeV-JHUgenV3	$2_{h_7}^+$
Graviton2MH9ToZZTo4L_M-125p6.7/8TeV-JHUgenV3	$2_{h_9}^-$
Graviton2MH10ToZZTo4L_M-125p6.7/8TeV-JHUgenV3	$2_{h_{10}}^-$
q \bar{q}	
Graviton2BPqqbarToZZTo4L_M-125p6.7/8TeV-JHUgenV3	2_b^+
Graviton2HPqqbarToZZTo4L_M-125p6.7/8TeV-JHUgenV3	2_h^+
Graviton2MPqqbarToZZTo4L_M-125p6.7/8TeV-JHUgenV3	2_h^-
Graviton2PH2qqbarToZZTo4L_M-125p6.7/8TeV-JHUgenV3	$2_{h_2}^+$
Graviton2PH3qqbarToZZTo4L_M-125p6.7/8TeV-JHUgenV3	$2_{h_3}^+$
Graviton2PH6qqbarToZZTo4L_M-125p6.7/8TeV-JHUgenV3	$2_{h_6}^+$
Graviton2PH7qqbarToZZTo4L_M-125p6.7/8TeV-JHUgenV3	$2_{h_7}^+$
Graviton2MH9qqbarToZZTo4L_M-125p6.7/8TeV-JHUgenV3	$2_{h_9}^-$
Graviton2MH10qqbarToZZTo4L_M-125p6.7/8TeV-JHUgenV3	$2_{h_{10}}^-$

5.2 Event selection and backgrounds

Leptons and jets are reconstructed as described in Section 4.3. The event selection follow the procedure described in Section 4.4. Additionally, the four-lepton invariant mass $m_{4\ell}$ is restricted to a narrow window around the observed 125.6 GeV resonance ($105.6 < m_{4\ell} < 140.6 \text{ GeV}$).

After the selection, the irreducible backgrounds originate from the gg or $q\bar{q} \rightarrow ZZ / Z\gamma^* \rightarrow 4\ell$ processes. These dominant backgrounds are evaluated from simulation.

The main reducible backgrounds arise from processes in which heavy-flavor jets

produce secondary leptons, and also from processes in which decays of heavy-flavor hadrons, in-flight decays of light mesons within jets, or (for electrons) the decay of charged hadrons overlapping with π^0 decays are misidentified as leptons. The main processes producing these backgrounds are $Z + \text{jets}$, $t\bar{t} + \text{jets}$, $Z\gamma + \text{jets}$, $WW + \text{jets}$, and $WZ + \text{jets}$. We denote these reducible backgrounds as “Z+X” since they are dominated by the $Z + \text{jets}$ process.

The contribution from the reducible background is estimated using two independent data driven methods with dedicated control regions. The control regions are defined by a dilepton pair satisfying all the requirements of a Z_1 candidate and two additional leptons, opposite sign (OS) or same sign (SS), satisfying certain relaxed identification requirements when compared to those used in the analysis. These four leptons are then required to pass the analysis ZZ candidate selection. The event yield in the signal region is obtained by weighting the control region events by the lepton misidentification probability (or fake rate) f , defined as the fraction of non-signal leptons which are identified by the analysis selection criteria.

The lepton fake rates f_e and f_μ are measured by forming a sample which includes a Z_1 candidate consisting of a pair of leptons, both passing the selection requirements used in the analysis, and exactly one additional lepton passing the relaxed selection.

The predicted yield in the signal region of the reducible background is the result of a combination of the two methods. The shape of the $m_{4\ell}$ distribution for the reducible background is obtained by combining the prediction from the OS and SS methods

and fitting the distributions with empirical functional forms built from Landau²⁷ and exponential distributions.

5.3 Yields

The number of estimated background and signal events and the number of observed candidates after final inclusive selection in data in the narrow mass region around 125.6 GeV, are given in Table 5.4, separately for 2011 (7 TeV) and 2012 (8 TeV) and all combined.

Table 5.4: The number of estimated background and signal events, and number of observed candidates, after final inclusive selection.

Channel	$4e$	4μ	$2e2\mu$
5.1 fb ⁻¹ @ 7 TeV			
$\bar{q}q \rightarrow ZZ$	0.84 ± 0.10	1.80 ± 0.11	2.24 ± 0.28
$Z + X$	0.62 ± 0.14	0.22 ± 0.09	1.06 ± 0.29
$gg \rightarrow ZZ$	0.03 ± 0.01	0.06 ± 0.02	0.07 ± 0.02
All background expected	1.49 ± 0.17	2.08 ± 0.14	3.37 ± 0.40
$m_H = 125.6$ GeV	0.70 ± 0.11	1.24 ± 0.14	1.67 ± 0.26
Observed	1	3	6
19.7 fb ⁻¹ @ 8 TeV			
$\bar{q}q \rightarrow ZZ$	2.94 ± 0.33	7.65 ± 0.49	8.86 ± 0.68
$Z + X$	2.77 ± 0.62	1.19 ± 0.48	4.29 ± 1.10
$gg \rightarrow ZZ$	0.20 ± 0.05	0.41 ± 0.10	0.50 ± 0.13
All background expected	5.91 ± 0.71	9.25 ± 0.69	13.65 ± 1.30
$m_H = 125.6$ GeV	3.09 ± 0.47	5.95 ± 0.71	7.68 ± 0.98
Observed	9	15	16
5.1 fb ⁻¹ @ 7 TeV and 19.7 fb ⁻¹ @ 8 TeV			
$\bar{q}q \rightarrow ZZ$	3.78 ± 0.34	9.45 ± 0.50	11.10 ± 0.73
$Z + X$	3.39 ± 0.64	1.41 ± 0.49	5.36 ± 1.14
$gg \rightarrow ZZ$	0.23 ± 0.05	0.47 ± 0.11	0.57 ± 0.13
All background expected	7.40 ± 0.73	11.33 ± 0.71	17.03 ± 1.36
$m_H = 125.6$ GeV	3.79 ± 0.48	7.19 ± 0.73	9.35 ± 1.01
Observed	10	18	22

5.4 Kinematic Distributions

Separation between the two types of four-lepton processes can be achieved by constructing kinematic discriminants following the matrix element method approach. The kinematic discriminants \mathcal{D}_{bkg} , $\mathcal{D}_{JP}^{\text{kin}}$, $\mathcal{D}_{bkg}^{\text{dec}}$, and $\mathcal{D}_{JP}^{\text{dec}}$ are used in this analysis, and described in detail in Section 2.3.4.

Some examples of the distributions as expected from simulation and as observed in data can be seen in Figure 5.1 for the discriminants used in the spin-1 study. A complete list of all discriminants used in the analysis is presented in Table 5.5.

Observables used for the study of the exotic models	
$\mathcal{D}_{\text{bkg}} / \mathcal{D}_{\text{bkg}}^{\text{dec}}$	discriminate against ZZ background, include $m_{4\ell}$, exclude $\cos \theta^*$, Φ_1
$\mathcal{D}_{1-} / \mathcal{D}_{1-}^{\text{dec}}$	Exotic vector (1^-), $q\bar{q} \rightarrow X$
$\mathcal{D}_{1+} / \mathcal{D}_{1+}^{\text{dec}}$	Exotic pseudovector (1^+), $q\bar{q} \rightarrow X$
$\mathcal{D}_{2b+} / \mathcal{D}_{2b+}^{\text{dec}}$	KK Graviton-like with SM in the bulk (2_b^+), $q\bar{q} \rightarrow X$
$\mathcal{D}_{2h+} / \mathcal{D}_{2h+}^{\text{dec}}$	BSM tensor with higher dim operators (2_h^+), $q\bar{q} \rightarrow X$
$\mathcal{D}_{2h-} / \mathcal{D}_{2h-}^{\text{dec}}$	BSM pseudotensor with higher dim operators (2_h^-), $q\bar{q} \rightarrow X$
$\mathcal{D}_{2h2+} / \mathcal{D}_{2h2+}^{\text{dec}}$	BSM tensor with higher dim operators ($2_{h_2}^+$), $gg \rightarrow X$, $q\bar{q} \rightarrow X$
$\mathcal{D}_{2h3+} / \mathcal{D}_{2h3+}^{\text{dec}}$	BSM tensor with higher dim operators ($2_{h_3}^+$), $gg \rightarrow X$, $q\bar{q} \rightarrow X$
$\mathcal{D}_{2h6+} / \mathcal{D}_{2h6+}^{\text{dec}}$	BSM tensor with higher dim operators ($2_{h_6}^+$), $gg \rightarrow X$, $q\bar{q} \rightarrow X$
$\mathcal{D}_{2h7+} / \mathcal{D}_{2h7+}^{\text{dec}}$	BSM tensor with higher dim operators ($2_{h_7}^+$), $gg \rightarrow X$, $q\bar{q} \rightarrow X$
$\mathcal{D}_{2h9-} / \mathcal{D}_{2h9-}^{\text{dec}}$	BSM pseudotensor with higher dim operators ($2_{h_9}^-$), $gg \rightarrow X$, $q\bar{q} \rightarrow X$
$\mathcal{D}_{2h10-} / \mathcal{D}_{2h10-}^{\text{dec}}$	BSM pseudotensor with higher dim operators ($2_{h_{10}}^-$), $gg \rightarrow X$, $q\bar{q} \rightarrow X$

Table 5.5: List of kinematic discriminants used in this analyses.

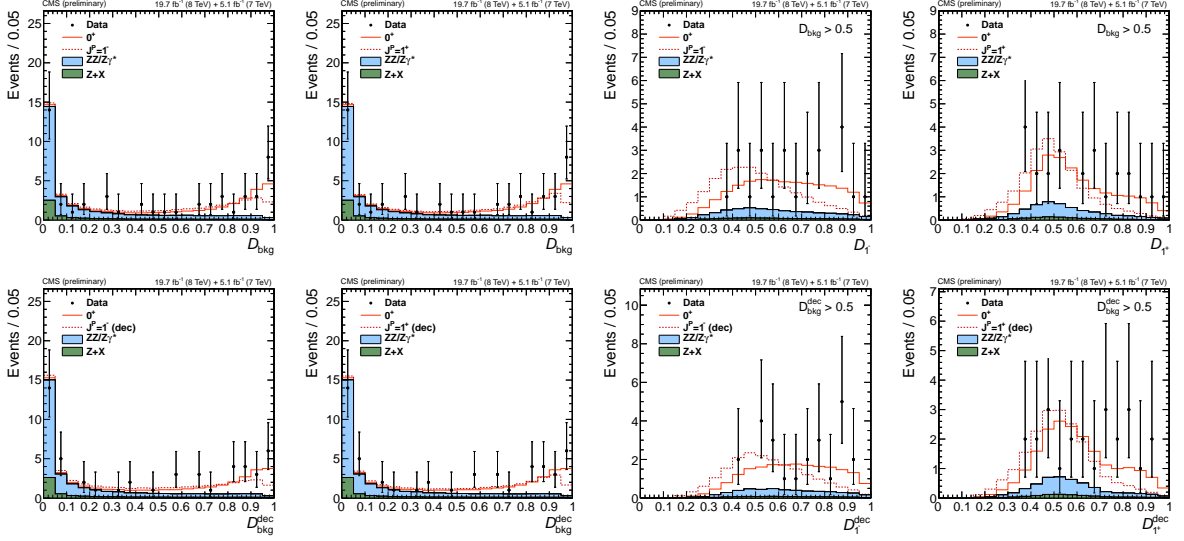


Figure 5.1: Observed distributions of the discriminants in data and MC expectations for the background and for a signal resonance at $m_H = 125.6$ GeV, either the SM Higgs boson or an alternative spin-1 hypothesis indicated. Top row from left to right: $\mathcal{D}_{\text{bkg}}(J^P = 1^-)$, $\mathcal{D}_{\text{bkg}}(J^P = 1^+)$, \mathcal{D}_{1-} , \mathcal{D}_{1+} ; bottom row from left to right: $\mathcal{D}_{\text{bkg}}^{\text{dec}}(J^P = 1^-)$, $\mathcal{D}_{\text{bkg}}^{\text{dec}}(J^P = 1^+)$, $\mathcal{D}_{1-}^{\text{dec}}$, $\mathcal{D}_{1+}^{\text{dec}}$. All distributions, except \mathcal{D}_{bkg} and $\mathcal{D}_{\text{bkg}}^{\text{dec}}$, are shown with the requirement $\mathcal{D}_{\text{bkg}} > 0.5$ ($\mathcal{D}_{\text{bkg}}^{\text{dec}} > 0.5$) to enhance signal purity.

5.5 Hypothesis Testing

To distinguish an alternative signal hypothesis from the SM Higgs boson, hypothesis testing based on kinematic discriminants is used. It is based on probability density functions packed into the 2D or 3D templates, built out of the kinematic discriminant distributions D as described before. The technical implementation of the hypothesis testing is done in the framework of the RooStats based CMS Higgs combination tools. More details are discussed in Section 4.6.4.

Events in the mass range $105.6 < m_{4\ell} < 140.6$ GeV are used to perform these studies. The Higgs boson mass is assumed to be $m_H = 125.6$ GeV. Templates are obtained from simulation for signal and irreducible background and from control regions for the reducible backgrounds, using the procedure described.

5.5.1 Spin-1

In spin-1 analysis, discrimination is based on 3D probability density functions $(\mathcal{D}_{1-}, \mathcal{D}_{1+}, \mathcal{D}_{\text{bkg}})$. The spin-1 hypotheses are also tested by relying only on their decay information, i.e. in a production-independent way, using kinematic discriminants $(\mathcal{D}_{1+}^{\text{dec}}, \mathcal{D}_{1-}^{\text{dec}}, \mathcal{D}_{\text{bkg}}^{\text{dec}})$.

Figure 5.2 shows expected 2D distributions of the discriminants $\mathcal{D}_{\text{bkg}}^{\text{dec}}$ vs. $\mathcal{D}_{1-}^{\text{dec}}$, for $q\bar{q} \rightarrow 4\ell$ background and SM. $\mathcal{D}_{\text{bkg}}^{\text{dec}}$ distributions differ significantly between signals and backgrounds.

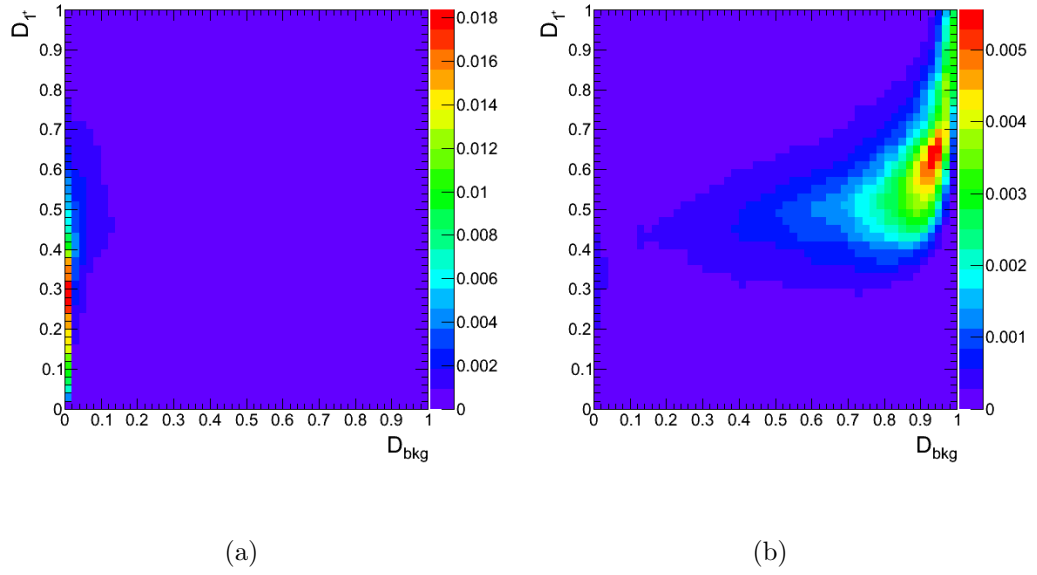


Figure 5.2: Distribution of \mathcal{D}_{bkg}^{dec} vs. \mathcal{D}_{1-}^{dec} for the qqZZ background (a) and for a signal resonance consistent with the SM Higgs boson with $m_{0+} = 125.6$ GeV. (b)

The alternative signal models are defined by the tensor structure of couplings, however, the absolute values of couplings and, hence, the expected event yields are not uniquely defined. The cross sections for alternative signal hypotheses are left floating in the fit. The same approach is taken for the SM Higgs boson hypothesis, i.e. the overall SM Higgs boson signal strength μ_S is the best fit value as it comes out from data. This way, the overall signal event yield is not a part of the discrimination between alternative hypotheses. Consequently, for pair-wise tests of alternative signal hypotheses with respect to the SM Higgs boson, the test statistic is defined using the ratio of signal plus background likelihoods for two signal hypotheses. In addition to pure 1^+ and 1^- , their mixtures with various fractions of 1^+ (f_{1^+}) are also tested.

5.5.2 Spin-2

In spin-2 analysis, discrimination is based on 2D probability density functions (D_{bkg}, D_{JP}) packed into the 2D templates. All spin-2 models are tested in $gg, q\bar{q}$ and production-independent way. When doing production-independent tests we use decay only variables ($D_{bkg}^{dec}, D_{JP}^{dec}$).

Figure 5.3 shows 2D distributions of the discriminants D_{bkg}^{dec} vs. D_{JP}^{dec} , for $q\bar{q}$ and $gg \rightarrow 4\ell$ background and Standard model. Distributions differ significantly between signal and background.

Figure 5.4 shows distribution of the D_{bkg} observable, and the production independent D_{bkg}^{dec} observable, used only to test production independent hypotheses.

In Fig. 5.5, the D_{JP} observables for selected tested hypotheses are shown.

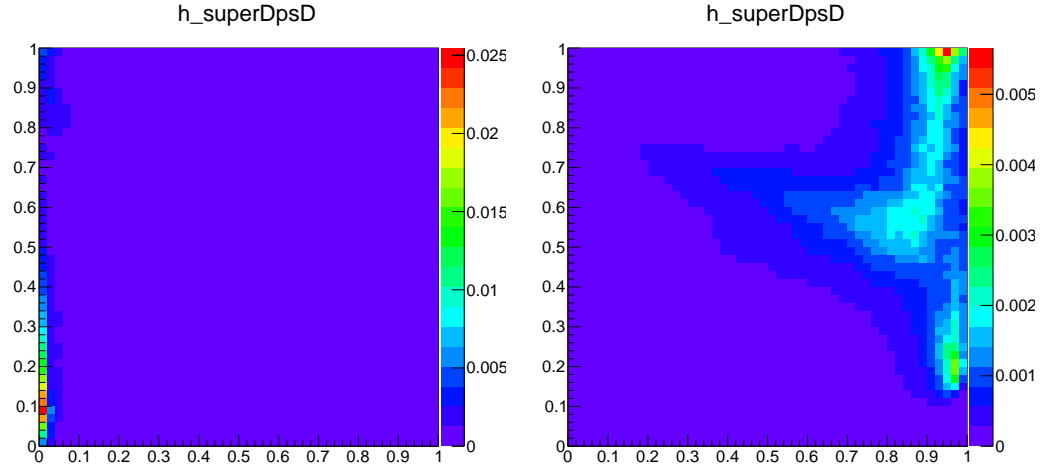


Figure 5.3: Distribution of D_{bkg}^{dec} vs. D_{JP}^{dec} for the $gg \rightarrow ZZ$ background (left) and for the signal resonance consistent with the SM Higgs boson $m_H = 125.6$ GeV model.

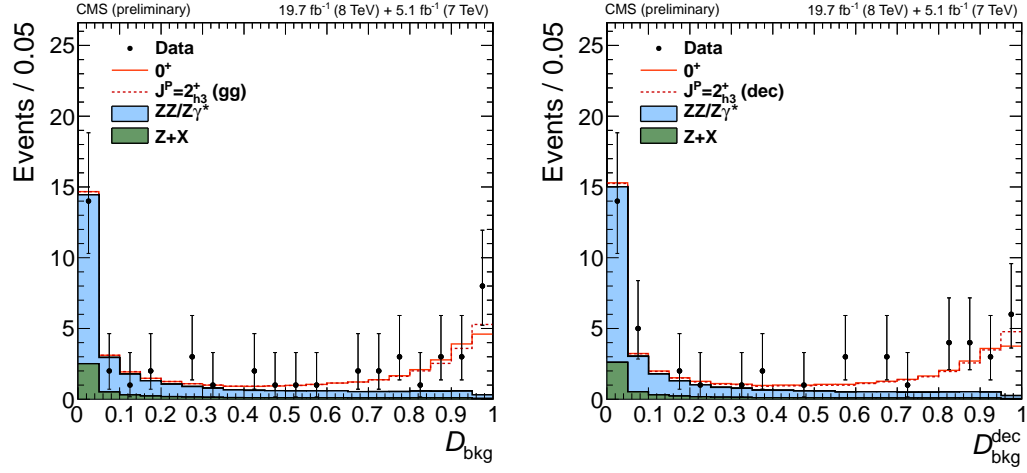


Figure 5.4: Distribution of D_{bkg} in data and MC expectations for the background and for a signal resonance consistent with SM Higgs boson at $m_H = 125.6$ GeV (left). The D_{bkg}^{dec} distribution for the production independent scenario (right).

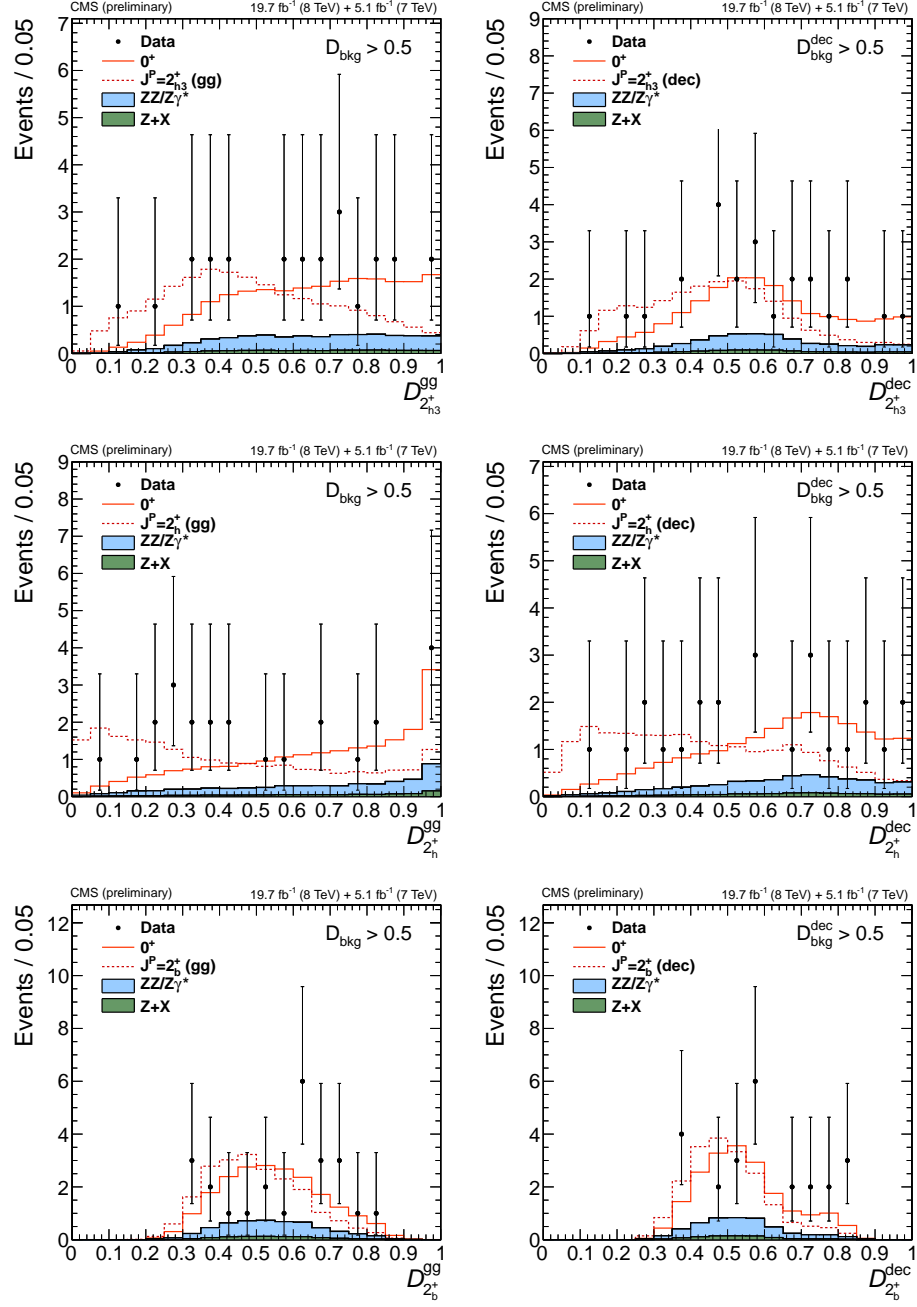


Figure 5.5: Distributions of D_{JP} with a requirement $D_{bkg} > 0.5$. Distributions for background and signal are shown.

5.6 Systematic Uncertainties

5.6.1 Theoretical uncertainties

The theoretical uncertainties are the uncertainties in the Higgs Branching Ratio to 4ℓ , QCD scale, and Parton Distribution Functions (PDF). All of these come from the latest calculations from the LHC Higgs Cross Section Working Group.²⁸ They are listed in Table 5.6.

5.6.2 Experimental uncertainties

The experimental uncertainties are the uncertainties in luminosity, lepton reconstruction and selection, and $Z + X$ estimation.

The $Z + X$ uncertainties include both the uncertainty on the expected yields and the uncertainty on the shape. Yield uncertainties are estimated to be 20%, 25%, and 40% for the $4e$, $2e2\mu$, and 4μ decay channels, respectively. The uncertainty in shape of distribution is taken into account by considering a difference between the $Z + X$ shape and the $q\bar{q} \rightarrow ZZ$ shape for a particular final state.

The lepton momentum scale leads to the resolution uncertainties on the $m_{4\ell}$ distribution, and alternative signal shapes are taken into account.

Additionally, when performing the hypothesis testing for a production independent hypothesis, another alternative shape is used to account for the MC coming from

a specific production sample. For example, if a gg MC is used to produce the default templates then a $q\bar{q}$ sample is added as a systematic variation.

These uncertainties are listed in Table 5.6. The “Production dependency” systematic is only applied when the hypothesis testing is used in a production-independent scenario.

Systematic	$4e$ 8TeV(7TeV)	4μ 8TeV(7TeV)	$2e2\mu$ 8TeV(7TeV)
Electron efficiency	10%(11%)	N/A	5%(11%)
Muon efficiency	N/A	4%(4%)	3%(3%)
Control region	20%(20%)	40%(40%)	25%(25%)
Luminosity	2.6%(2.2%)		
Missing higher-orders $q\bar{q} \rightarrow ZZ$	3%(3%)		
Missing higher-orders $gg \rightarrow ZZ$	24%(24%)		
Missing higher-orders $gg \rightarrow H$	8%(7%)		
α_S + PDF($q\bar{q}$)	3%(3%)		
α_S + PDF(gg)	7%(7%)		
Signal acceptance	2%(2%)		
Lepton resolution & scale	Shape		
$Z + X$ shape	Shape		
Production dependency	Shape		

Table 5.6: Summary of the uncertainties.

5.7 Results

5.7.1 Testing of mixed spin-1 hypotheses

The expected and observed distributions of test statistic q are shown in Figure 5.6 (production-independent) and Figure 5.7 ($q\bar{q}$ production), for all spin-1 hypotheses tested. The results are summarized in the Table 5.7 and in Fig. 5.8.

The expected separation is quoted for two scenarios, where the signal strength for each hypothesis is predetermined from the fit to data and where events are generated with SM expectations for the signal cross section ($\mu=1$). The observed separation quotes consistency of the observation with the 0^+ model or J^P model and corresponds to the scenario where the signal strength is floated in the fit to data. Table also quotes the CL_s value for the J^P model. The last three columns quote the expected and observed limit at 95%C.L. on the fractional presence of J^P model as a state nearly degenerate with the 0^+ state.

The data disfavor all the spin-1 hypotheses tested and in favor of the SM hypothesis $J^P = 0^+$ with $1-\text{CL}_s$ values larger than 95% C.L.

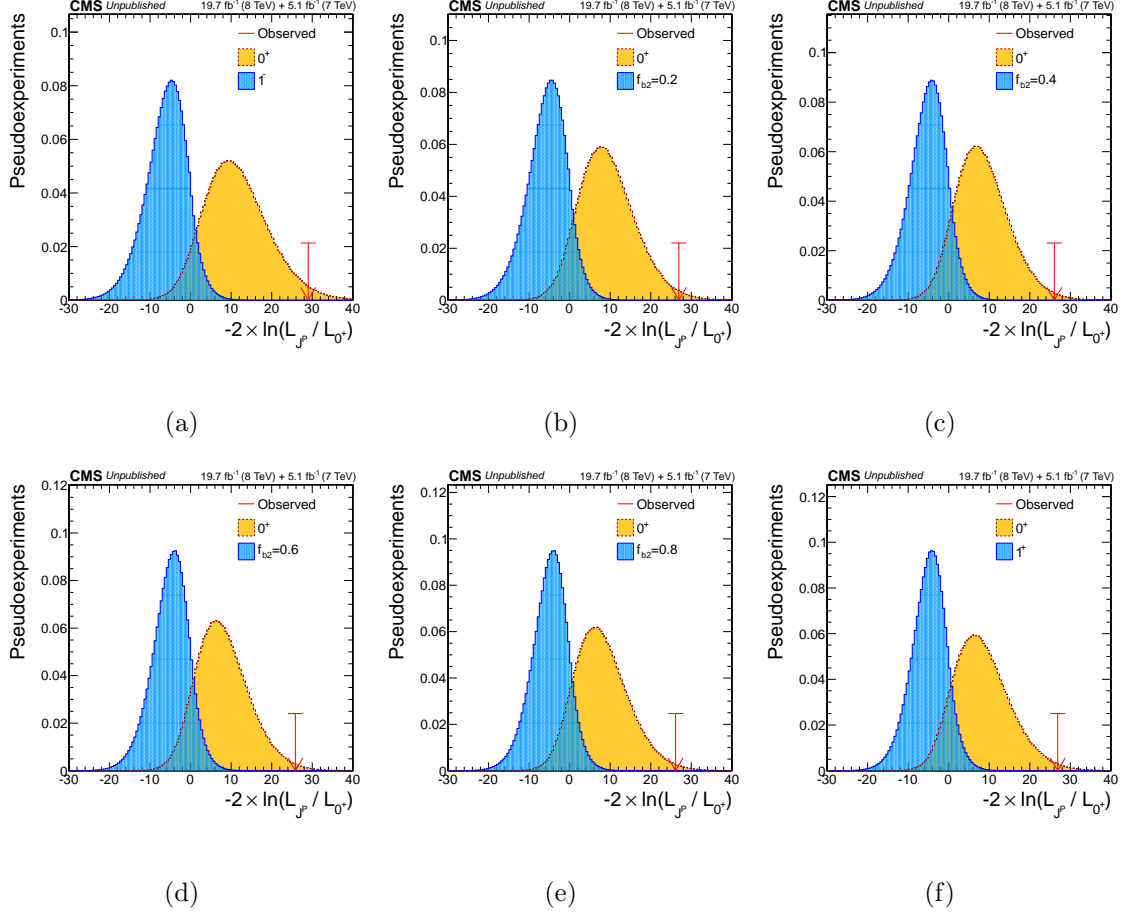


Figure 5.6: Distribution of the test-statistic $q = -2 \ln(\mathcal{L}_{J^P} / \mathcal{L}_{0^+})$ of the spin-1 hypothesis tested against the SM Higgs boson hypothesis, for the production independent scenario. $J^P = \text{pure } 1^-$ (top left), mixture with $f_{b2}=0.2$ (top middle), $f_{b2}=0.4$ (top right), $f_{b2}=0.6$ (bottom left), $f_{b2}=0.8$ (bottom middle), and pure 1^+ (bottom right). Distributions for the SM Higgs boson are represented by the yellow histogram and for the alternative J^P hypotheses by the blue histogram.

Table 5.7: A summary of models used in the analysis of spin-one hypotheses. Events are generated with SM expectation for the signal cross section ($\mu=1$).

J^P model	J^P production	Expected ($\mu=1$)	Obs. 0^+	Obs. J^P	CL_s	$f(J^P)$ CL=95% Obs(Exp)	$f(J^P)$ Best-Fit
1^-	$q\bar{q}$	2.9σ (2.8σ)	-1.4σ	$+5.0\sigma$	$<0.001\%$	<0.46 (0.78)	$0.00^{+0.16}_{-0.00}$
$f_{b2} = 0.2$	$q\bar{q}$	2.6σ (2.6σ)	-1.4σ	$+4.6\sigma$	0.002%	<0.49 (0.81)	$0.00^{+0.17}_{-0.00}$
$f_{b2} = 0.4$	$q\bar{q}$	2.5σ (2.4σ)	-1.3σ	$+4.4\sigma$	0.005%	<0.51 (0.83)	$0.00^{+0.19}_{-0.00}$
$f_{b2} = 0.6$	$q\bar{q}$	2.4σ (2.4σ)	-1.2σ	$+4.1\sigma$	0.015%	<0.53 (0.83)	$0.00^{+0.20}_{-0.00}$
$f_{b2} = 0.8$	$q\bar{q}$	2.4σ (2.4σ)	-1.0σ	$+4.0\sigma$	0.021%	<0.55 (0.83)	$0.00^{+0.21}_{-0.00}$
1^+	$q\bar{q}$	2.4σ (2.4σ)	-0.8σ	$+3.8\sigma$	0.031%	<0.57 (0.81)	$0.00^{+0.22}_{-0.00}$
1^-	any	2.9σ (2.7σ)	-2.0σ	$>5.0\sigma$	$<0.001\%$	<0.37 (0.79)	$0.00^{+0.12}_{-0.00}$
$f_{b2} = 0.2$	any	2.7σ (2.5σ)	-2.2σ	$>5.0\sigma$	$<0.001\%$	<0.38 (0.82)	$0.00^{+0.12}_{-0.00}$
$f_{b2} = 0.4$	any	2.5σ (2.4σ)	-2.3σ	$>5.0\sigma$	$<0.001\%$	<0.39 (0.84)	$0.00^{+0.13}_{-0.00}$
$f_{b2} = 0.6$	any	2.5σ (2.3σ)	-2.4σ	$>5.0\sigma$	$<0.001\%$	<0.39 (0.86)	$0.00^{+0.13}_{-0.00}$
$f_{b2} = 0.8$	any	2.4σ (2.3σ)	-2.3σ	$>5.0\sigma$	$<0.001\%$	<0.40 (0.86)	$0.00^{+0.13}_{-0.00}$
1^+	any	2.5σ (2.3σ)	-2.3σ	$>5.0\sigma$	$<0.001\%$	<0.41 (0.85)	$0.00^{+0.13}_{-0.00}$

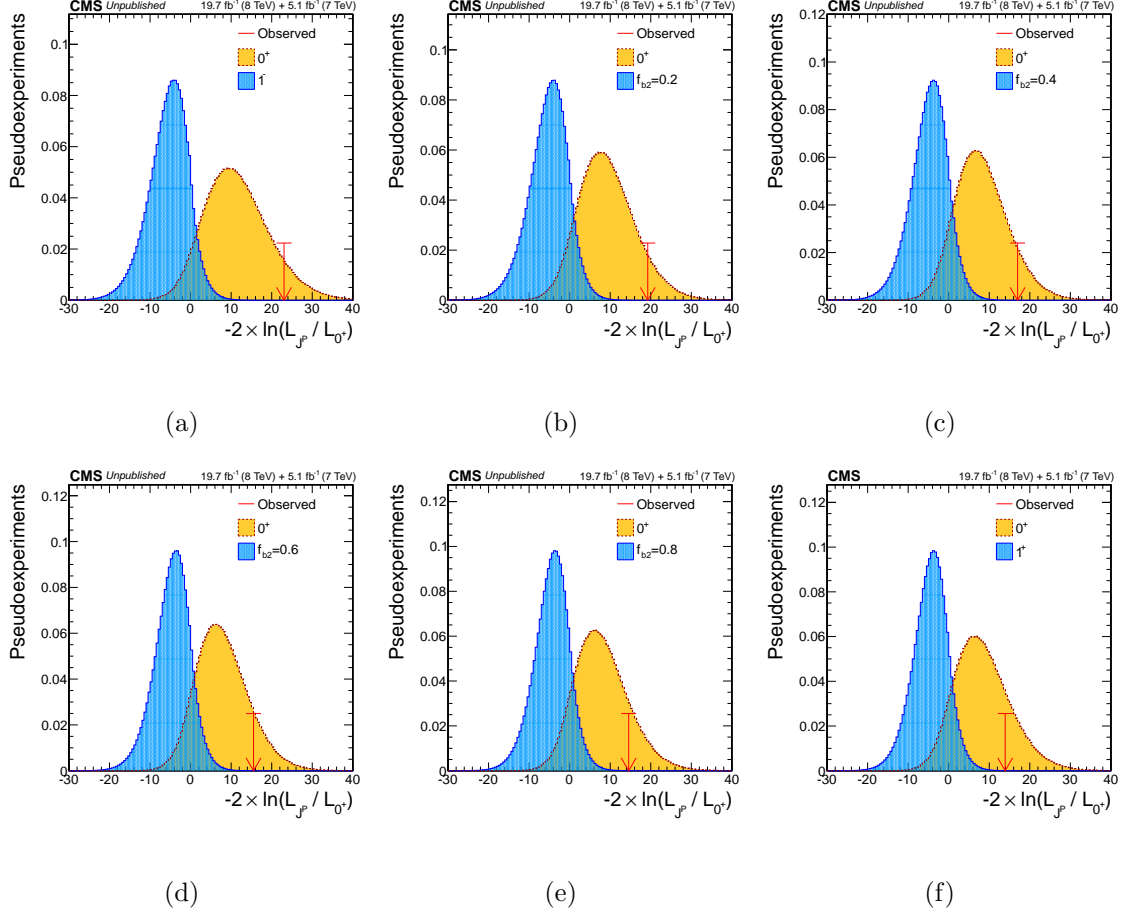


Figure 5.7: Distribution of the test-statistic $q = -2\ln(\mathcal{L}_{JP}/\mathcal{L}_{0+})$ of the spin-1 hypothesis tested against the SM Higgs boson hypothesis, for the $q\bar{q}$ production scenario. $J^P = \text{pure } 1^-$ (top left), mixture with $f_{b2}=0.2$ (top middle), $f_{b2}=0.4$ (top right), $f_{b2}=0.6$ (bottom left), $f_{b2}=0.8$ (bottom middle), and pure 1^+ (bottom right). Distributions for the SM Higgs boson are represented by the yellow histogram and for the alternative J^P hypotheses by the blue histogram.

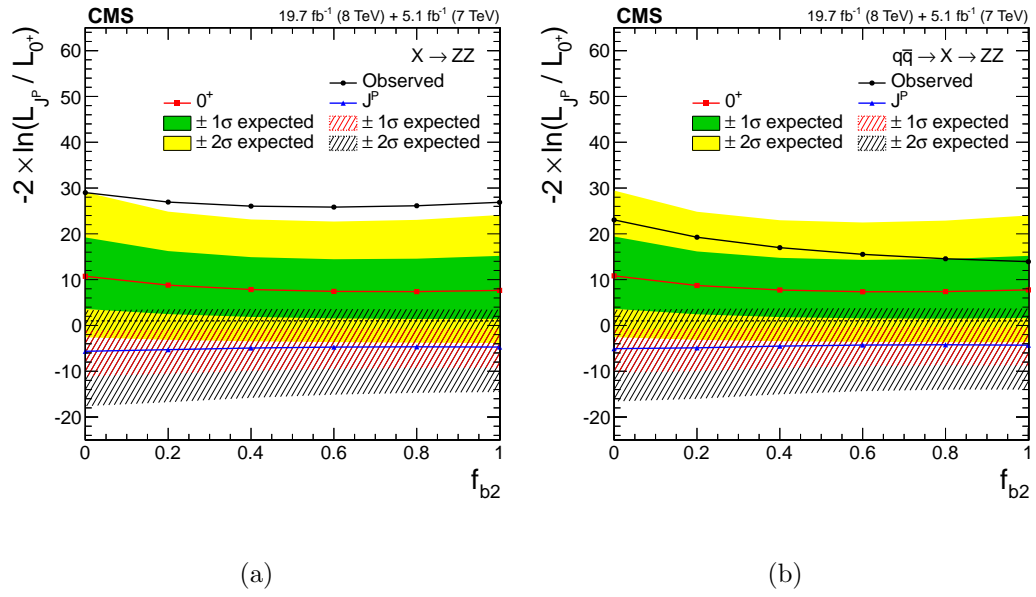


Figure 5.8: Distribution of median test statistic q , as a function of f_{b2} . The green (red) and blue (black) bands represent the 1σ and 2σ around the median expected value for the SM (spin-1) Higgs boson hypothesis.

5.7.2 Testing of spin-2 hypotheses

The expected and observed distributions of test statistic q are shown in Figure 5.9, Figure 5.10 and Figure 5.11 for all spin-2 hypotheses tested. The results are summarized in the Table 5.8. The expected and observed separations from the test statistic distributions for all the considered models are also summarized in Fig. 5.12.

The data disfavor all the spin-2 hypotheses tested and in favor of the SM hypothesis $J^P = 0^+$ with 1-CL_s values larger than 95% C.L.

J^P model	J^P prod.	Expected ($\mu=1$)	Obs. 0^+	Obs. J^P	CL _s	$f(J^P)$ 95% CL obs. (exp.)	$f(J^P)$ best fit
2_m^+	gg	1.9σ (1.8σ)	-1.1σ	$+3.0\sigma$	0.90%	<0.71 (1.00)	$0.00^{+0.30}_{-0.00}$
2_{h2}^+	gg	2.0σ (2.1σ)	-0.3σ	$+2.4\sigma$	2.0%	<0.85 (0.89)	$0.09^{+0.39}_{-0.09}$
2_{h3}^+	gg	3.2σ (3.4σ)	$+0.3\sigma$	$+3.0\sigma$	0.17%	<0.72 (0.58)	$0.13^{+0.29}_{-0.13}$
2_h^+	gg	3.8σ (4.0σ)	$+1.8\sigma$	$+2.0\sigma$	2.3%	<1.00 (0.52)	$0.48^{+0.24}_{-0.29}$
2_b^+	gg	1.6σ (1.8σ)	-1.4σ	$+3.4\sigma$	0.50%	<0.64 (1.00)	$0.00^{+0.24}_{-0.00}$
2_{h6}^+	gg	3.4σ (3.7σ)	-0.6σ	$+4.9\sigma$	$<0.001\%$	<0.38 (0.58)	$0.00^{+0.13}_{-0.00}$
2_{h7}^+	gg	3.8σ (4.5σ)	-0.3σ	$+4.5\sigma$	$<0.001\%$	<0.44 (0.43)	$0.00^{+0.19}_{-0.00}$
2_h^-	gg	4.2σ (4.5σ)	$+1.0\sigma$	$+3.2\sigma$	0.090%	<0.77 (0.47)	$0.29^{+0.21}_{-0.23}$
2_{h9}^-	gg	2.5σ (2.6σ)	-1.1σ	$+4.0\sigma$	0.029%	<0.46 (0.76)	$0.00^{+0.15}_{-0.00}$
2_{h10}^-	gg	4.2σ (4.3σ)	-0.1σ	$+4.8\sigma$	$<0.001\%$	<0.57 (0.50)	$0.06^{+0.27}_{-0.06}$
2_m^+	$\bar{q}q$	1.7σ (1.7σ)	-1.7σ	$+3.8\sigma$	0.17%	<0.56 (1.00)	$0.00^{+0.19}_{-0.00}$
2_{h2}^+	$\bar{q}q$	2.2σ (2.2σ)	-0.8σ	$+3.3\sigma$	0.26%	<0.61 (0.86)	$0.00^{+0.23}_{-0.00}$
2_{h3}^+	$\bar{q}q$	3.1σ (3.0σ)	$+0.2\sigma$	$+3.0\sigma$	0.21%	<0.81 (0.70)	$0.13^{+0.40}_{-0.13}$
2_h^+	$\bar{q}q$	4.0σ (3.9σ)	$+0.2\sigma$	$+3.9\sigma$	0.008%	<0.71 (0.53)	$0.21^{+0.28}_{-0.21}$
2_b^+	$\bar{q}q$	1.7σ (1.7σ)	-1.9σ	$+4.1\sigma$	0.062%	<0.45 (1.00)	$0.00^{+0.14}_{-0.00}$
2_{h6}^+	$\bar{q}q$	3.4σ (3.3σ)	-0.2σ	$+4.0\sigma$	0.008%	<0.74 (0.71)	$0.04^{+0.45}_{-0.04}$
2_{h7}^+	$\bar{q}q$	4.1σ (3.9σ)	$+0.4\sigma$	$+3.8\sigma$	0.010%	<0.77 (0.55)	$0.35^{+0.23}_{-0.28}$
2_h^-	$\bar{q}q$	4.3σ (4.4σ)	$+0.0\sigma$	$+4.6\sigma$	$<0.001\%$	<0.57 (0.48)	$0.01^{+0.31}_{-0.01}$
2_{h9}^-	$\bar{q}q$	2.4σ (2.2σ)	$+0.5\sigma$	$+2.0\sigma$	3.1%	<0.99 (0.86)	$0.31^{+0.43}_{-0.31}$
2_{h10}^-	$\bar{q}q$	4.0σ (3.9σ)	$+0.4\sigma$	$+4.0\sigma$	0.006%	<0.75 (0.59)	$0.30^{+0.26}_{-0.30}$
2_m^+	any	1.5σ (1.5σ)	-1.6σ	$+3.4\sigma$	0.71%	<0.63 (1.00)	$0.00^{+0.22}_{-0.00}$
2_{h2}^+	any	1.9σ (2.0σ)	-0.9σ	$+3.0\sigma$	0.74%	<0.66 (0.95)	$0.00^{+0.27}_{-0.00}$
2_{h3}^+	any	3.0σ (3.1σ)	$+0.0\sigma$	$+3.1\sigma$	0.18%	<0.69 (0.64)	$0.00^{+0.35}_{-0.00}$
2_h^+	any	3.8σ (4.0σ)	$+0.3\sigma$	$+3.6\sigma$	0.025%	<0.64 (0.49)	$0.07^{+0.30}_{-0.07}$
2_b^+	any	1.7σ (1.7σ)	-1.6σ	$+3.6\sigma$	0.29%	<0.55 (1.00)	$0.00^{+0.19}_{-0.00}$
2_{h6}^+	any	3.3σ (3.4σ)	-0.3σ	$+4.2\sigma$	0.003%	<0.54 (0.62)	$0.00^{+0.23}_{-0.00}$
2_{h7}^+	any	4.0σ (4.2σ)	$+0.6\sigma$	$+3.5\sigma$	0.032%	<0.70 (0.47)	$0.17^{+0.28}_{-0.17}$
2_h^-	any	4.2σ (4.6σ)	-0.2σ	$+4.8\sigma$	$<0.001\%$	<0.48 (0.43)	$0.04^{+0.21}_{-0.04}$
2_{h9}^-	any	2.2σ (2.1σ)	-0.6σ	$+2.9\sigma$	0.57%	<0.69 (0.89)	$0.00^{+0.27}_{-0.00}$
2_{h10}^-	any	3.9σ (4.0σ)	$+0.1\sigma$	$+4.3\sigma$	0.002%	<0.61 (0.54)	$0.08^{+0.30}_{-0.08}$

Table 5.8: List of models used in the analysis of the spin-two hypotheses corresponding to the pure states of the type noted.

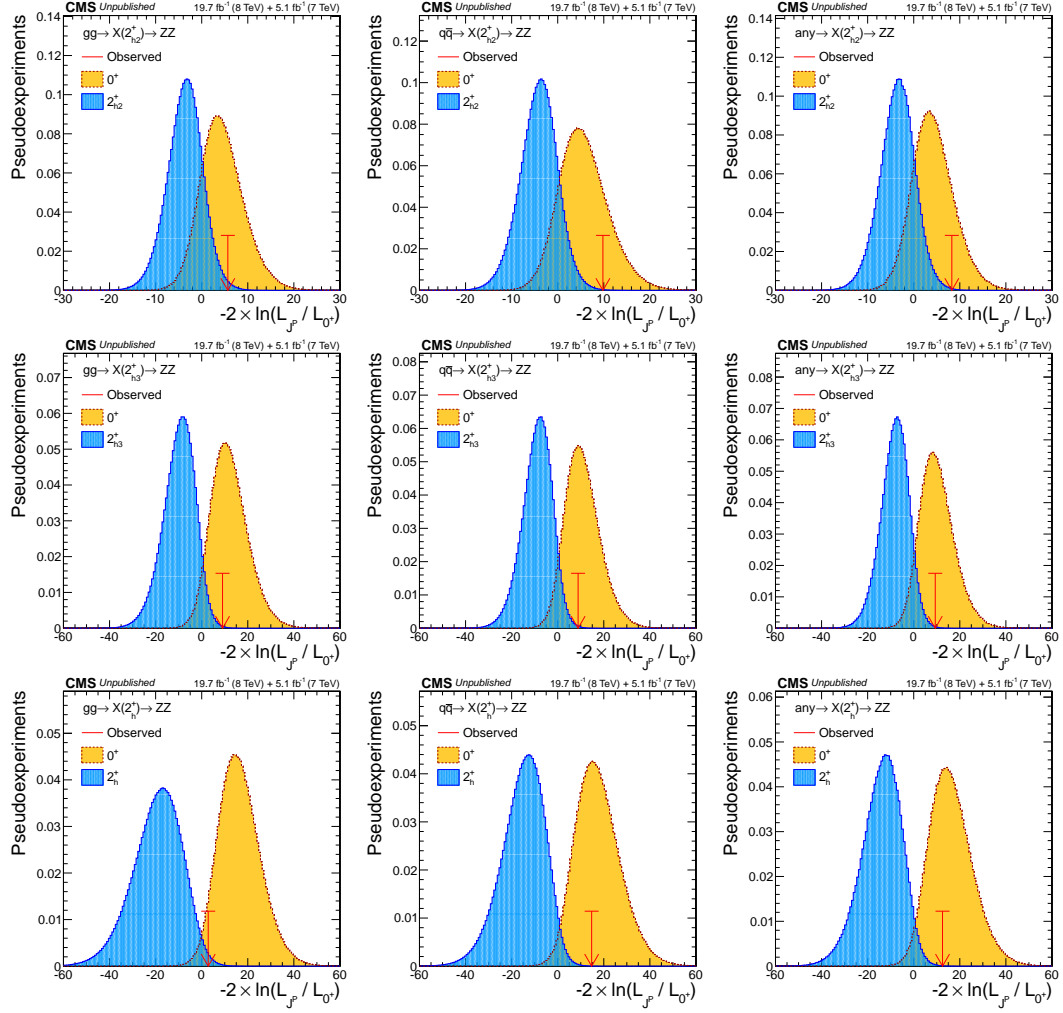


Figure 5.9: Distribution of test-statistics $q = -2\ln(\mathcal{L}_{JP}/\mathcal{L}_{0+})$ for two signal types (0^+ represented by the yellow histogram and alternative hypothesis by the blue histogram) for $m_H = 125.6 \text{ GeV}$ shown with a large number of generated experiments. Red arrow represents the observed value of the test-statistics.

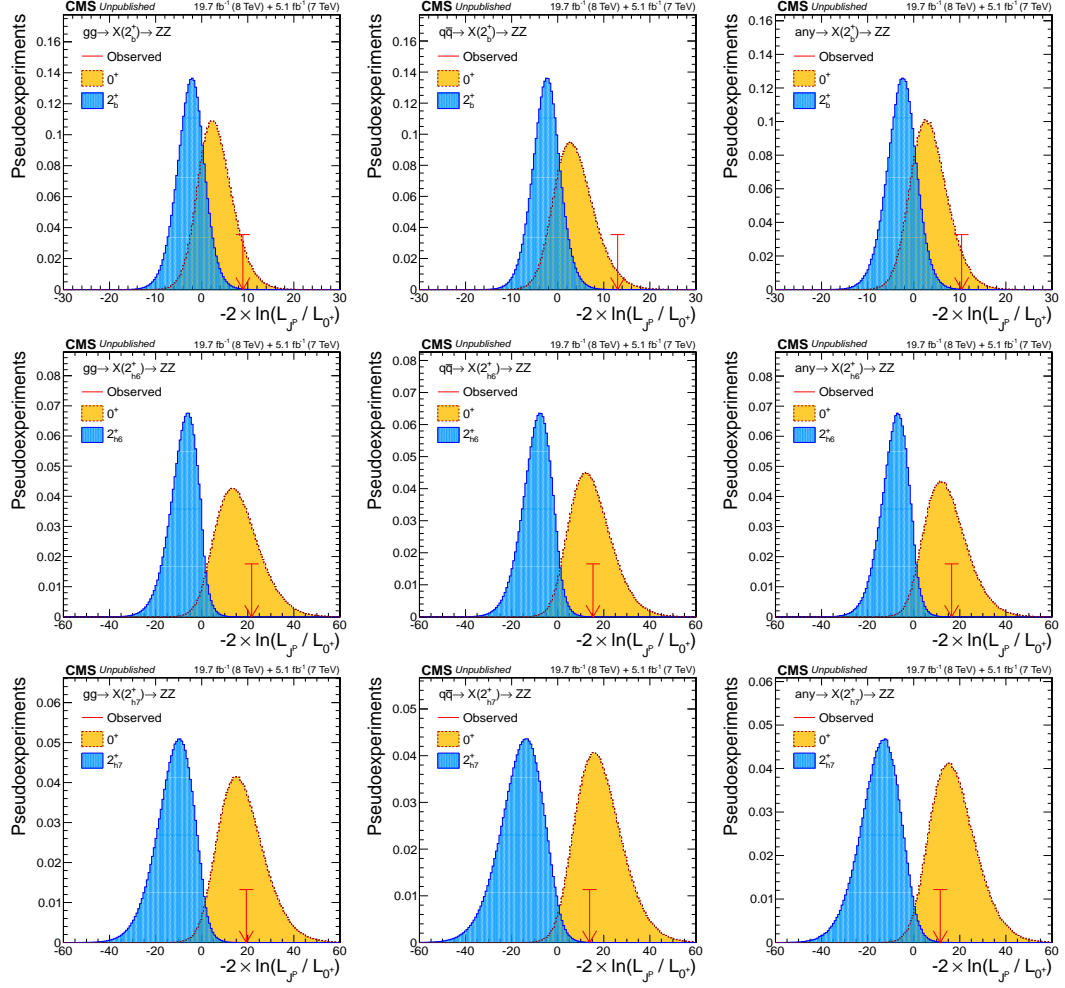


Figure 5.10: Distribution of $q = -2\ln(\mathcal{L}_{JP}/\mathcal{L}_{0^+})$ for two signal types (0^+ represented by the yellow histogram and alternative hypothesis by the blue histogram) for $m_H = 125.6$ GeV shown with a large number of generated experiments. Ten alternative hypotheses are tested in gg , $q\bar{q}$ and production model independent way.

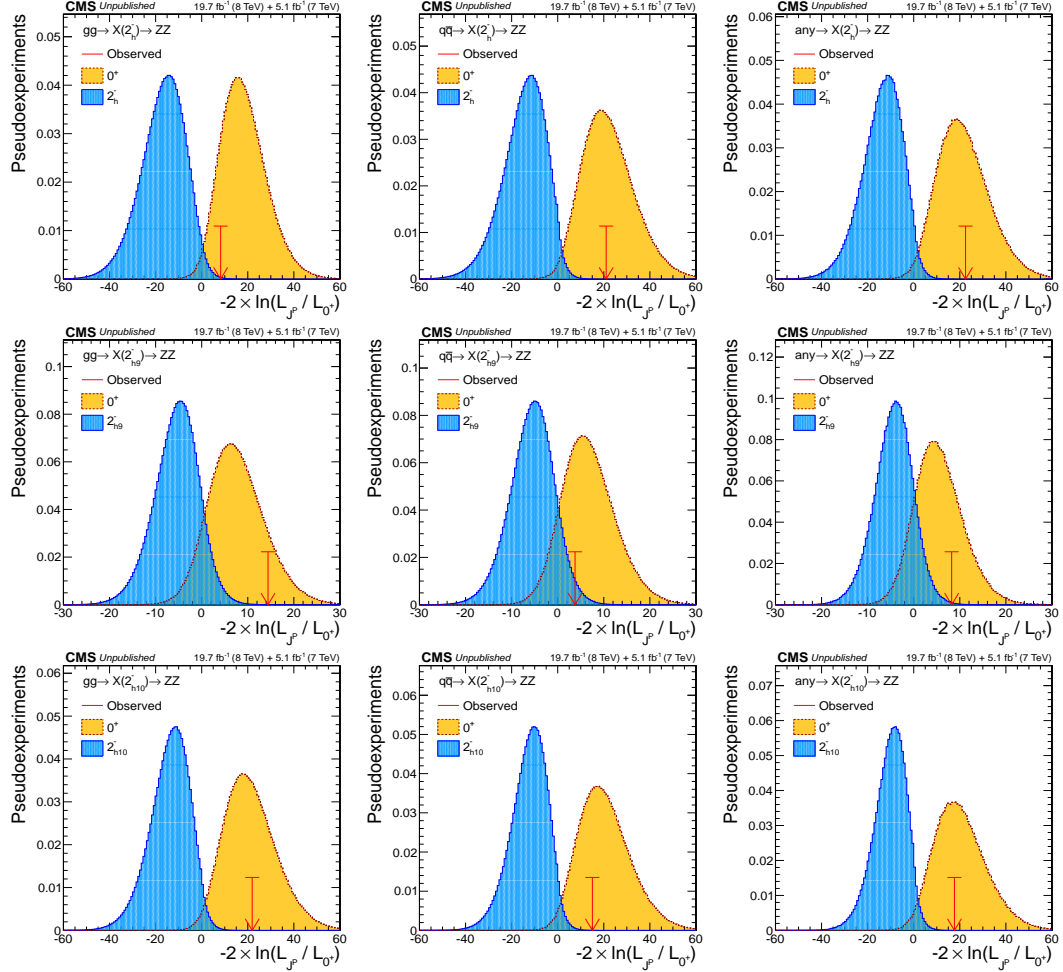


Figure 5.11: Distribution of $q = -2\ln(\mathcal{L}_{JP} / \mathcal{L}_{0+})$ for two signal types (0^+ represented by the yellow histogram and alternative hypothesis by the blue histogram) for $m_H = 125.6$ GeV shown with a large number of generated experiments. Ten alternative hypotheses are tested in gg , $q\bar{q}$ and production model independent way.

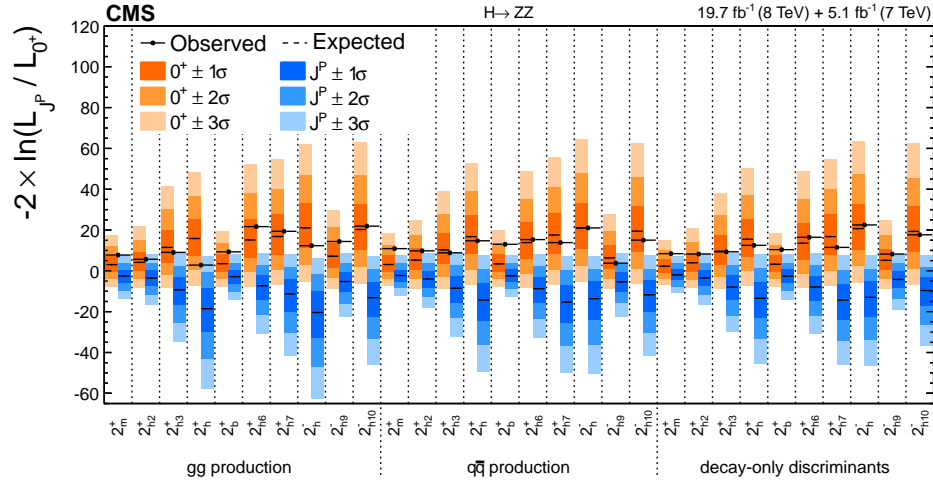


Figure 5.12: Summary of the expected and observed values for the test-statistic q distributions for the twelve alternative hypotheses tested with respect to the SM Higgs boson. The orange (blue) bands represent the 1σ , 2σ , and 3σ around the median expected value for the SM Higgs boson hypothesis (alternative hypothesis). The black point represents the observed value.

5.7.3 Constrains on mixed non-interfering states

the production of a second resonance with different J^P quantum numbers but close in mass to the SM Higgs-like state can be probed. The two states are assumed to be sufficiently separated in mass or produced by different mechanisms, so that they do not interfere, but still to be closer than the experimental mass resolution

$$\Gamma_{J^P} \text{ and } \Gamma_{0^+} \ll |m_{J^P} - m_{0^+}| \ll \delta_m \sim 1\text{GeV}. \quad (5.1)$$

The fractional cross section $f(J^P)$ is defined as follows

$$f(J^P) = \frac{\sigma_{J^P}}{\sigma_{0^+} + \sigma_{J^P}}, \quad (5.2)$$

where σ_{J^P} (σ_{0^+}) is the cross section of the process corresponding to the J^P (0^+) model defined at the LHC energy of 8TeV and, in the case of the ZZ channel, for the $X \rightarrow ZZ \rightarrow 2e2\mu$ decay mode. In this case the notation J^P refers to a model name and in practice should reflect all relevant model properties, including spin, parity, production, and decay modes.

Figures 5.13 and Figure 5.14 show the likelihood scans of $f(J^P)$ for the spin-1 hypotheses, in the production-independent and $q\bar{q}$ cases, respectively. The observed non-interfering fraction measurements are also summarized in Table 5.7, and Figure 5.15

Figures 5.16, Figure 5.17, and Figure 5.18 show the likelihood scans of $f(J^P)$ for the spin-2 hypotheses, in the production-independent, gg , and $\bar{q}q$ cases, respectively.

The observed non-interfering fraction measurements are also summarized in Table 5.8 and Figure 5.19.

These results are consistent with the SM signal. Each of these fractions is tested and reported independently of the other hypotheses, but there are correlations of kinematic distributions between the various alternative hypotheses.

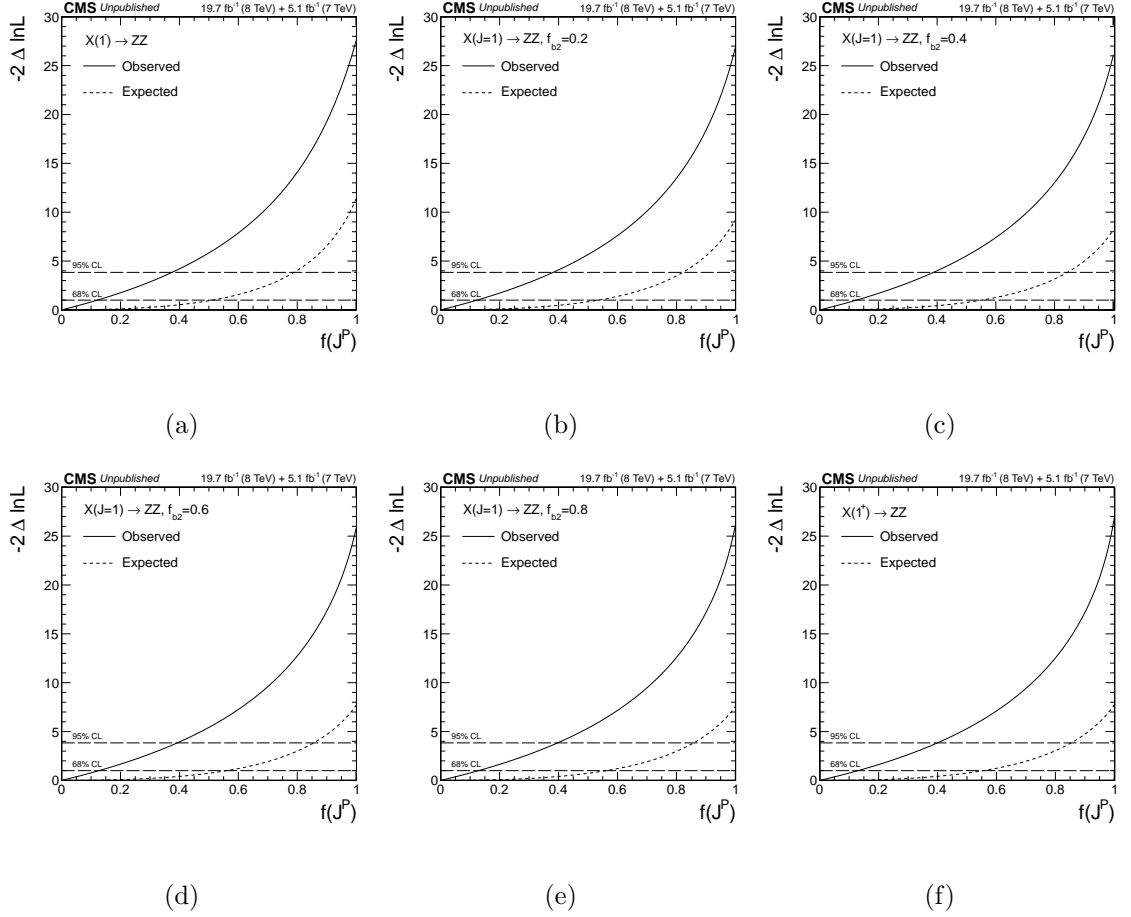


Figure 5.13: Expected and observed distributions of $-2\Delta\ln\mathcal{L}$ as a function of $f(J^P)$, in the production independent ($\text{any} \rightarrow J^P$) case. $J^P = \text{pure } 1^-$ (top left), mixture with $f_{b2}=0.2$ (top middle), $f_{b2}=0.4$ (top right), $f_{b2}=0.6$ (bottom left), $f_{b2}=0.8$ (bottom middle), and pure 1^+ (bottom right). The horizontal lines at $-2\Delta\ln\mathcal{L} = 1$ and 3.84 represent the 68% and 95% C.L., respectively.

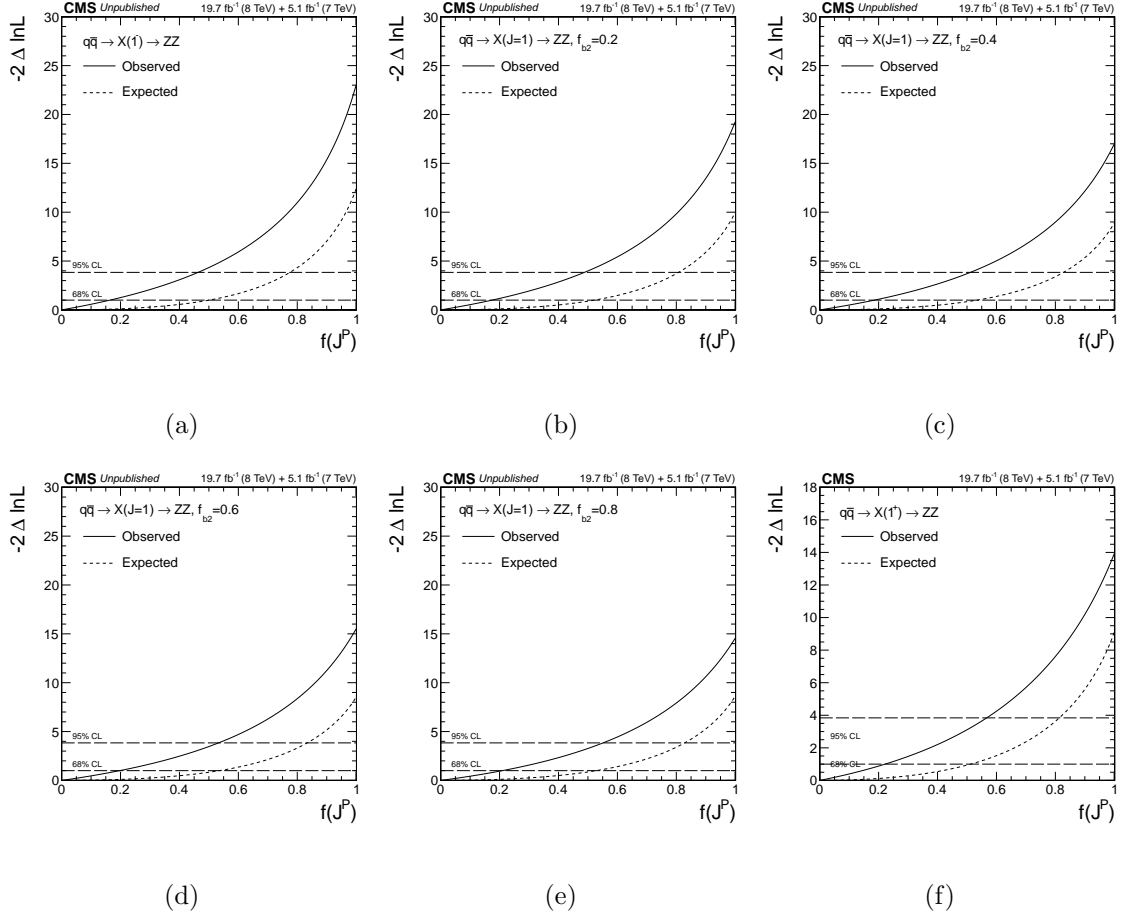


Figure 5.14: Expected and observed distributions of $-2\Delta\ln\mathcal{L}$ as a function of $f(J^P)$, in the $q\bar{q}$ production case. $J^P = \text{pure } 1^-$ (top left), mixture with $f_{b2}=0.2$ (top middle), $f_{b2}=0.4$ (top right), $f_{b2}=0.6$ (bottom left), $f_{b2}=0.8$ (bottom middle), and pure 1^+ (bottom right). The horizontal lines at $-2\Delta\ln\mathcal{L} = 1$ and 3.84 represent the 68% and 95% C.L., respectively.

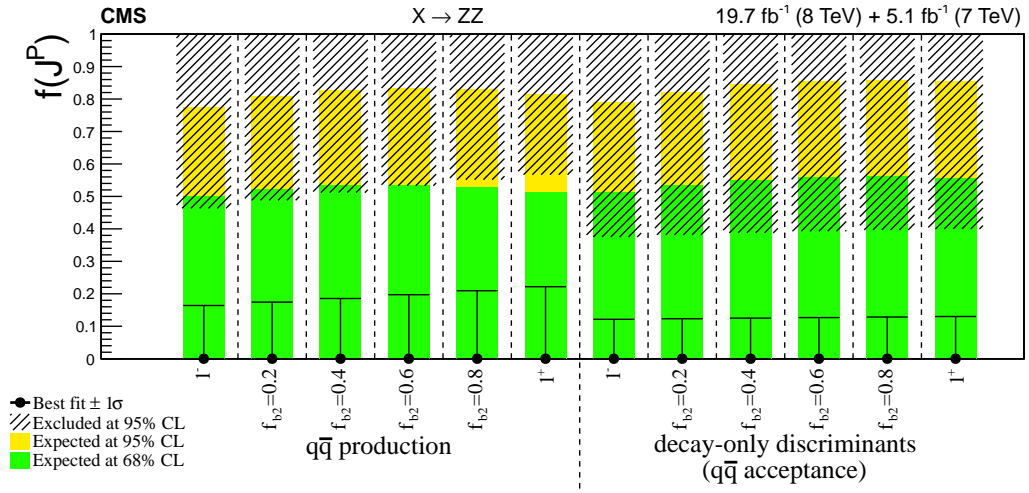


Figure 5.15: Summary of expected and observed constraints on the non-interfering fraction measurements for spin-1.

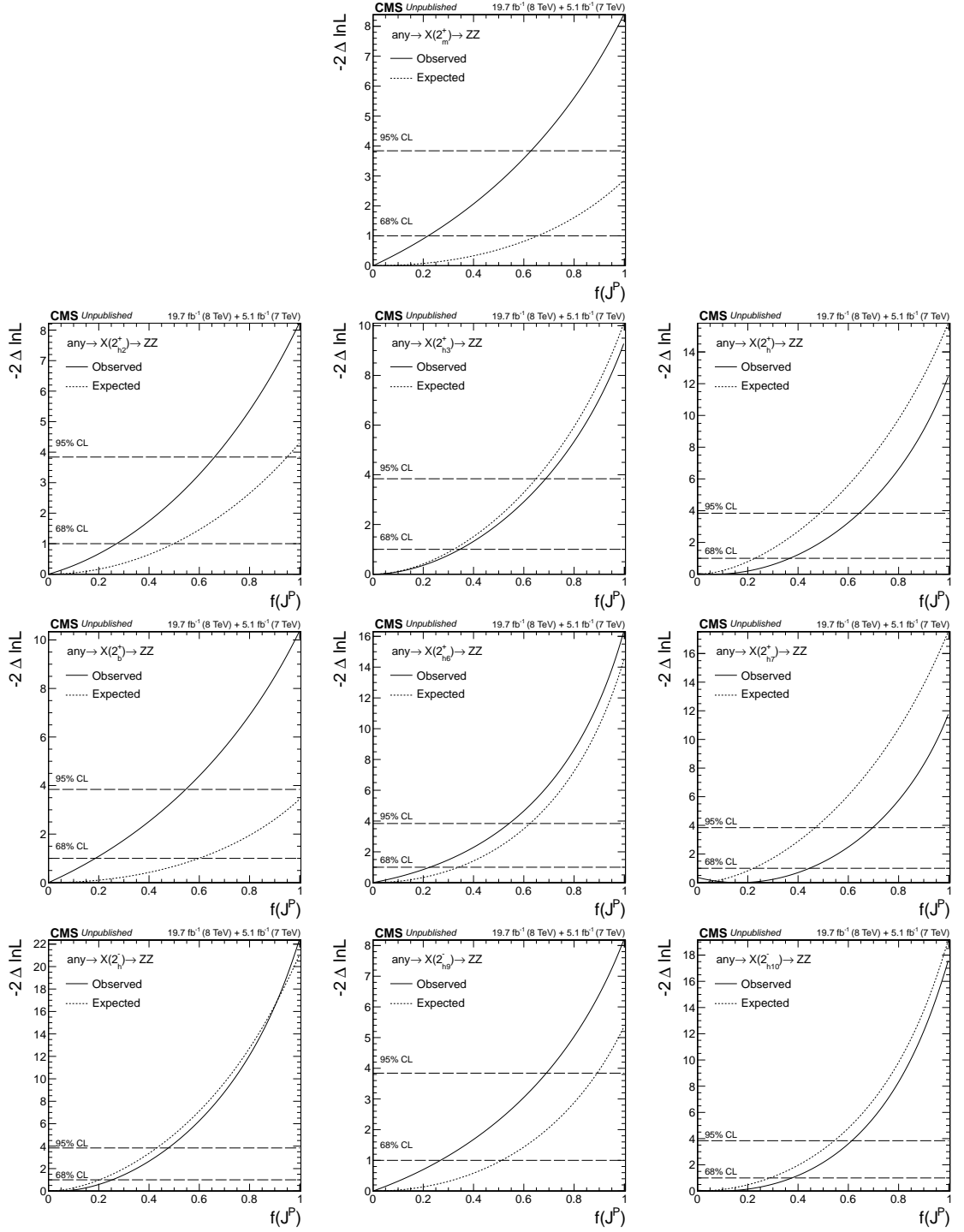


Figure 5.16: Non-interfering fraction expectations for various spin-2 models. The above results are production-independent.

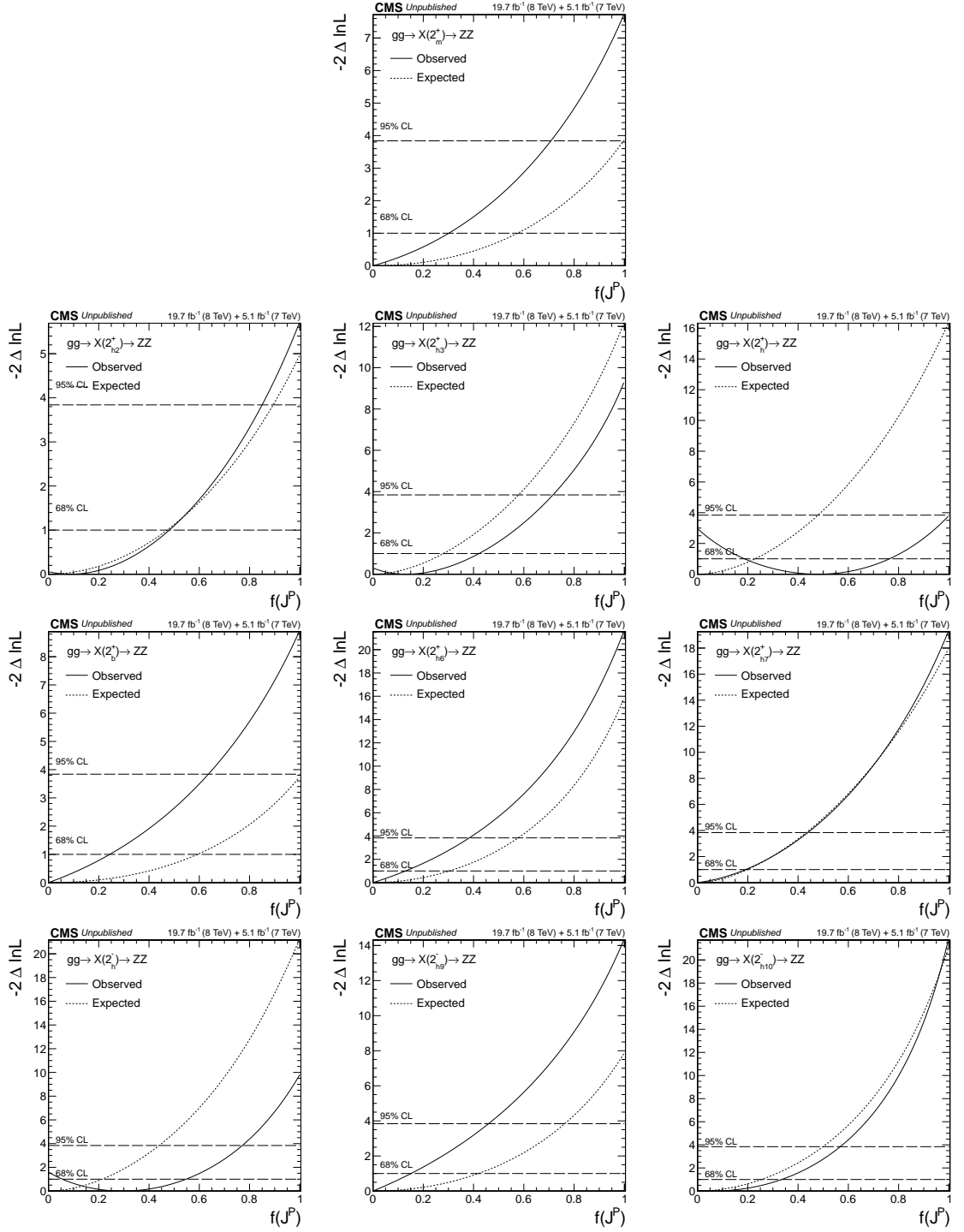


Figure 5.17: Non-interfering fraction expectations for various spin-2 models ($gg \rightarrow J^P$).

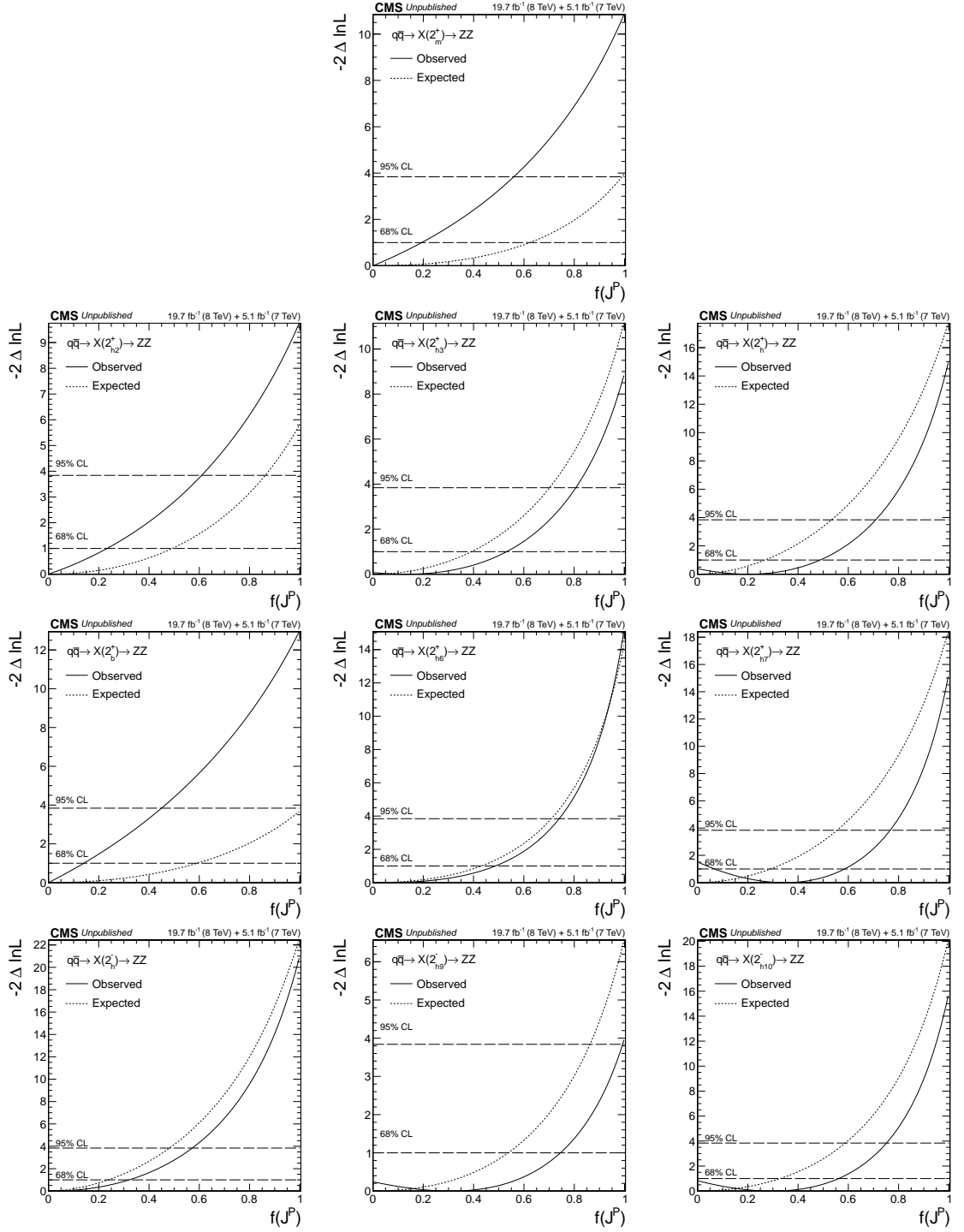


Figure 5.18: Non-interfering fraction expectations for various spin-2 models ($q\bar{q} \rightarrow J^P$).

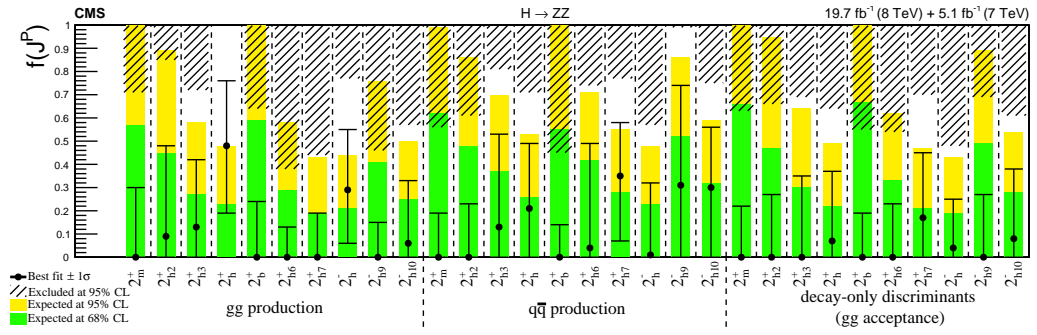


Figure 5.19: Summary of expected and observed constraints on the non-interfering fraction measurements for spin-2.

5.8 Summary of the exotic spin studies

The exotic-spin study covers the analysis of mixed-parity spin-one states and ten spin-two hypotheses under the assumption of production either via gluon fusion or quark-antiquark annihilation, or without such an assumption.

The spin-one hypotheses are excluded at a greater than 99.999% C.L. The spin-two boson with gravity-like minimal couplings is excluded at a 99.87% C.L., and the other spin-two hypotheses tested are excluded at a 99% C.L. or higher.

Chapter 6

Search for High Mass $X \rightarrow VV$

Resonances

This section presents the search for a heavy partner of the H(125), as predicted by two-Higgs-doublet models (2HDM). ZZ decay mode is one of the dominant decay channels for SM-like Higgs boson with mass above the $2m_Z$ threshold. This analysis is performed in both $H \rightarrow ZZ \rightarrow 4\ell$ and $H \rightarrow ZZ \rightarrow 2\ell 2q$ channels. The new resonance X is searched in a wide mass range from 130 GeV to 3 TeV, in a model-independent approach. For a given mass of the X boson, the width and production mechanism are assumed to be unknown. The parameter f_{VBF} is used to denote the fraction of electroweak production mechanism with respect to the total production mechanism. The three parameters m_X , Γ_X , and f_{VBF} are scanned over a wide range of allowed phase space. If the new resonance have a large width, there will be sizable interference

between $X \rightarrow ZZ \rightarrow 4f$ process and SM background production of $ZZ/Z\gamma^* \rightarrow 4f$. The interference effect is present in both gluon fusion and electroweak production processes, which this analysis properly takes into account.

6.1 Experimental data and Simulated Samples

The full dataset recorded by the CMS experiment during 2016 with proton-proton collisions at the energy of 13 TeV is used in this analysis, corresponding to an integrated luminosity of 35.9 fb^{-1} .

Details of Monte Carlo simulation are introduced in Section 4.5. In this analysis, a wide range of masses m_X from 100 GeV to 3 TeV is generated with the width Γ_X set according to SM expectation for m_X up to 1 TeV, and $\Gamma_X = 0.5 \times m_X$ at higher masses.

The MELA matrix-element package based on JHUGEN for both $H(125)$ and X signal, and on MCFM for the continuum background, allows modeling of interference of a broad X resonance with SM background in either gluon-fusion or electroweak production, the later including vector-boson fusion and production in association with a weak vector boson.

6.2 Event Selection and Categorization

Leptons and jets are reconstructed as described in Section 4.3. Event selection is described in Section 4.4. Event categorization is described below.

6.2.1 $X \rightarrow ZZ \rightarrow 4\ell$

At high mass only two X production mechanisms are expected to dominate: gluon fusion and VBF. Two categories dedicated to the production mechanisms: VBF-jets and inclusive are used.

In addition, to compensate the efficiency loss in the electron channels at high $p_{T\text{region}}$, a Reduced Selection Category (RSE) is added. Studies have shown that the $SIP < 4$ requirement in the standard electron selection is the main driver of efficiency losses at higher p_T . The second cause of efficiency loss, particularly at higher masses, is the opposite-sign lepton charge requirement, as the charge misidentification rate increases with lepton p_T . Both requirements were designed to reduce the background, while in the high mass region background is already low. Thus, these requirements are dropped for RSE category when invariant mass of the four leptons is above 300 GeV.

The detailed selection criteria are as follows:

- **VBF-jets** requires exactly four leptons with regular criteria, there must be either two or three jets of which at most one is b-tagged, or at least four jets

and no b-tagged jets, and $\mathcal{D}_{2\text{jet}}^{\text{VBF}}$ following Eq. (2.7) is required to pass a mass dependant cut.

- **Inclusive** consists of the remaining events with regular selected leptons.
- **RSE** contains events with loosend electron selection above 300 GeV.

When more than two jets pass the selection criteria, the two jets with the highest p_T are selected for matrix element calculations.

As a result of the above selection process, events are split into eight categories: $4e$, 4μ , $2e2\mu$, in either **VBF-jets** or **inclusive** category, or $4e$ and $2e2\mu$ in RSE category. Each event is characterized by two observables ($m_{4\ell}$ and $\mathcal{D}_{\text{bkg}}^{\text{kin}}$) which are shown in Figure 6.1 with several signal hypotheses.

6.2.2 $X \rightarrow ZZ \rightarrow 2\ell 2q$

To increase the sensitivity to the different production modes, events are categorized into VBF and inclusive types. Furthermore, since a large fraction of signal events is enriched with b-flavor jets due to the presence of the $Zo \rightarrow$ decays, a b-tag category is built. The definitions are the follows:

- **VBF-jets** requires two additional and forward jets besides those reconstructing the hadronic Z boson candidate; a mass dependent cut on $\mathcal{D}_{2\text{jet}}^{\text{VBF}}$, as defined in Eq. (2.7).

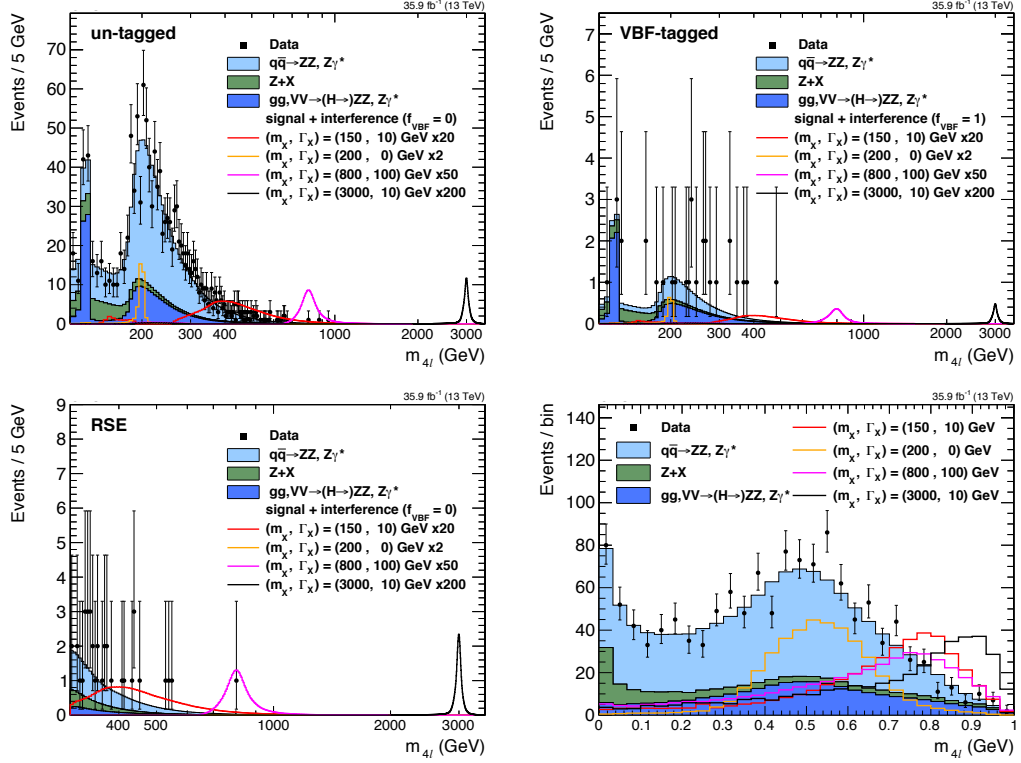


Figure 6.1: Distribution of the invariant mass of the four-leptons in un-tagged (upper left), VBF-tagged (upper right) and RSE (bottom left) category and $\mathcal{D}_{\text{bkg}}^{\text{kin}}$ (bottom right) of all the selected events. Signal expectation including the interference effect for several mass and width hypothesse are shown in the plot. The cross-section of the signal correspondes to the expected exclusion value (times a scaling to make them more visible) on the plots, and are normalizaed to a total of 400 events on the right plot.

- **b-tag** consists of the remaining events with two b-tagged jets (in the resolved case) or two b-tagged subjets from the hadronic Z boson candidate.
- **Inclusive** consists of the remaining events.

As a result of this selection process, events are split into twelve categories: $2e2q$ or $2\mu2q$, either **VBF-jets**, **b-tagged**, or **inclusive**, and each with either **merged jets** or **resolved jets**. Each event is characterized by two observables $(m_{2\ell2q}, \mathcal{D}_{Zjj})$.

Figure 6.2 shows the invariant mass distribution for merged and resolved events in different categories after the selections.

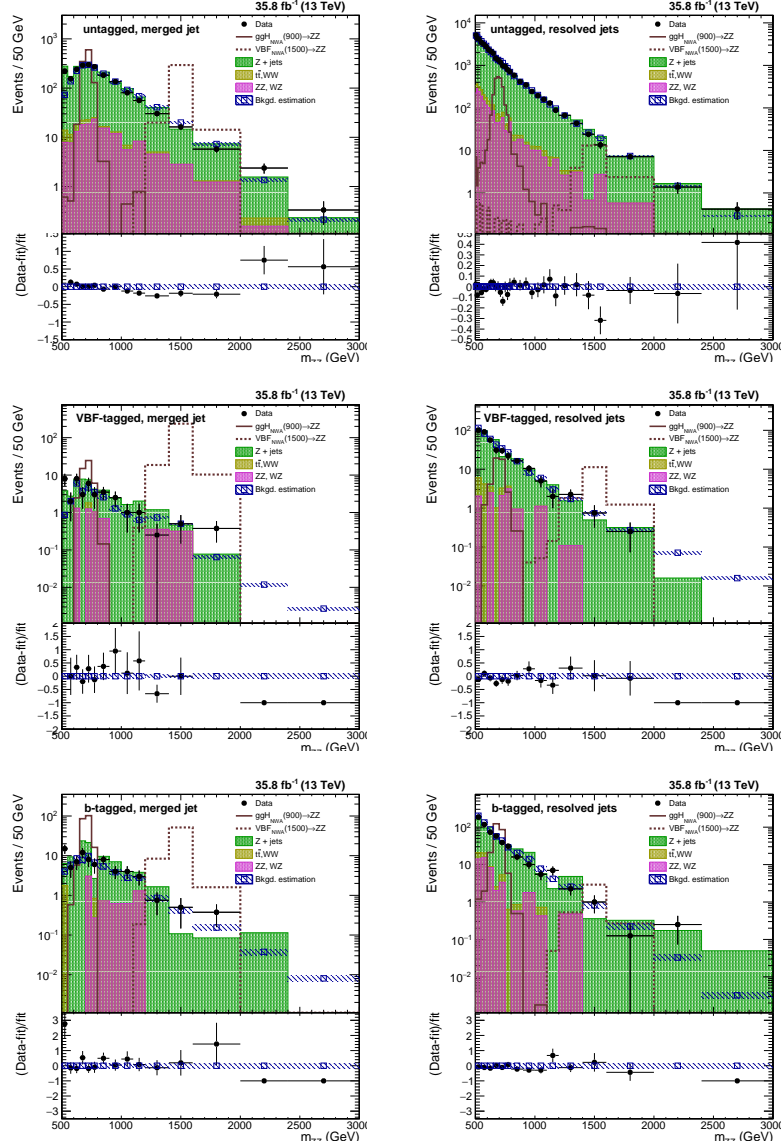


Figure 6.2: Invariant mass distribution m_{ZZ} in the signal region for the merged (left) and resolved (right) case in the different categories. The points are the observed data, the stacked histograms are the standard model simulated background, and the open histograms are simulated signal samples. The blue hatched bands refer to the sum of MC- and data-derived background estimations. Lower panels show data/estimation ratios.

6.3 Kinematic discriminants

All Kinematic discriminants are introduced in Section 2.3.4. The matrix-element methods are used in three ways. First, they are used to apply weights in MC simulation to create various models without the need to regenerate the full MC samples. Second, the matrix element methods are used to create a model of a broad high-mass resonance X and its interference with SM background to be used in the likelihood fit. Finally, these methods are used to create optimal discriminants for either categorization of events according to likely production mechanism, or to separate signal from the dominant background.

6.3.1 $X \rightarrow ZZ \rightarrow 4\ell$

The discriminant sensitive to the VBF production is described in (2.7), and the discriminant sensitive to the $ZZ \rightarrow 4\ell$ kinematics is described in (2.5).

6.3.2 $X \rightarrow ZZ \rightarrow 2\ell 2q$

The discriminant sensitive to the $ZZ \rightarrow 2\ell 2q$ kinematics is described in (2.6). Figure 6.3 shows the distribution of \mathcal{D}_{Zjj} for several representative examples. Figures 6.4 to 6.7 show the distribution of \mathcal{D}_{Zjj} vs $m_{2\ell 2q}$ with conditional normalisation for signal and background.

The template $\mathcal{T}(\mathcal{D}_{Zjj}|m_{2\ell 2q})$ used in analysis is conditionally normalized such that

each slice of \mathcal{D}_{Zjj} is normalised to unit area for a given value of $m_{2\ell 2q}$. An analogous discriminant is defined for spin-2 signals, where the denominator probability is based on production and decay of KK graviton propagating in the bulk.

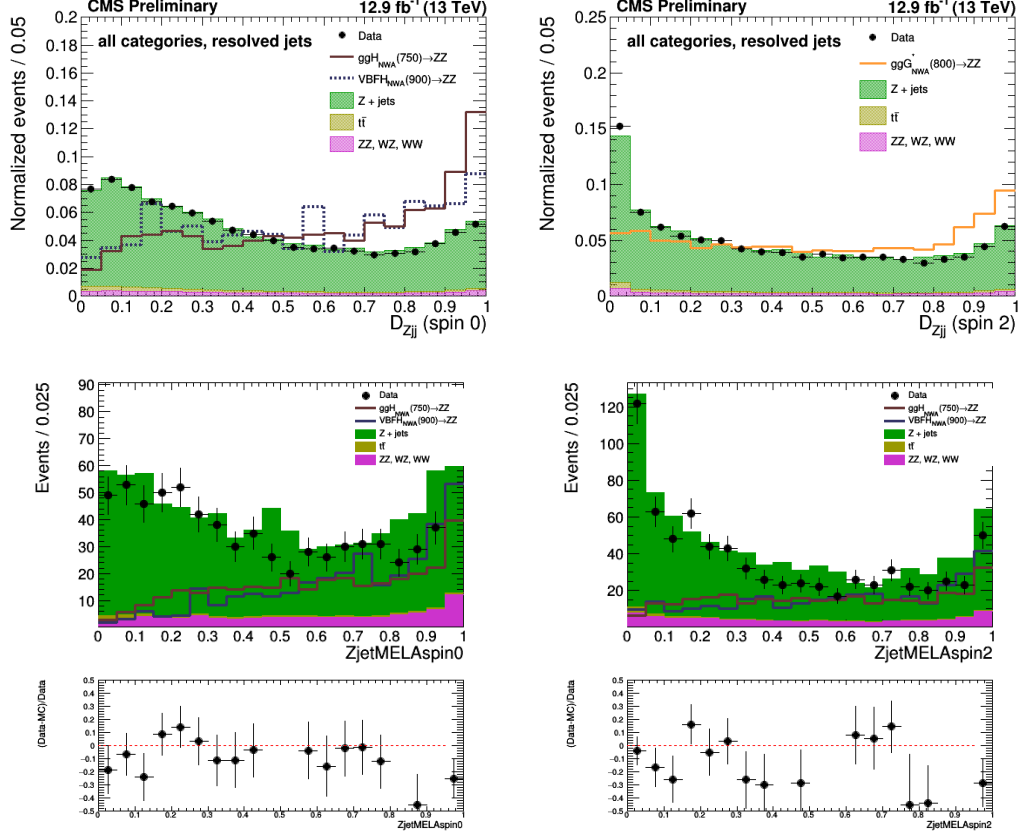


Figure 6.3: Distribution of \mathcal{D}_{Zjj} with events with two resolved jets (top) and with a merged jet (bottom). Spin-0 on the left, spin-2 on the right.

To take the different kinematics in resolved jets and in subjects (of merged jet) into account, different templates on \mathcal{D}_{Zjj} vs m_{ZZ} are derived for events passing resolved-jet based selection and merged-jet based selection. Templates for spin-0 case are given in Fig. 6.4 and 6.5, while templates for spin-2 case are given in Fig. 6.6 and 6.7.

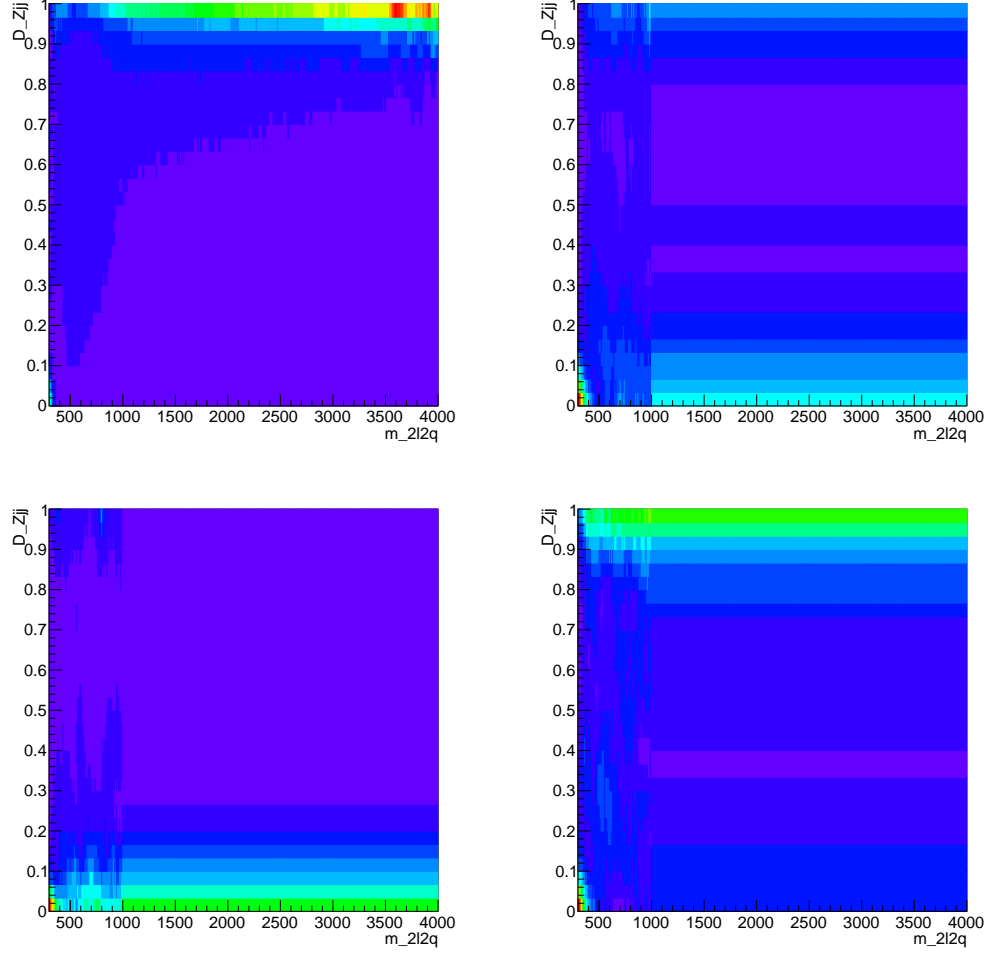


Figure 6.4: Distribution of \mathcal{D}_{Zjj} vs $m_{2\ell 2q}$ with conditional normalisation for spin-0 signal (top left), $DY + \text{jets}$ (top right), $t\bar{t} + WW$ (bottom left), ZW, ZZ diboson backgrounds (bottom left), for the merged selection. When conditionally normalised, each slice of \mathcal{D}_{Zjj} is normalised to unit area for a given value of $m_{2\ell 2q}$.

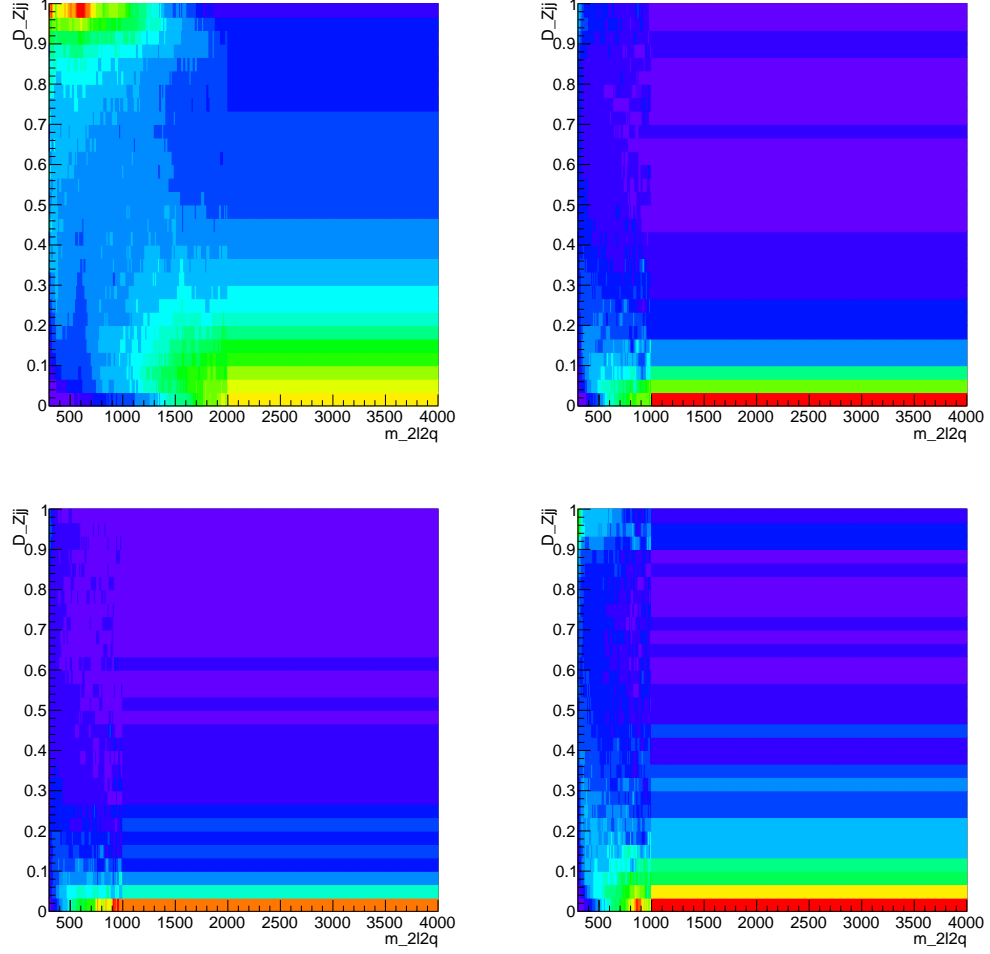


Figure 6.5: Distribution of \mathcal{D}_{Zjj} vs $m_{2\ell 2q}$ with conditional normalisation for spin-0 signal (top left), DY + jets (top right), $t\bar{t}$ + WW (bottom left), ZW, ZZ diboson backgrounds (bottom right), for the resolved selection. When conditionally normalised, each slice of \mathcal{D}_{Zjj} is normalised to unit area for a given value of $m_{2\ell 2q}$.

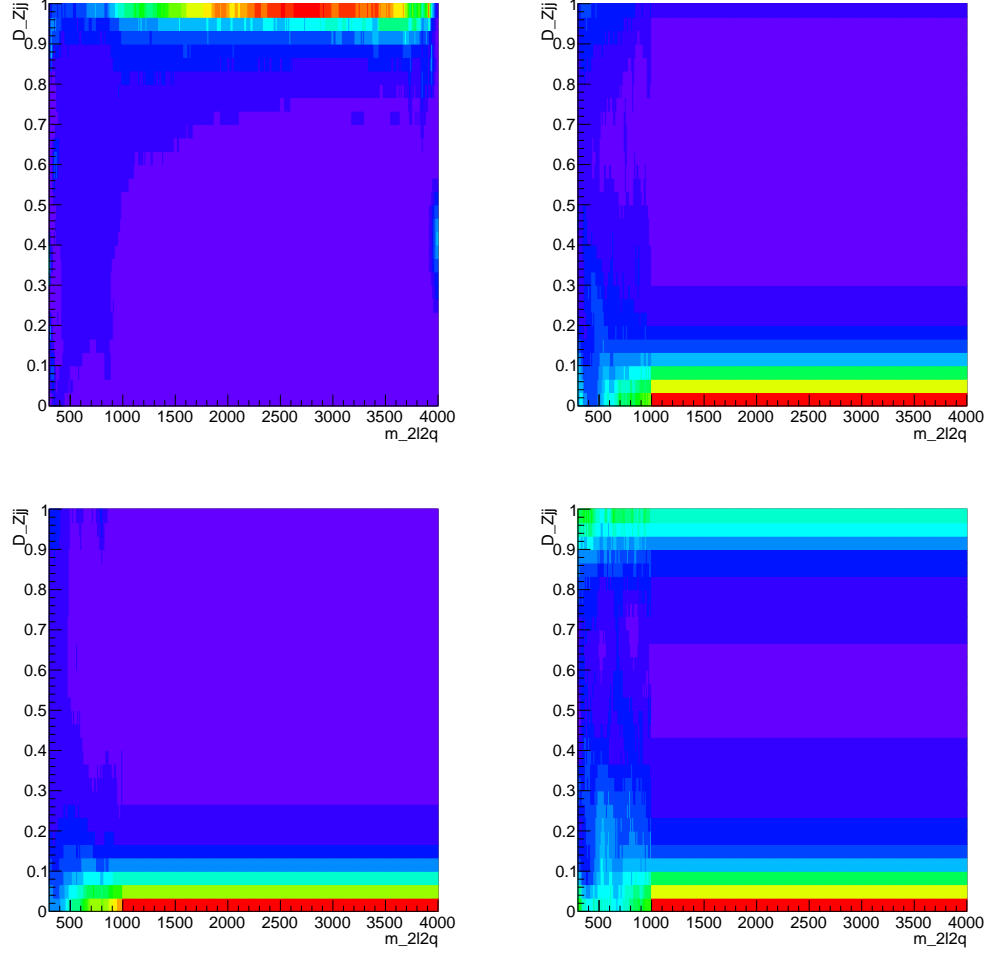


Figure 6.6: Distribution of \mathcal{D}_{Zjj} vs $m_{2\ell 2q}$ with conditional normalisation for spin-2 signal (top left), DY + jets (top right), $t\bar{t}$ + WW (bottom left), ZW, ZZ diboson backgrounds (bottom right), for the merged selection. When conditionally normalised, each slice of \mathcal{D}_{Zjj} is normalised to unit area for a given value of $m_{2\ell 2q}$.

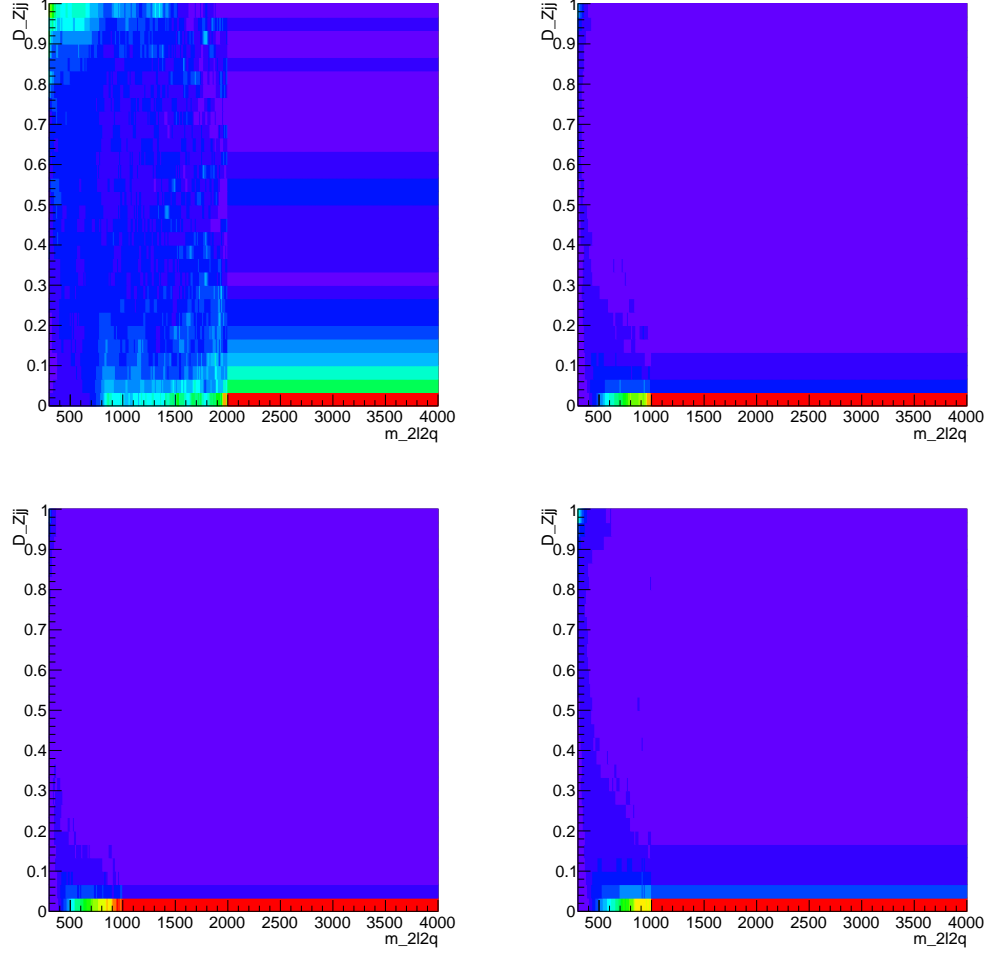


Figure 6.7: Distribution of \mathcal{D}_{Zjj} vs $m_{2\ell 2q}$ with conditional normalisation for spin-2 signal (top left), $DY + \text{jets}$ (top right), $t\bar{t} + WW$ (bottom left), ZW, ZZ diboson backgrounds (bottom right), for the resolved selection. When conditionally normalised, each slice of \mathcal{D}_{Zjj} is normalised to unit area for a given value of $m_{2\ell 2q}$.

6.4 Signal and background parameterization

The ultimate goal of the analysis is to determine if a set of X boson parameters m_X , Γ_X , and $\sigma_i \times \mathcal{B}_{ZZ}$, where the latter is the signal production cross section times $X \rightarrow ZZ$ branching fraction in each production channel i (gluon fusion or EW production), are consistent with the data. In practice, the $\sigma_i \times \mathcal{B}$ for $i = 1, 2$ are expressed in terms of $\sigma_{\text{tot}} \times \mathcal{B}_{ZZ}$ and f_{VBF} , and the confidence intervals on $\sigma_{\text{tot}} \times \mathcal{B}_{ZZ}$ are determined from profile likelihood scans for a given set of $(m_X, \Gamma_X, f_{\text{VBF}})$.

The likelihood function is maximized with respect to the nuisance parameters which include the constrained parameters describing the systematic uncertainties, as discussed in Section 4.6.2. The extended likelihood function is defined for candidate events as

$$\mathcal{L} = \exp \left(- \sum_i n_{vv}^i - \sum_i n_{\text{bkg}}^i \right) \times \prod_k \prod_j \left(\sum_i n_{vv}^i \times \mathcal{P}_{vv}^{i,k}(\vec{x}_j; m_X, \Gamma_X) + \sum_i n_{\text{bkg}}^i \times \mathcal{P}_{\text{bkg}}^{i,k}(\vec{x}_j) \right), \quad (6.1)$$

where the observables \vec{x}_j are defined for each event j in category k . There are several signal and background types i , defined for each production mechanism. The background processes which do not interfere with signal are described by the probability density functions (pdf) $\mathcal{P}_{\text{bkg}}^{i,k}(\vec{x}_j)$.

The $vv \rightarrow 4f$ process is described by the pdf $\mathcal{P}_{vv}^{i,k}(\vec{x}_j; m_X, \Gamma_X)$ for $vv = gg$ (gluon

fusion) and $vv = VV$ (EW production). This pdf describes production and decay of signal X, SM background, including $H(125)$, and interference of all these contributions and is parameterized as follows

$$\begin{aligned} \mathcal{P}_{vv}^{i,k}(\vec{x}_j; m_X, \Gamma_X) &= \mu_i \times \mathcal{P}_{vv \rightarrow X \rightarrow 4f}^{i,k}(\vec{x}_j; m_X, \Gamma_X) \\ &+ \sqrt{\mu_i} \mathcal{P}_{\text{int}}^{i,k}(\vec{x}_j; m_X, \Gamma_X) + \mathcal{P}_{vv \rightarrow 4f}^{i,k}(\vec{x}_j), \end{aligned} \quad (6.2)$$

where μ_i is the relative signal strength for production type i defined as the ratio of $\sigma_i \times \mathcal{B}$ with respect to a reference value, for which normalization of the pdf is determined. The interference contribution $\mathcal{P}_{\text{int}}^{i,k}$ scales as $\sqrt{\mu_i}$ and the pure signal as μ_i , while both of them depend on the signal parameters m_X and Γ_X .

6.5 Signal Model

The parameterization of the signal can be separated in two steps: modeling of the ideal distributions, both the shape and yield, and introducing detector effect. The signal pdf after detector effects $\mathcal{P}^{\text{reco}}(m_{4f})$ is implemented with the multiplicative efficiency function $\mathcal{E}(m_{4f})$ and convolution for the mass resolution $\mathcal{R}(m_{4f}|m_{4f}^{\text{truth}})$, both extracted from the full simulation of the $gg \rightarrow 4f$ and $VV \rightarrow 4f$ processes:

$$\mathcal{P}_{\text{sig}}^{\text{reco}}(m_{4f}) = (\mathcal{E}(m_{4f}^{\text{truth}}) \times \mathcal{P}_{\text{sig}}(m_{4f}^{\text{truth}}|m_X, \Gamma_X)) \otimes \mathcal{R}(m_{4f}|m_{4f}^{\text{truth}}). \quad (6.3)$$

The parameterization of $\mathcal{R}(m_{4f}|m_{4f}^{\text{truth}})$ and $\mathcal{E}(m_{4f}^{\text{truth}})$ covers the mass range from 100 GeV to 3.5 TeV.

6.5.1 Lineshape prior to detector effects

The ideal distribution for a narrow $H(125)$ or a high-mass resonance is simple, which can be taken as a delta function when convoluting with a resolution function. Parameterization of a broad resonance or of the off-shell tail of an $H(125)$ signal, or any other signal below $2m_Z$ threshold, requires special care of modeling the line-shape and interference with background.

The following production mechanisms are considered: gluon fusion, VBF, VH . The cross section for the $t\bar{t}H$ production mechanism is highly suppressed for $m_X > 2m_Z$ and we therefore do not consider it. The mass and width of both $H(m_H, \Gamma_H)$ and $X(m_X, \Gamma_X)$ are included as general parameters of the model.

The probability density function $\mathcal{P}^{\text{ideal}}(m_{4\ell}^{\text{ideal}}|m_X, \Gamma_X, \sigma_X)$, as implemented in RooFit and CMS combine tool, is based on the matrix element MCFM+JHUGen+HNNLO implemented within the MELA framework and has the most general parameterization of $H(m_H, \Gamma_H)$ and $X(m_X, \Gamma_X)$ for any width and mass of the resonances.

6.5.2 Efficiency

Parameterization of efficiency function $\mathcal{E}(m_{4f})$ is extracted from the full simulation of each production mechanism and each signal type with POWHEG+JHUGen simulation of the wide resonance with $\Gamma_X = \Gamma_H^{\text{SM}}(m_H)$.

Efficiency is parameterized separately for each 4ℓ final state ($2e2\mu$, $4e$, 4μ), and for

each of the 12 $l\bar{l}tq$ categories. To have a smooth estimation of efficiency in our search region, a total of 57 mass points are used for fitting the 4ℓ efficiency distribution: 115, 120, 124, 125, 126, 130, 135, 140, 145, 150, 155, 160, 165, 170, 175, 180 within 1 GeV of m_H ; 190, 200, 210, 230, 250, 270, 300 within 5 GeV of m_H ; and at 400 GeV and above increments of 50 GeV up to 3.5 TeV. A total of 45 mass points for fitting the $l\bar{l}tq$ efficiency distribution: starting at 300 GeV and above in increments of 50 GeV up to 3.5 TeV. Figure 6.8 shows the efficiencies in the $X \rightarrow 4\ell$ and $X \rightarrow 2\ell 2q$ analyses in various categories.

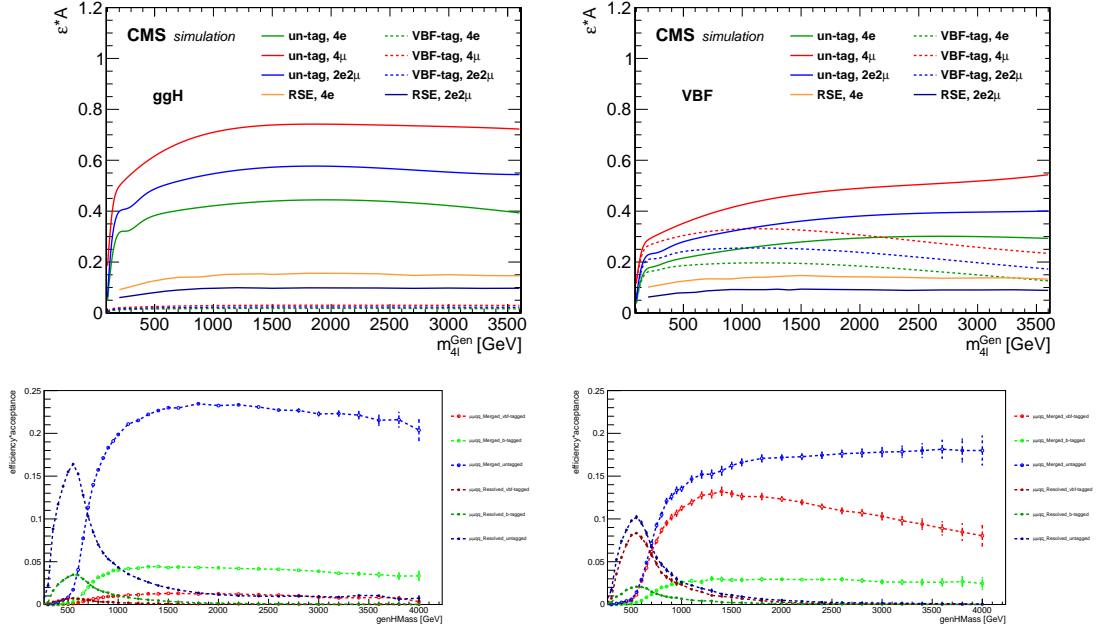


Figure 6.8: The efficiency of the signal events to pass the $X \rightarrow ZZ \rightarrow 4\ell$ (top) and $X \rightarrow ZZ \rightarrow \mu\mu qq$ (bottom) selection as a function of the generated ZZ invariant mass, from ggH (left) and VBF (right) production modes.

Parameterization of spin-2 model is performed using spin-0 simulation re-weighted

with the MELA weights to account for different kinematics. In general, efficiency for the 2_b^+ model is higher than for isotropic spin-0 decay because of higher acceptance efficiency in the spin-2 model with the Z bosons predominantly in the central region of the detector.

6.5.3 Resolution

Parameterization of the resolution function $\mathcal{R}(m_{4\ell}|m_{4\ell}^{\text{ideal}})$ is extracted for each final state of 4ℓ ($2e2\mu$, $4e$, 4μ) and $2\ell 2q$ ($2e2J$, $2e1J$, $2\mu 2J$, $2\mu 1J$). In $2\ell 2q$ final state, the 3 categories (b-tag, VBF-jets, and inclusive) are merged, and the electron and muon channels are also merged, because resolution effects are dominated by jet reconstruction.

The resolution in other production mechanisms and in the spin-2 model are generally very similar to the SM gluon fusion production. Therefore, a common parameterization of resolution can be used.

A total of 54 mass points are used for fits: from 120 GeV, increments of 20 GeV up to 900 GeV, increments of 50 GeV up to 1600 GeV, with the selection window within 5 GeV below 1 TeV and within 5% above. The distribution of resolution $(m_{4\ell} - m_{4\ell}^{\text{ideal}})$ is parameterized, which does not vary much within the mass windows quoted above.

Several representative examples are shown in Fig. 6.9 (4ℓ) and Fig. 6.10 ($2\ell 2q$). Dependence of six parameters of the double-Crystal Ball function is parameterized

with the glued polynomial functions in several mass regions, which preserve the value and derivative of the function at the junctions. After initializing the parameters from individual fits in each mass window, a joint fit is performed using all mass distributions at the same time, leading to a smooth and optimal dependence of all parameter on m_{4f} , see Fig. 6.11 (4ℓ) and Fig. 6.12 ($2\ell 2q$) for such dependence.

6.5.3.1 Final parameterization

The final signal parameterization in 2D is built with the conditional template $\mathcal{T}(D_{\text{bkg}}|m_{4f})$ which describes the D_{bkg} discriminant for each value of m_{4f} .

$$\mathcal{P}_{vv}^{i,k}(m_{4f}, D_{\text{bkg}}) = \mathcal{P}_{vv}^{\text{reco}}(m_{4f}) \times \mathcal{T}(D_{\text{bkg}}|m_{4f}). \quad (6.4)$$

The template $\mathcal{T}(D_{\text{bkg}}|m_{4f})$ parameterization includes all detector effects affecting the D_{bkg} distribution. Definition of $D_{\text{bkg}}^{\text{kin}}$ depends on the signal spin model. Examples of $\mathcal{T}(D_{\text{bkg}}^{\text{kin}}|m_{4\ell})$ distributions are shown in Section 6.3.

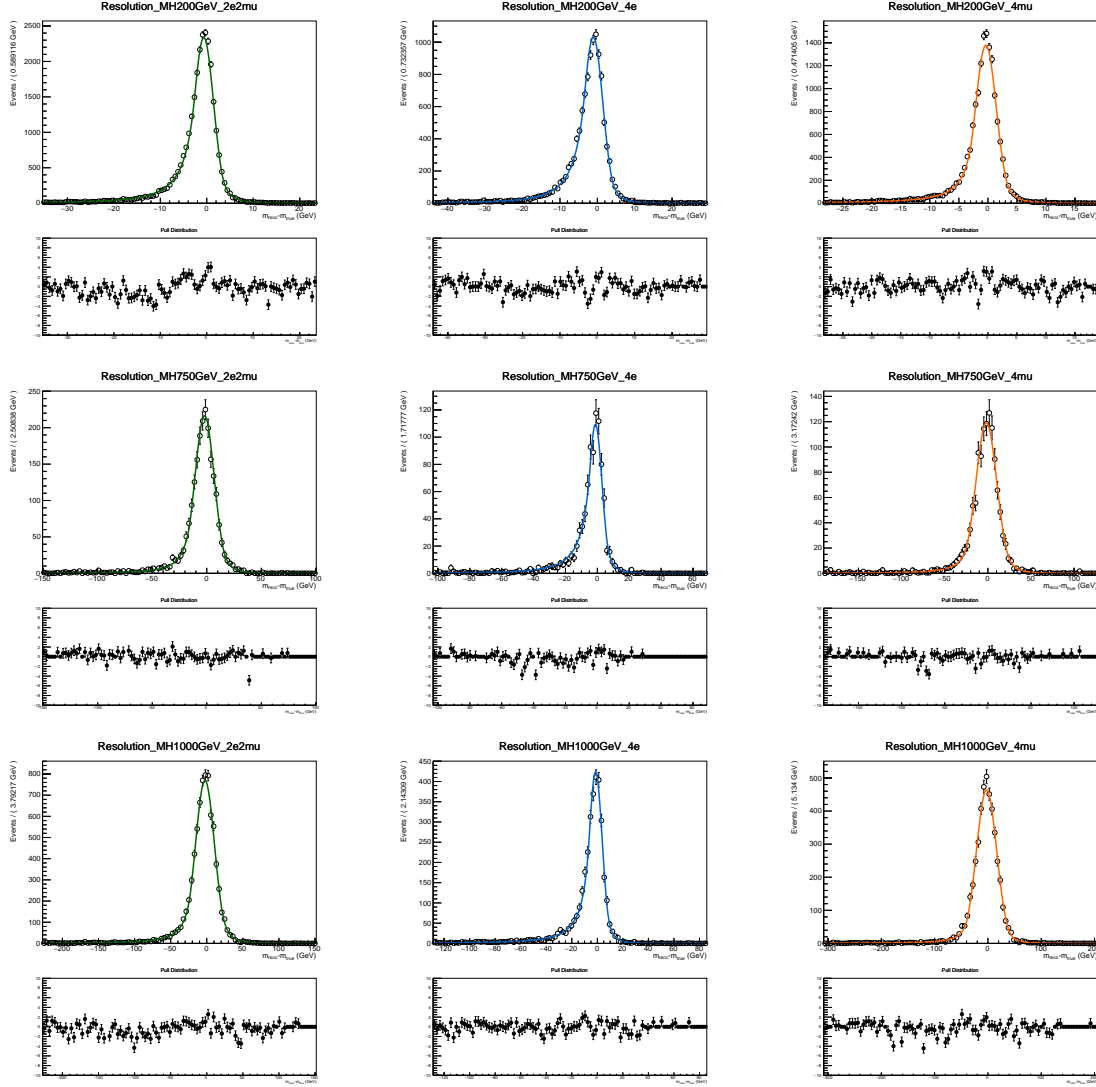


Figure 6.9: Representative $m_{4\ell}$ distributions of a resolution function $\mathcal{R}(m_{4\ell}|m_{4\ell}^{\text{ideal}})$ in $2e2\mu$ (left), $4e$ (middle), and 4μ (right) channels. Several examples are shown from top to bottom: $m_{4\ell} = 200, 740, 1000$ GeV.

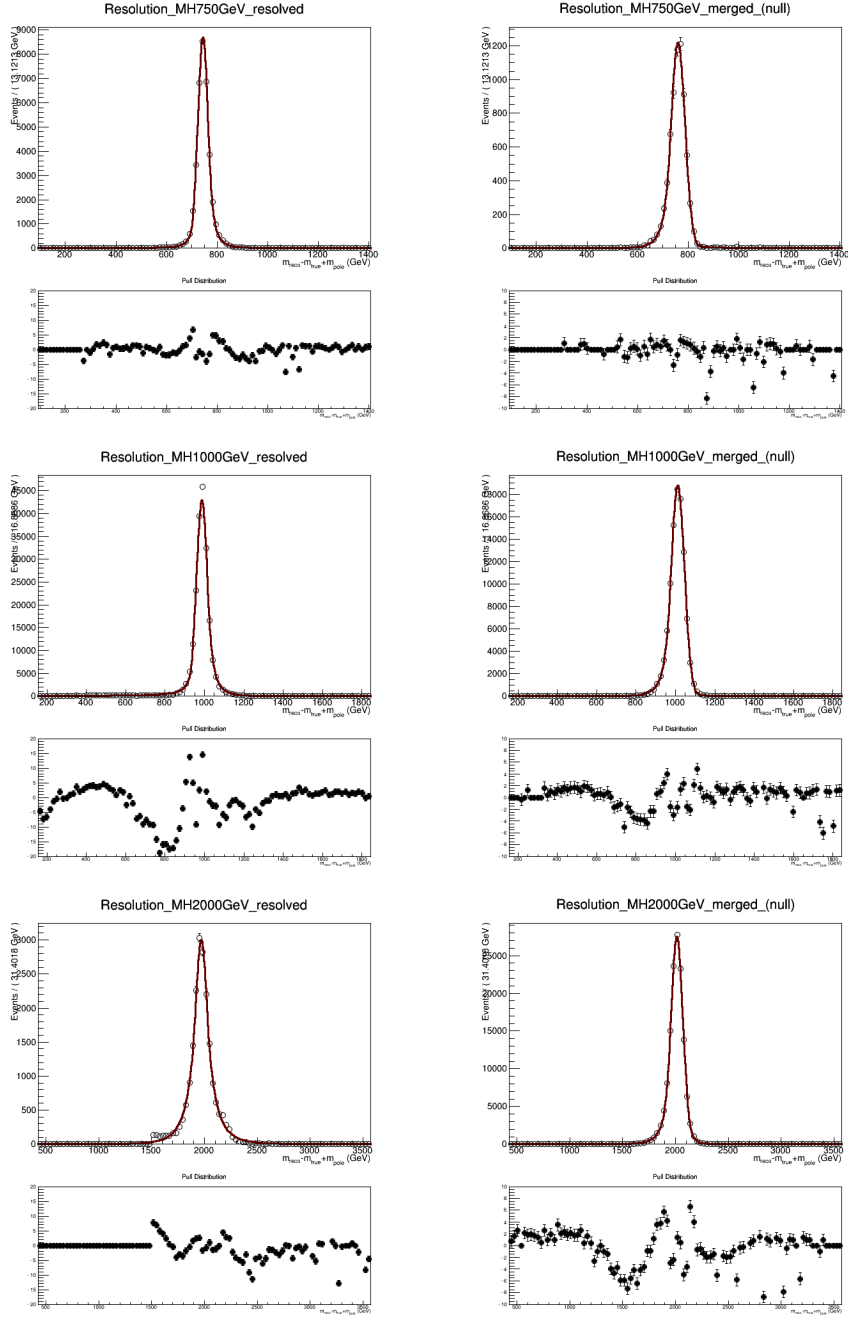


Figure 6.10: Representative $m_{2\ell 2q}$ distributions of a resolution function $\mathcal{R}(m_{2\ell 2q}|m_{2\ell 2q}^{\text{ideal}})$ two-jet (left) and merged-jet (right) categories. Several examples are shown from top to bottom: $m_{2\ell 2q} = 750, 1000, 2000$ GeV.

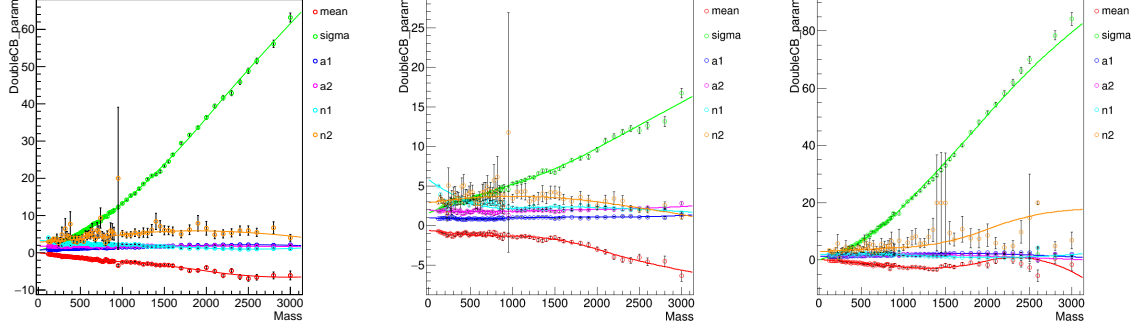


Figure 6.11: Dependence of six parameters of the resolution function in the $2e2\mu$ (left), $4e$ (middle), and 4μ (right) channels. Point show results of individual fits, smooth curves show parameterization from a simultaneous fit of all distributions.

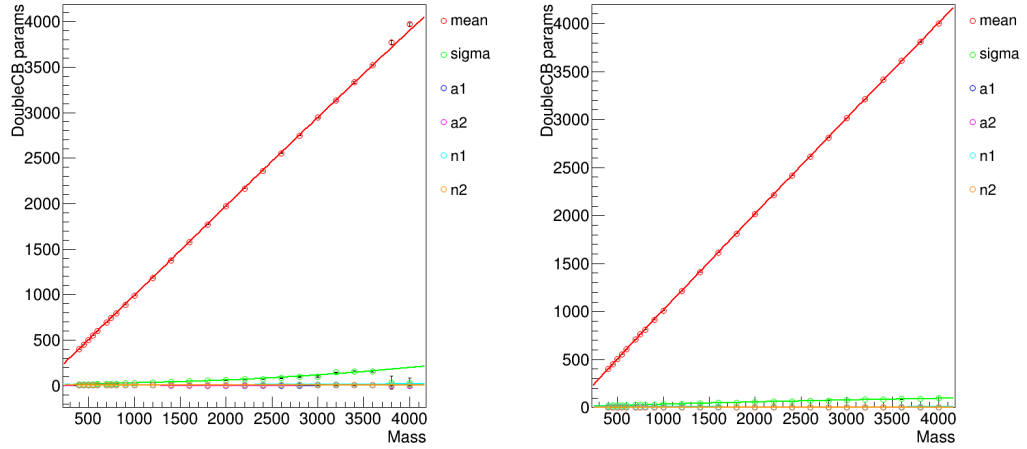


Figure 6.12: Dependence of six parameters of the resolution function in the two-jet (left) and merged-jet (right) categories. Point show results of individual fits, smooth curves show parameterization from a simultaneous fit of all distributions.

6.6 Background Estimation

6.6.1 $X \rightarrow ZZ \rightarrow 4\ell$

The background estimation in $X \rightarrow ZZ \rightarrow 4\ell$ channel is the same as described in Chapter 5.

6.6.2 $X \rightarrow ZZ \rightarrow 2\ell 2q$

The following SM processes are considered as background in $X \rightarrow ZZ \rightarrow 2\ell 2q$ analysis: Z+jets, diboson, and $t\bar{t}$ production.

The diboson production (mainly ZZ and WZ) is simulated using MC while the other two contributions are estimated either using MC simulation corrected to data in control regions (Z+jets), or extracted directly from data in control regions ($t\bar{t}$). The latter two cases are described in detail in the following subsections.

6.6.2.1 Estimation of Z+jets background

The Z+jets background is the dominant SM background in $X \rightarrow ZZ \rightarrow 2\ell 2q$ analysis. Events from this background are characterised by having a real $Z \rightarrow \ell\ell$ decay, while associated jets from regular q/g emission are misidentified as coming from a $Z \rightarrow q\bar{q}$ decay, and are combined to generate a misidentified hadronic V boson.

The misidentified V comes either from the combinatoric background for the resolved category ($Z + 2\text{jets}$), where the dijet system happens to have an invariant mass compatible with Z boson, or from an unusual parton-shower + hadronization development for a single jet, leading to a configuration similar to that of the boosted $Z \rightarrow q\bar{q}$ decay in the merged case.

In both cases, a sideband region with a misidentified hadronic V mass close to that of the signal region can be used to estimate the contribution of this background. This is called the *alpha method*. To address the correlation between the hadronic V mass and the m_{ZZ} in these configurations, a correction factor, *alpha transfer function* $\alpha(m_{ZZ})$, is calculated from the ratio of the m_{ZZ} distributions in the sideband and signal regions calculated in the Z+jets simulation:

$$\alpha(m_{ZZ}) = \frac{N_{\text{SIG}}^{\text{MC}}(m_{ZZ})}{N_{\text{SB}}^{\text{MC}}(m_{ZZ})}, \quad (6.5)$$

The Z+jets m_{ZZ} distribution in the data signal region can be estimated by multiplying the alpha function by the the Z+jets m_{ZZ} distribution in the data sideband region. The pure Z+jets distribution in the hadronic V mass is obtained by subtracting the subdominant backgrounds from the data.

To summarise, the method to estimate the Z+jets background comprises the following steps:

- Estimate the Z+jets m_{ZZ} distribution in the data sideband region by subtracting the subdominant backgrounds from the data.

- Estimate the sideband to signal alpha transfer function by the ratio of the m_{ZZ} distributions in the sideband and signal regions in Z+jets simulation.
- Estimate the shape of Z+jets m_{ZZ} distribution in the data signal region by the product of the alpha function and the Z+jets m_{ZZ} distribution in the data sideband region.

6.6.2.2 Estimation of $t\bar{t}$ background

The $t\bar{t}$ background is an important source of contamination in the b-tagged categories. It is estimated from the data using the control region built with events in $e^\pm\mu^\mp$ final state passing the same kinematic cuts as the signal region. The control region also accounts for other small backgrounds (as $WW + \text{jets}$, $Z \rightarrow \tau^+\tau^- + \text{jets}$, single top, fakes) where the lepton flavor symmetry can be invoked as well.

MC studies show that the $e^\pm\mu^\mp$ v.s. $e^+e^- + \mu^+\mu^-$ symmetry works at the level of the shapes of the distributions of all considered variables and of distributions in all b-tagging based categories.

Due to limited statistics in data with $e^\pm\mu^\mp$ final state, the di-boson mass shape is taken from $t\bar{t}$ and WW MC simulations, while the normalization is controlled by the number of events in $e^\pm\mu^\mp$ data control region as

$$N_{t\bar{t}+WW}^{SR}(m_{ZZ}) = N_{t\bar{t}+WW}^{SR}{}_{MC}(m_{ZZ}) \times \frac{N_{Data}^{e^\pm\mu^\mp CR}}{N_{t\bar{t}+WW}^{e^\pm\mu^\mp CR}{}_{MC}}, \quad (6.6)$$

where $N_{t\bar{t}+WW}^{SR}(m_{ZZ})$ is the mass spectrum from $t\bar{t}$ and WW MC simulations, and

$\frac{N_{Data}^{e^{\pm}\mu^{\mp} CR}}{N_{t\bar{t}+WW}^{e^{\pm}\mu^{\mp} CR MC}}$, the ration of number events between data and MC in $e^{\pm}\mu^{\mp}$ control region,

is used to weight the normalization.

6.7 Systematic Uncertainties

Theoretical uncertainties which affect both the signal and background estimation include uncertainties from the renormalization and factorization scale and choice of PDF set. The uncertainty from the renormalization and factorization scale is determined by varying these scales between 0.5 and 2 times their nominal value while keeping their ratio between 0.5 and 2. The uncertainty from the PDF set is determined by taking the root mean square of the variation when using different replicas of the default NNPDF set. An additional uncertainty of the 10% on the K factor used for the $gg \rightarrow ZZ$ prediction is applied. The uncertainty on the NNLO-to-NLO K factor of the ZZ and WZ cross sections is about 10%. QCD scale and PDF sets uncertainties are evaluated from simulation, and are on the event categorization and overall signal and background yields. Systematic uncertainty from the Z branching ratio is taken into account on the signal yields.

The uncertainty on the knowledge of the integrated luminosity of the data sample (2.6%) introduces an uncertainty on the number of signal and background events passing the final selection. Uncertainties on the lepton identification and reconstruction efficiency lead to 6–11% uncertainty on 4ℓ final state and 4-8% on $2\ell 2q$, on the

normalization of both signal and background. The uncertainty on the lepton energy scale is 0.04% for muons and 0.3% for electrons, which introduces a relative 20% uncertainty on the signal resolution for 4ℓ and $2\ell 2q$. The jet energy scale and jet reconstruction efficiency uncertainty affect both signal and background in the yields, and the most important uncertainty on the $2\ell 2q$ signal shapes.

In addition, each final state has channel specific uncertainties mainly from the data driven background estimation, as well as from boosted and merged jet reconstruction.

6.7.1 $X \rightarrow ZZ \rightarrow 4\ell$

Experimental uncertainties mainly arise from the reducible background estimation. Impacts from the limited number of events in the control regions as well as in the region where the misidentification rates are computed. Additional sources of systematic uncertainty arise from the difference in the composition of the sample from which the misidentification rate is computed and the control regions of the two methods where the fake rate is applied. The systematic uncertainty on the $m_{4\ell}$ shape is determined by taking the envelope of differences among the shapes from the OS and SS methods in the three different final states. The combined systematic uncertainty is estimated to be about 40 to 55%.

6.7.2 $X \rightarrow ZZ \rightarrow 2\ell 2q$

The dominant uncertainties on the signal selection efficiency arise from uncertainties on the efficiency to tag the hadronic jet as a Z in the high-mass boosted categories, and from uncertainties on the b-tagging efficiency. The efficiency of the boosted W tagging selection and its corresponding systematic uncertainty has been measured in data using a sample enriched in semileptonic $t\bar{t}$ events. The b-tagging efficiencies and their corresponding systematic uncertainties have been measured in data using samples enriched in beauty decay events.

On the data driven background estimation, the statistical uncertainty of the $e^\pm\mu^\mp$ control sample is propagated to the uncertainty on the $t\bar{t} + WW$ estimation. The alpha method for the Z+jets background estimation depends on the uncertainty on the extrapolation factor and statistics of the dijet mass or pruned jet mass sideband region. The studies show that the jet energy scale and resolution can affect the extrapolation factor $\alpha(m_{ZZ})$ up to 3 to 10%. The statistical uncertainty of the sideband region is propagated by the covariance matrix on the fitting of the sideband data m_{ZZ} distribution. In the b-tagged and VBF-tagged categories, the uncertainty on $\alpha(m_{ZZ})$ is fully covered by the statistical uncertainty of the sideband data, thus ignored. Systematic uncertainties on alternative alpha-factor binning average and alternative functional forms are propagated to the limits using appropriate nuisance parameters that describe a smooth variation between the nominal and alternative function.

For the two-dimensional \mathcal{D}_{Zij} template shapes, two systematic uncertainties are

considered for signal samples: jet-energy scale and resolution variations, as well as comparison with identical MC samples where HERWIG++⁷ is used for parton showering and hadronisation, instead of PYTHIA. For background templates, a conservative systematic uncertainty is taken by using alternative templates where the content of each two-dimensional interval is replaced by the content of the preceding or following interval in m_{ZZ} .

6.8 Results

The search for a scalar spin-0 resonance X decaying to $ZZ \rightarrow 4\ell$ and $ZZ \rightarrow 2\ell 2q$ final states is performed for the range of masses m_X between 130 and 3000 GeV. The width of the resonance Γ_X is allowed to have any value, starting from the narrow-width approximation (denoted as $\Gamma_X = 0$) to a large width.

Production of the X resonance is considered to be either in gluon fusion or vector boson fusion, where VX production is included according to expectation of the relative VX and VBF cross sections.

Figure 6.13 shows the upper limits at the 95% C.L. on the $pp \rightarrow X$ cross section times $X \rightarrow ZZ$ branching fraction $\sigma_X \times \mathcal{B}_{ZZ}$ as a function of m_X at $\Gamma_X = 0, 10$, and 100 GeV, for 4ℓ final state. Results are shown with both f_{VBF} floated (left) and $f_{VBF} = 1$ for pure VBF model (right). Figure 6.14 shows the upper limits for $2\ell 2q$ final state, and Figure 6.15 show the upper limits with 4ℓ and $2\ell 2q$ channels combined.

Figure 6.16 shows the upper limits for spin-2 narrow resonance, assuming 100% gluon fusion production. Only 12.9 fb^{-1} data from 2016 are used.

12.9 fb^{-1}

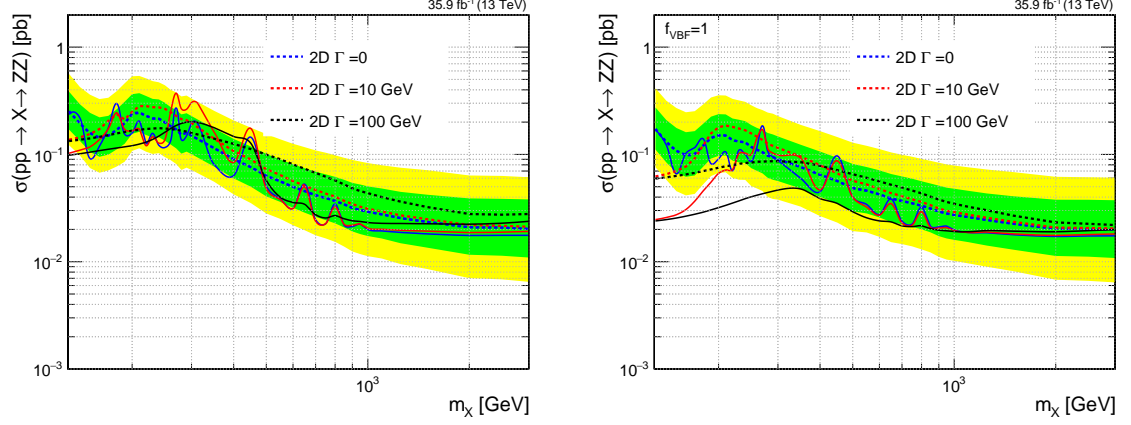


Figure 6.13: Expected and observed upper limits on the $pp \rightarrow X \rightarrow ZZ$ cross section as a function of m_X at $\Gamma_X = 0, 10$, and 100 GeV , for 4ℓ final state, using 35.9 fb^{-1} of CMS data at 13 TeV . Left: f_{VBF} profiled. Right: $f_{\text{VBF}} = 1$, pure VBF model.

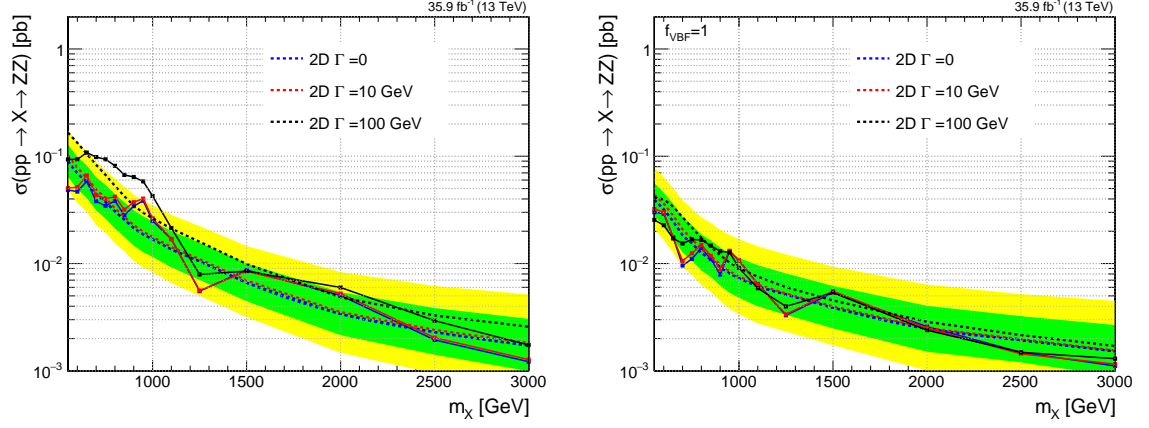


Figure 6.14: Expected and observed upper limits on the $pp \rightarrow X \rightarrow ZZ$ cross section as a function of m_X at $\Gamma_X = 0, 10$, and 100 GeV, for $2\ell 2q$ final state, using 35.9 fb^{-1} of CMS data at 13 TeV. Left: f_{VBF} profiled. Right: $f_{\text{VBF}} = 1$, pure VBF model.

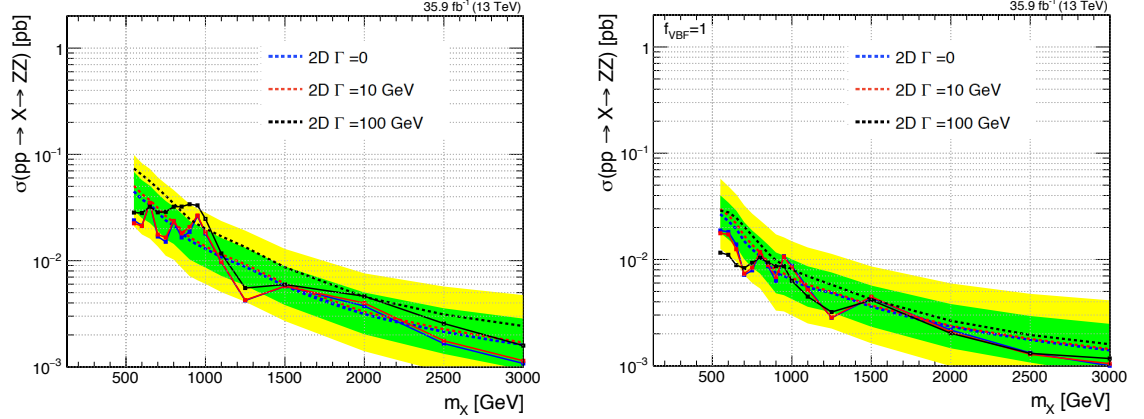


Figure 6.15: Expected and observed upper limits on the $pp \rightarrow X \rightarrow ZZ$ cross section as a function of m_X at $\Gamma_X = 0, 10$, and 100 GeV, with 4ℓ and $2\ell 2q$ channels combined, using 35.9 fb^{-1} of CMS data at 13 TeV. Left: f_{VBF} profiled. Right: $f_{\text{VBF}} = 1$, pure VBF model.

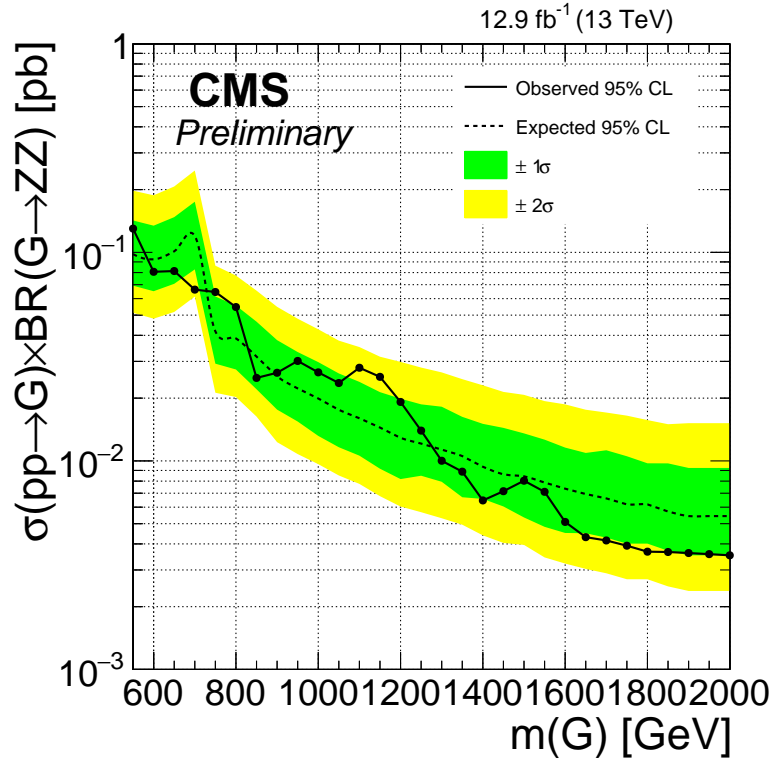


Figure 6.16: Expected and observed upper limits on the $pp \rightarrow X \rightarrow ZZ$ cross section under narrow width resonance assumption for 12.9 fb⁻¹ of CMS data at 13 TeV with a spin-2 graviton assumption.

Chapter 7

Conclusion

The Higgs boson was the last missing piece of the Standard Model and was discovered by CMS and ATLAS in 2012. After the discovery, the precise measurement of Higgs boson's quantum properties and the search for new resonances have become the priority, in order to gain possible evidence about new physics beyond the Standard Model.

The data analysis framework and statistical methods are introduced. The MELA discriminant which is a critical tool for both property measurements and searching for new resonance is described in Chapter 2.

In Chapter 5, exotic spin models (spin-1 and spin-2) have been tested using Run1 data from LHC. All spin-1 and spin-2 models are excluded at 95% confidence level, including spin-1 mixture states. Combined with other analyses in CMS, it has been shown that the discovered Higgs boson is a spin-0 particle, consistent with expecta-

tions of the Standard Model. A few theoretical models, such as 2HDM, predicted the existence of additional Higgs bosons. In Chapter 6, the search for an additional high mass resonance is performed using Run2 data from LHC, using $ZZ \rightarrow 4\ell$ and $ZZ \rightarrow 2\ell 2q$ channels. No excess is found for mass up to 3 TeV.

So far we have used $\sim 30 \text{ fb}^{-1}$ of data. We expect $\sim 300 \text{ fb}^{-1}$ of data by 2025, and the High-Luminosity upgrade project of LHC (HL-LHC) will start in 2025 and will deliver $\sim 3000 \text{ fb}^{-1}$ of data, so we have just $\sim 1\%$ of full sample by now. With higher integrated luminosity, more events from rare processes of Higgs will be observed. Higgs boson self coupling and its coupling with other particles can be more precisely measured. It will also provide higher sensitivity for SUSY particles searches.

Besides LHC, other new large particle experiments are being planned, such as International Linear Collider (ILC) in Japan, Circular Electron Positron Collider (CEPC) in China, and Future Circular Collider (FCC) at CERN. These future experiments will help to explore the unknown realms of particle physics and answer the remaining questions discussed in Chapter 1.

Bibliography

- [1] Commissioning of the particle-flow event reconstruction with the first LHC collisions recorded in the CMS detector. CMS Physics Analysis Summary CMS-PAS-PFT-10-001, 2010.
- [2] Georges Aad et al. Observation of a new particle in the search for the Standard Model Higgs boson with the ATLAS detector at the LHC. *Phys.Lett.*, B716:1–29, 2012.
- [3] S. Agostinelli et al. GEANT4: a simulation toolkit. *Nucl. Instrum. Meth. A*, 506:250, 2003.
- [4] John Allison et al. Geant4 developments and applications. *IEEE Trans. Nucl. Sci.*, 53:270, 2006.
- [5] Ian Anderson, Sara Bolognesi, Fabrizio Caola, Yanyan Gao, Andrei V. Gritsan, et al. Constraining anomalous HVV interactions at proton and lepton colliders. *Phys.Rev.*, D89:035007, 2014.

- [6] E. Bagnaschi, G. Degrandi, P. Slavich, and A. Vicini. Higgs production via gluon fusion in the POWHEG approach in the SM and in the MSSM. *JHEP*, 1202:088, 2012.
- [7] M. Bahr et al. Herwig++ Physics and Manual. *Eur. Phys. J.*, C58:639–707, 2008.
- [8] G. L. Bayatian et al. CMS technical design report, volume II: Physics performance. *J. Phys.*, G34(6):995–1579, 2007.
- [9] Volker Blobel and Claus Kleinwort. A New method for the high precision alignment of track detectors. In *Advanced Statistical Techniques in Particle Physics. Proceedings, Conference, Durham, UK, March 18-22, 2002*, pages URL–STR(9), 2002.
- [10] Sara Bolognesi, Yanyan Gao, Andrei V. Gritsan, Kirill Melnikov, Markus Schulze, et al. On the spin and parity of a single-produced resonance at the LHC. *Phys.Rev.*, D86:095031, 2012.
- [11] Jonathan M. Butterworth, Adam R. Davison, Mathieu Rubin, and Gavin P. Salam. Maximizing Boosted Top Identification by Minimizing N-subjettiness. *JHEP*, 02:093, 2012.
- [12] John M. Campbell, R. Keith Ellis, and Ciaran Williams. Bounding the Higgs

- width at the LHC using full analytic results for $gg \rightarrow e^-e^+\mu^-\mu^+$. *JHEP*, 04:060, 2014.
- [13] Serguei Chatrchyan et al. Observation of a new boson at a mass of 125 GeV with the CMS experiment at the LHC. *Phys.Lett.*, B716:30–61, 2012.
- [14] CMS Collaboration. Particle-flow event reconstruction in cms and performance for jets, taus, and met. CMS Physics Analysis Summary CMS-PAS-PFT-09-001, 2009.
- [15] ATLAS Collaboration. Procedure for the LHC Higgs boson search combination in summer 2011. 2011.
- [16] The CMS collaboration. Alignment of the cms tracker with lhcb and cosmic ray data. *Journal of Instrumentation*, 9(06):P06009, 2014.
- [17] Kyle Cranmer. Practical Statistics for the LHC. In *Proceedings, 2011 European School of High-Energy Physics (ESHEP 2011): Cheile Gradistei, Romania, September 7-20, 2011*, pages 267–308, 2015. [,247(2015)].
- [18] F. Englert and R. Brout. Broken Symmetry and the Mass of Gauge Vector Mesons. *Phys.Rev.Lett.*, 13:321–322, 1964.
- [19] Stefano Frixione, Paolo Nason, and Carlo Oleari. Matching NLO QCD computations with Parton Shower simulations: the POWHEG method. *JHEP*, 0711:070, 2007.

- [20] Andrei V. Gritsan, Raoul Röntsch, Markus Schulze, and Meng Xiao. Constraining anomalous Higgs boson couplings to the heavy flavor fermions using matrix element techniques. 2016.
- [21] G.S. Guralnik, C.R. Hagen, and T.W.B. Kibble. Global Conservation Laws and Massless Particles. *Phys.Rev.Lett.*, 13:585–587, 1964.
- [22] Peter W. Higgs. Broken Symmetries and the Masses of Gauge Bosons. *Phys.Rev.Lett.*, 13:508–509, 1964.
- [23] Peter W. Higgs. Broken symmetries, massless particles and gauge fields. *Phys.Lett.*, 12:132–133, 1964.
- [24] Peter W. Higgs. Spontaneous Symmetry Breakdown without Massless Bosons. *Phys.Rev.*, 145:1156–1163, 1966.
- [25] V. Karimaki, A. Heikkinen, T. Lampen, and T. Linden. Sensor alignment by tracks. *eConf*, C0303241:TULT008, 2003.
- [26] T.W.B. Kibble. Symmetry breaking in nonAbelian gauge theories. *Phys.Rev.*, 155:1554–1561, 1967.
- [27] L. Landau. On the energy loss of fast particles by ionization. *J. Phys. (USSR)*, 8:201, 1944.
- [28] LHC Higgs Cross Section Working Group, S. Heinemeyer, C. Mariotti, G. Pas-

- sarino, and R. Tanaka (Eds.). Handbook of LHC Higgs Cross Sections: 3. Higgs Properties. *CERN-2013-004*, CERN, Geneva, 2013.
- [29] Paolo Nason and Carlo Oleari. NLO Higgs boson production via vector-boson fusion matched with shower in POWHEG. *JHEP*, 1002:037, 2010.
- [30] C. Patrignani et al. Review of Particle Physics. *Chin. Phys.*, C40(10):100001, 2016.
- [31] Torbjörn Sjöstrand, Stephen Mrenna, and Peter Skands. PYTHIA 6.4 physics and manual. *JHEP*, 05:026, 2006.

Vita

Education

- Ph.D. Experimental Particle Physics, Johns Hopkins University, August 2017.
- B.Sc., with First Class Honor, double major in physics and mathematics, the University of Hong Kong, June 2011.

Work Experience

- Research/Teaching Assistant, Johns Hopkins University, January 2012 - June 2017.
- Research Assistant, European Organization for Nuclear Research, January 2015 - December 2015.
- Undergraduate Research Assistant, The University of Hong Kong, June 2009 - December 2010.

- Summer Student, European Organization for Nuclear Research, Geneva, July 2010 - August 2010.

Conferences and Workshops

- CMS Data Analysis School, Fermilab, January 2013.
- LHCC Meeting, Geneva, Switzerland, March 2015.
- CERN-Fermilab Hadron Collider Physics Summer School, Geneva, Switzerland, July 2015.
- Yandex MLHEP Machine Learning Workshop, St Petersburg, Russia, August 2015.
- Higgs Coupling 2015, Durham, UK, October 2015.

Publications

- “Search for new diboson resonances in the dilepton + jets final state at $\sqrt{s} = 13$ TeV with 2016 data”, The CMS Collaboration, preprint CMS-PAS-HIG-16-034
- “Measurements of properties of the Higgs boson and search for an additional resonance in the four-lepton final state at $\sqrt{s} = 13$ TeV”, The CMS Collaboration, preprint CMS-PAS-HIG-16-033

- “Constraints on the spin-parity and anomalous HVV couplings of the Higgs boson in proton collisions at 7 and 8 TeV”, The CMS Collaboration, Phys. Rev. D 92, 012004 (2015)
- “Measurement of the properties of a Higgs boson in the four-lepton final state”, The CMS Collaboration, Phys. Rev. D 89, 092007 (2014)
- “CMS Tracker Alignment Performance Results Summer 2016”, The CMS Collaboration, CMS-DP-2016-063
- “Alignment of the CMS Tracking-Detector with First 2015 Cosmic-Ray and Collision Data”, The CMS Collaboration, CMS-DP-2015-029